

VCSEL-Based Multi-Mode Fiber Optical Links
for 100Gbit/s Transmission: Advanced Simulation Tools
and Experimental Link Studies

A Dissertation
Presented to
The Academic Faculty

By

Sriharsha Kota Pavan

In Partial Fulfillment
of the Requirements for the Degree
Doctor of Philosophy in the
Electrical and Computer Engineering



School of Electrical and Computer Engineering
Georgia Institute of Technology
May 2016

Copyright © 2016 by Sriharsha Kota Pavan

VCSEL-Based Multi-Mode Fiber Optical Links
for 100Gbit/s Transmission: Advanced Simulation Tools
and Experimental Link Studies

Approved by:

Professor Stephen E. Ralph, Advisor
School of Electrical and Computer
Engineering
Georgia Institute of Technology

Professor Gee-Kung Chang
School of Electrical and Computer
Engineering
Georgia Institute of Technology

Professor Benjamin Klein
School of Electrical and Computer
Engineering
Georgia Institute of Technology

Professor Russell D. Dupuis
School of Electrical and Computer
Engineering
Georgia Institute of Technology

Professor Michael Chapman
School of Physics
Georgia Institute of Technology

Date Approved: January 8, 2016

To

My Parents,

Smt Kota Visalakshi & Sri K.E.V. Kameshwar Rao

for their love support, and sacrifices;

And

My Uncle who has left valuable memories through my childhood,

Late Sri Kota Srinivas Chakravarthy;

ACKNOWLEDGEMENTS

I would like to thank my advisor Prof. Stephen E. Ralph for his passionate and visionary guidance leading the research to solve some of the most fundamental problems with significant practical implications in the field of multi-mode fiber optic communications. I am indebted to him for giving me the opportunity to learn and contribute in a resourceful lab like the Terabit Optical Networking Consortium. I am also grateful to Dr. Robert Lingle Jr., Dr. Kasyapa Balemarthy and Dr. Yi Sun of OFS Fitel, Dr. David W. Dolfi of Avago Technologies, Prof. Benjamin Klein of ECE, Georgia Tech, and Dr. David Cunningham for their insightful inputs in the numerous discussions we had during this research collaboration.

I am indebted to my lab colleagues Justin Lavrencik, Patrick J. Decker, and Patrick C. Caputo for helping me in the experimental part of my research, and Jie Pan, Pierre Isautier, Jerrod Langston, Andy Stark, David Haupt Stuart Hughes and Michael Pratt for helping maintain high energy levels in the group with fun-filled atmosphere all through these years.

I would like to thank Prof. Gee-Kung Chang, Prof. Benjamin Klein, Prof. Russell D. Dupuis, and Prof. Michael Chapman for serving on my Ph.D. committee. Their feedback on my research has been useful in improving both the content and presentation of this dissertation. I am forever indebted to my first advisor Dr. Richard S. Wolff of Montana State University, for introducing me to the field of Optics, my former colleagues at RSoft Inc. (now Synopsys), Mr. Jigesh Patel, Dr. Dwight Richards, and Mr. Enrico Ghillino for their encouragement and guidance in the early stages of my career.

I thank almighty for having me blessed with the coolest parents who are my best friends till date. Their love and support all through my life made me what I am. One person who had the most impact on my career and life choices so far is my sister Dr. Kokila Hota. I thank her for not only being a great friend and guide, but also giving the greatest gift to our family- my lovely little niece, Lasya Hota. Lasya had been a source of immense joy and pleasure during these years, and

will always remain special to me. I would also like to thank my brother-in-law Partha Hota, for being there for me at crucial times with his experienced and insightful advices in both personal and professional fronts last few years.

This list would be incomplete without the mention of my uncle Mr. Kota Siva Kumar, and Dr. Kota Sailaja who are an inspiration in our family on the academic front, and uncle Late Sri. Kota Srinivas Chakravarthy, for their unconditional love and support all through my life.

I owe a lot to my roommates - Karthik Nayani, Rajiv Damodaran, and Sricharan Yarlagadda, and to my friends from Amlu apartments for making my stay in Atlanta memorable and for all the enriching experiences. I was lucky enough to have my dear sister Sirisha Parimi nearby all these years- just a short drive away whenever I missed family and delicious home-food! A big 'Cheers' to my friends at Windsor apartments for being my default stress buster group – I thoroughly enjoyed and miss the crazy parties we had. It was a pleasure being part of the Georgia Tech Cricket club which had several high moments over the last few years in Cricket - a sport that had been my first love since childhood.

I would like to end this long list by thanking a special person who has made my world beautiful and been the reason for much happiness in the family recently - my beloved wife Anusha Uppuluri. Her crucial support during this final leg ensured an uncompromised output in my Thesis. Looking forward to a beautiful journey ahead.

TABLE OF CONTENTS

	Page
ACKNOWLEDGEMENTS	iv
LIST OF TABLES	ix
LIST OF FIGURES	x
LIST OF ABBREVIATIONS	xiii
SUMMARY	xv
CHAPTER 1 HIGH SPEED MULTIMODE FIBER OPTICAL LINKS	1
1.1 Types of MMF	2
1.2 Moving Towards 100Gbit/s per Lambda for VCSEL-MMF Links	3
CHAPTER 2 IEEE 802.3 MODEL FOR 10GBIT/S VCSEL-MMF LINKS	6
CHAPTER 3 PRIOR ART	9
3.1 Link Penalties in High Speed MMF Links: Temperature Dependence	9
3.2 Mode Partition Noise in VCSEL-Based MMF Links	10
3.3 High Speed Experimental Demonstrations of VCSEL-MMF Links	13
3.4 25Gbit/s POF Links and Impact of Electronic Equalization	14
CHAPTER 4 END-TO-END VCSEL-MMF LINK MODELING FOR 100GBIT/S	17
4.1 Full Physical Simulation Model	17
4.1.1 Noise Modeling	19
4.2 IEEE 802.3 Conformed Analytic Model	22
4.3 Comparison Between Full Physical Simulation Model Versus Analytic Model	23
CHAPTER 5 INVESTIGATION OF VCSEL-MMF LINK PENALTIES	26
5.1 25Gbit/s Link Penalties at 850nm: Temperature Dependence	26

5.2	Experimental Setup	27
5.3	Estimation of Link Penalties using the End-to-end Analytic Link Model	29
5.4	Results: Temperature Dependence of Back-to-Back and 150m Link Penalties	31
5.4.1	Back-to-Back	31
5.4.2	150m OM4 Fiber Links	34
CHAPTER 6 NEW MODEL FOR MPN BASED ON LANGEVIN-RATE EQUATIONS		41
6.1	VCSEL Noise and MPN	41
6.2	Underlying Assumptions in the IEEE Standard O-A Model for MPN	44
6.3	Langevin Noise-Driven Spatio-Temporal Rate Equations for VCSELs	46
6.4	Comprehensive Physical Model for VCSEL Noise From the Rate Equations	49
6.4.1	Closed-Form Expressions for VCSEL Mode Correlations	53
6.4.2	Analytic Model for the VCSEL Noise: Simplified Covariance Matrix	63
6.4.3	Special Cases: VCSEL With High and Low Overlapping Modes	67
6.5	Direct Experimental Validation of the New MPN Model	69
6.5.1	Experimental Methodology	69
6.5.2	Results and Discussions	70
6.6	Penalty Due to MPN and COV Matrix	75
6.7	Summary	78
CHAPTER 7 EXPERIMENTAL STUDIES: PAM-4 LINKS BEYOND 50GBIT/S		80
7.1	PAM-4 Experimental Setup	82
7.1.1	VCSEL Characterization	83
7.1.2	PAM-4 BER Measurement	85
7.1.3	Forward Error Correction (FEC)	85
7.1.4	Fiber Set Examined	86
7.1.5	Electrical PAM-4 Implementation	86
7.1.6	Extracting Fiber Penalties Using Analytic Model	87

7.2 PAM-4 MMF Link Analysis: 850nm VCSELs	88
7.3 Moving to Longer Wavelengths: >50Gbit/s PAM-4 at 1050nm	91
7.4 Performance Comparison of 1050nm and 850nm PAM-4 Links	95
7.5 Level-Dependent RIN: Analysis on 900nm VCSELs at 50Gbit/s	97
7.5.1 Dependence of VCSEL RIN Spectrum on Current Bias: L-I-RIN	97
7.5.2 Impact of L-I-RIN on 50Gbit/s PAM-4 Link Modeling	98
7.6 Summary	100
CHAPTER 8 POF STUDIES: IMPACT OF ELECTRONIC EQUALIZATION	101
8.1 VCSEL Characterization	102
8.1.1 VCSEL Characterization: Spectrum	104
8.1.2 VCSEL Characterization: L-I-V Characteristics	105
8.2 Receiver Characterization	107
8.3 Plastic Optical Fiber Modal Bandwidth Characterization	107
8.4 Fractional-spaced Linear Analog Equalizer	111
8.5 Impact of a T/2-FFE Equalizer on 100m POF Link: Results and Discussions	113
8.6 POF Channel Estimation	114
CHAPTER 9 CONCLUSION	117
9.1 Summary of Contributions	117
9.2 Future Directions	119
APPENDIX A DERIVATION OF COV MATRIX FROM LANGEVIN-DRIVEN VCSEL RATE EQUATIONS	121
APPENDIX B RELATIONSHIP BETWEEN MPN PENALTY AND COV MATRIX	133
APPENDIX C PUBLICATION LIST	135
REFERENCES	137

LIST OF TABLES

	Page
Table 1.1: Comparison of Glass fiber and GI-POF based MMF links	3
Table 5.1: Measured penalties of the 6 VCSEL-MMF combinations at 2 representative temperatures	36
Table 6.1: Typical VCSEL parameters	56
Table 6.2: Calculated α for each mode from the direct measurements along with their corresponding time-averaged normalized mode powers	73
Table 6.3: Extracted Γ_p and k_n for each mode pair from the direct measurements	75
Table 7.1: Complete set of MMF (OM3, OM4 and WBF) examined for > 50Gbit/s PAM-4 Link Analysis at 850nm and 1050nm	87
Table 7.2: Fiber penalty at BER $\sim 10^{-12}$ in 51.56Gbit/s VCSEL-MMF links for the set of MMF examined	96

LIST OF FIGURES

	Page
Figure 1.1: Trend in the increase of bandwidth demand for short reach and long haul networks	1
Figure 2.1: Block diagram of the IEEE 802.3 analytic model for end-to-end link with bitrates up to 10Gbit/s	6
Figure 3.1: Block diagram of fractional spaced FFE	14
Figure 4.1: Block diagram of the full physical simulation model for end-to-end link with bitrates > 25Gbit/s	17
Figure 4.2: Comparison between full physical simulation model and IEEE 802.3 conformed analytic model	24
Figure 5.1: Automated measurement setup. DSO: Digital Sampling Oscilloscope; EA: Error Analyzer; OPM: Optical Power Meter; OSA: Optical Spectrum Analyzer; PD: Photo-Diode; PG: Pattern Generator; TEC: Thermo-Electric Cooler; TIA: Trans-Impedance Amplifier; VOA: Variable Optical Attenuator	28
Figure 5.2: a) Spectral width and mean wavelength vs. VCSEL temperature at nominal bias current 8.4mA; b) Total encircled flux observed at 20 and 65°C for VCSEL B	29
Figure 5.3: Back to back performance at 25Gbit/s for VCSEL A at $T_{VCSEL} = 30^{\circ}C$ and B at $T_{VCSEL} = 20^{\circ}C$	31
Figure 5.4: BER vs. OMA for btb cases for a range of operating temperatures of (a) VCSEL A and (b) VCSEL B	33
Figure 5.5: BER vs. OMA for a range of operating temperatures for two of 6 cases examined (a) VCSEL A with 150m 5200MHz-km fiber and (b) VCSEL B with 150m 10,000MHz-km fiber	35
Figure 5.6: Link sensitivity and penalty with respect to btb at BER 10^{-12} versus VCSEL temperature	38
Figure 6.1: Schematic of a VCSEL structure showing the important physical elements	46
Figure 6.2: Average RIN in a single VCSEL mode vs. normalized time-averaged mode power, Eq. (6.27), (6.30) for typical values of a VCSEL, Table 6.1	57

Figure 6.3: Variation of the normalized cross spectral density, $RIN_{ij,avg}$ calculated from Eq. (6.40) for a 2-mode VCSEL with mode powers $\bar{a}_i = 0.2$ and $\bar{a}_j = 0.8$ with normalized overlap integral C_{ijg} for typical values of a VCSEL, Table 6.1	61
Figure 6.4: Variation of the cross-correlation coefficient, $R_{ij}(0)$ calculated from Eq. (6.32) and (6.43) for a 2-mode VCSEL with mode powers $\bar{a}_i = 0.2$ and $\bar{a}_j = 0.8$ with normalized overlap integral C_{ijg} for typical values of a VCSEL, Table 6.1	62
Figure 6.5: Effect of C_{ijg} on the composite RIN for a 2-mode VCSEL with mode powers $\bar{a}_i = 0.2$ and $\bar{a}_j = 0.8$ and typical VCSEL parameters, Table 6.1	66
Figure 6.6: (a) Mode splitting experimental setup with beam analysis (at circle); (b) Block diagram of the dual receiver setup	69
Figure 6.7: Optical spectrum of VCSEL with overlaid captured modes	70
Figure 6.8: Cross-correlation between modes at 8mA (a) R_{12} ; (b) R_{23} ; (c) R_{13} . Delay offset is due to different signal path lengths of the two receivers	72
Figure 6.9: Simulated intensity profiles of (a) LP01 mode; (b) LP11 mode; and (c) LP21 mode for the 900nm VCSEL under study	74
Figure 6.10: Power penalty due to MPN versus Reach for a 5 mode VCSEL-based optical link at 25GBaud with RIN of -145dB/Hz and normalized variance in the dominant mode of 2.7×10^{-3} (a) For OOK modulation; (b) For PAM-4 modulation	77
Figure 7.1: (a) Link setup for PAM-4; (b) Eye diagram at TP1	83
Figure 7.2: VCSEL spectrum when biased at 25Gbit/s, 6.1mA	84
Figure 7.3: L-I-V characteristics of the VCSEL	85
Figure 7.4: 25.78GBaud at 850nm for Btb links using NRZ and PAM-4	88
Figure 7.5: 25.78GBaud using PAM-4 at 850nm: (a) OM3 MMF performance; (a) OM4 MMF performance	90
Figure 7.6: 25.78GBaud at 1050nm: (a) Btb links using NRZ and PAM-4; (b) Wideband fiber (WBF) performance	92
Figure 7.7: 25.78GBaud using PAM-4 at 1050nm: (a) OM3 MMF performance; (b) OM4 MMF performance	93

Figure 7.8: Bit rates up to 66Gbit/s at 1050nm using PAM-4	94
Figure 7.9: Performance comparison of 850nm and 1050nm PAM-4 links at 25.78GBaud: Fiber penalty at BER $\sim 10^{-12}$ for 100m MMF with EMBc	95
Figure 7.10: (a) Unmodulated RIN spectra for various bias currents; (b) L-I-RIN for the 900nm VCSEL	98
Figure 7.11: 50Gbit/s PAM-4 for a) btb at 7.5mA bias; b) 100m of three standard OM4 fibers at 8.5mA. c) 100m of one standard OM3 fiber at 8.5mA	99
Figure 8.1: Schematic of the experimental setup	103
Figure 8.2: Test setup used for VCSEL characterization	104
Figure 8.3: VCSEL spectrum when biased at 15mA and modulated at 25Gbit/s	104
Figure 8.4: L-I-V Curves for the VCSEL	105
Figure 8.5: Test setup for measuring DMD	108
Figure 8.6: De-convolved and normalized DMD plots for the POF with amplitude of each pulse in (a) Linear scale; (b) dB scale; (c) A sample single pulse magnified to show ripple and non-Gaussian nature	110
Figure 8.7: BER of 100m POF before and after equalization using 5-tap and 9-tap FFE112	
Figure 8.8: Illustration of the channel estimation technique	114
Figure 8.9: Response of the 100m GI-PF-POF channel	115

LIST OF ABBREVIATIONS

VCSEL	Vertical cavity surface emitting laser
FP	Fabry-perot laser
MMF	Multi-mode fiber
SMF	Single mode fiber
PMMA	Polymethyl metacrylate
(GI) PF-POF	Gradient index perflourinated plastic optical fiber
DMA	Differential mode attenuation
MC	Mode coupling
CD	Chromatic dispersion
MD	Modal dispersion
DMD	Differential mode delay
EMBc	Calculated effective modal bandwidth
MCDI	Modal and chromatic dispersion interaction
PAM	Pulse amplitude modulation
OOK	On-off keying
ISI	Inter-symbol interference
RIN	Relative intensity noise
MPN	Mode partition noise
MN	Modal noise
PRBS	Pseudo-random bit sequence
BER	Bit error rate
O-A	Ogawa-Agrawal model

MPD	Mode power distribution
BLW	Baseline wander
MLSE	Maximum likelihood sequence estimation
FFE	Feed-forward equalizer
FIR	Finite impulse response
TIA	Trans-impedance amplifier
BW	Bandwidth
TEC	Thermo-electric controller
OMA	Optical modulation amplitude
ER	Extinction ratio
PSD	Power spectral density
CSD	Cross-spectral density
COV	Covariance matrix
TE	Transverse electric
TM	Transverse magnetic
EA	Error analyzer
SER	Symbol error rate
SNR	Signal-to-noise ratio
WBF	Wideband fiber
TOSA	Transmitter optical sub-assembly
ROSA	Receiver optical sub-assembly
VOA	Variable optical attenuator

SUMMARY

Ever since the first successful demonstration of the fiber-optic systems in 1977, commercial systems have been using multimode fibers (MMF) for short reach applications as the preferred medium of transmission due to their relative ease of use compared to the single-mode fibers (SMF) [70]. In short reach applications such as the datacenters, the constraints due to the cost and complexity of deployment drive the choice of associated technology. VCSEL-based MMF optical links offer a cost-effective solution to the growing demand for bandwidth today with the large core MMF relaxing the requirement of high-end optics at the transmitter and receiver. Recently, the IEEE802.3bs task force has adopted 25Gbit/s per wavelength on VCSEL-MMF links to achieve 400GbE, with the future goals for short reach applications heading towards 100Gbit/s per wavelength. State-of-the-art VCSEL technology limits intensity-modulation based links to be below 50Gbit/s even after using reasonable signal processing. Thus, advanced multi-level signaling techniques that can pack more bits per symbol need to be explored and implemented in VCSEL-MMF links for achieving speeds $> 100\text{Gbit/s}$. At such higher speeds with tight power budgets, optimum link designing calls for a thorough understanding of the penalties due to the impairments. Hence, advanced modeling tools are indispensable.

This research aims at addressing the two aspects mentioned above:

- 1) A thorough understanding of the individual impairments in the future VCSEL-MMF links with speeds approaching 100Gbit/s and their temperature dependencies. In particular, high speed VCSEL links using multi-level modulation schemes such as PAM-

4, the mode partition noise (MPN) penalty can be a major limiting factor for the link reach, making its accurate modeling critical. This work develops a physical yet simple model for estimating MPN penalty accurately in multi-transverse mode VCSEL-MMF links. The model is based on the noise-inclusive spatio-temporal form of the rate equations that describe the mode power evolution inside a VCSEL with the spontaneous emission noise in carrier and photon populations modeled through the Langevin sources. Direct experimental verification of the new model is then presented with detailed discussions on the quantitative impact on the link designing. In addition, advanced simulation tools for capturing the impact of modal and chromatic dispersion interaction (MCDI) on the link performance are developed; additionally, temperature dependencies of individual link penalties for 25Gbit/s OOK links at 850nm are studied experimentally.

2) Statistical analysis of PAM-4 based multimode fiber (MMF) links with > 50Gbit/s speeds is presented using VCSELs at 850nm and 1050nm across a wide range of fiber profiles with EMBc spanning from 2GHz.km to 10GHz.km. To our knowledge, this is the first such study using 850nm to 1050nm VCSELs performed on MMFs whose alpha profiles span across the wide range of EMBc. Error-free transmission of 51.56Gbit/s is demonstrated over a set of standard OM3 and OM4 fibers up to reaches of 150m with no error-correction (FEC) and 300m at FEC-conformed BER using 850nm and 1050nm VCSELs. Further, using a prototype wide band fiber (WBF) that is specially designed to operate between a wide band of 850nm and 1100nm, error-free transmission at 62Gbit/s is also demonstrated with 100m reach. Individual link penalties are extracted through a comparison with the end-to-end analytic link model and results are compared for 850nm

and 1050nm links, providing insights into the advantages and challenges in moving to longer wavelengths for bitrates $> 50\text{Gbit/s}$ using PAM-4.

In addition, plastic optical fiber (POF) based VCSEL-MMF links and the impact of electronic equalization on them is also analyzed for 25Gbit/s and higher speeds.

CHAPTER 1

HIGH SPEED MULTIMODE FIBER OPTICAL LINKS

Short range optical communications links are needed for a variety of applications including data centers and high performance computing. A plot of the growth in the bandwidth demand with time in the short reach networks, Fig. 1.1 [1], reveals that the data rates almost double every two years. In order to keep up with this increasing demand there is a need to increase the data rates; various standards have been developed by the

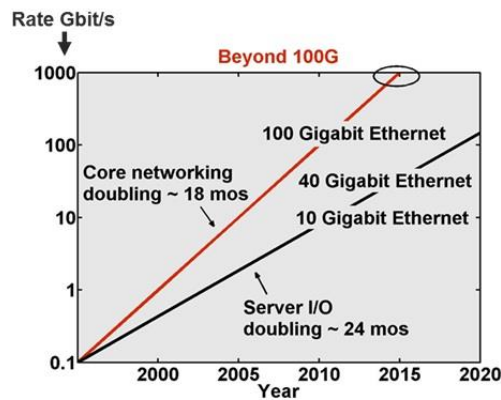


Fig. 1.1. Trend in the increase of bandwidth demand for short reach and long haul networks [1]

IEEE 802.3 study group [2]. Standards include 40Gbit/s and 100Gbit/s using 4 and 10 lanes respectively of 10Gbit/s links comprised of OM3 and OM4 multimode fiber (MMF). These low-cost implementations use direct modulation of VCSELs with MMF. The emerging 100GBASE-SR4 standard uses 25G VCSELs over four lanes of MMF at a data rate of 25.78125G to allow forward error correction (FEC) [3]. The 100G MMF standard responds to the need for higher density front panel interfaces and the need to reduce the cost and power of 100G optics and cabling.

Compared to the long-haul networks which consist of SMF optical links, the VCSEL-based MMF links cannot use advanced signal processing algorithms due to cost

and complexity considerations and hence are very sensitive to various impairments in the link. The most important impairments in the MMF links are due to the ISI effects such as chromatic dispersion (CD), modal dispersion (MD), non-ideal rise-time of the VCSEL, limited receiver bandwidth and noise impairments such as relative intensity noise (RIN) of the VCSEL, mode partition noise (MPN) due to VCSEL-MMF combination, thermal noise, electrical amplifier noise and shot noise at the receiver. While the CD is caused due to the wavelength dependence of the refractive index of the fiber, the MD arises out of the relative delays between the different optical paths in the fiber and is determined by the alpha profile of the graded index (GI) MMF.

MPN and RIN are related to the noise characteristics of a VCSEL. RIN represents intensity fluctuations in the composite power output of a VCSEL and is a power-dependent multiplicative noise. It is independent of the channel response. MPN on the other hand occurs due to a combination of the mode power fluctuations among different lasing modes in a VCSEL and the dispersive element in the link, typically the fiber. The correlated random fluctuations among the VCSEL transverse modes combined with the differential mode delays (DMD) due to the CD and MD of the MMF causes random timing jitter in the received pulse. This bounded random jitter which is termed as MPN is then measured as intensity fluctuations at the sampling instant at the receiver [4].

1.1 Types of MMF

With the development of perflourinated (PF) plastic optical fiber (POF) that exhibits significantly lower attenuation than polymethyl-methacrylate (PMMA) near 1 μ m wavelength, POF based MMF links emerged as an alternate to silica based MMF links.

Table. 1.1. Comparison of Glass fiber and GI-POF based MMF links

	Glass fiber MMF links	GI-POF MMF links
Attenuation	Very low (<1dB/km)	Moderate (~40dB/km)
Differential mode attenuation	Very low	High
Mode coupling	Low	High
Modal bandwidth (EMBc)	Excellent (EMBc > 4.7GHz-km)	Good (EMBc ~ 2GHz-km)
Core size	50micron	55-120micron
CD at 850nm	~ -100 ps/(nm-km)	~ -90 ps/(nm-km)

Recent studies in multimode fiber systems focused on using graded index (GI) PF-POF based links due to the ease of fiber preparation and simplicity in termination [5][6]. While this ease of connectorization makes GI-POF a better choice for high data rate short-reach applications, there are some challenges that need to be addressed in the POF links. Table 1.1 shows some of the basic differences between glass fiber and GI-POF based MMF links:

1.2 Moving Towards 100Gbit/s per Lambda for VCSEL-MMF Links

The future deployment of 200G and 400G systems will require supporting short reach MMF solutions, preferably using as few fibers as possible. Thus there exists a need to increase the bit rate to 50Gbit/s while retaining the benefits of direct intensity modulation, direct detection and MMF [3]. Although VCSELs have been reported with >50Gbit/s using on-off keying modulation [7], the capability to robustly support

>50Gbit/s is limited. Thus, as was done in single mode long haul environments, there is a need to implement advanced modulation formats that support multiple bits per symbol. PAM-4 has been demonstrated to support 32Gbit/s [8] using 850nm VCSELs. In particular, reaches up to 50m at 50Gbit/s [9] and 200m at 30Gbit/s [10] have been shown to be possible at 850nm.

The focus of this research is to develop advanced modeling tools to accurately simulate end-to-end VCSEL-based MMF links for data rates reaching 100Gbit/s. In particular, this work reports advanced simulation tools to estimate the performance of high speed MMF links that will accurately take into account the effect of modal and chromatic dispersion interaction (MCDI) on the link penalties such as ISI and MPN. This research reports a new comprehensive model for MPN and RIN that is more accurate for the VCSEL-MMF links compared to the existing MPN model being used by the IEEE 802.3 standards group. The new model is a comprehensive physical yet simple-to-use model for estimating MPN penalty accurately in multi-transverse mode VCSEL-MMF links. It is based up on the spatio-temporal form of the rate equations that describe the mode power evolution inside a VCSEL with the Langevin noise sources added to represent the noise due to the spontaneous emission in carrier and photon populations. The MPN and RIN characteristics of the VCSEL are represented through a normalized covariance matrix (COV) which is further reduced to the three VCSEL-specific parameters α , Γ_p , and k_n . Direct experimental measurement of VCSEL output mode fluctuations achieved through a spatial filtering of 900nm VCSEL modes using spectrometer validate the predictions and the accuracy of the model assumptions.

In addition, this work presents experimental demonstrations showing error-free transmission of up to reach of 300m MMF at bitrates $> 50\text{Gbit/s}$ using multilevel PAM-4 modulation format at wavelengths of 850nm, 1050nm and 900nm. As will be discussed in detail in Chapter 7, longer wavelength VCSEL-MMF links outperform the corresponding 850nm links due to reduced dispersion if wide bandwidth fibers are used. Further, dependence of ISI and noise penalties for high speed short reach VCSEL-MMF links on temperature and bias currents is also investigated for OOK and PAM-4 links.

The rest of the document is organized as follows: Chapter 2 will outline the various assumptions underlying the IEEE 802.3 model for 10Gbit/s VCSEL-based MMF links and corresponding limitations. Chapter 3 will describe the state of the art in the field of VCSEL-based high speed MMF optical link designing. Chapter 4 will describe the advanced end-to-end VCSEL-MMF link models that are developed for the 100Gbit/s links and in Chapter 5, the end-to-end analytic link model is used along with experimental measurements to study the temperature behavior of VCSEL-MMF link penalties including ISI and noise. Chapter 6 discusses the new MPN model, developed to replace the existing IEEE standard model for VCSEL-MMF links, with experimental validation. Chapters 7 and 8 present PAM-4 based high speed experimental demonstrations of $> 50\text{Gbit/s}$ using VCSELs around $1\mu\text{m}$ and investigation of POF-based high speed VCSEL links. Chapter 9 will provide a summary of the findings and discuss future scope in the direction of this work.

CHAPTER 2

IEEE 802.3 MODEL FOR 10GBIT/S VCSEL-MMF LINKS

In an effort to model the short reach MMF-based optical links, the IEEE 802.3 study group developed a simplified end-to-end MMF optical link model, Fig. 2.1, for bit rates up to 10Gbit/s [2]. This spreadsheet based analytic model characterizes the end-to-end link with closed-form penalty calculations for individual link impairments including

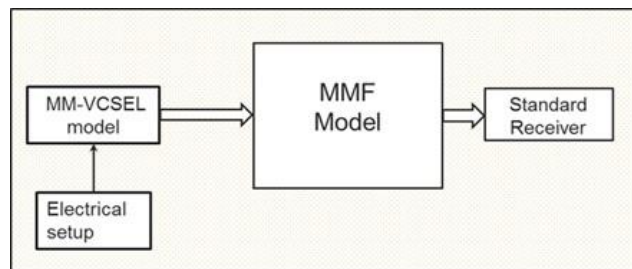


Fig. 2.1. Block diagram of the IEEE 802.3 analytic model for end-to-end link with bitrates up to 10Gbit/s.

various ISI effects and noise sources both in the optical and electrical domains. This model makes several simplifying assumptions on the end-to-end link, the most notable being [11]:

1. MMF link response:

Impulse response for the laser, MMF and the optical receiver channel are all approximated to be Gaussian.

2. Modal and chromatic dispersion interaction (MCDI) effects:

The IEEE spreadsheet model assumes the modal and chromatic dispersion effects are independent of each other and calculates the ISI penalty due to each effect separately. For bitrates of 25Gbit/s and higher, the MCDI effects play a crucial role in the net ISI penalty seen in the links. Also, since the currently deployed MMF is optimized at 850nm,

as we move to longer wavelengths, the MD penalty and thus the MCDI effects become significant.

3. MPN and RIN:

The IEEE 802.3 spreadsheet model treats RIN and MPN independently. It uses Ogawa-Agrawal (O-A) model for MPN penalty calculation [12]. This involves several simplifying assumptions which do not hold for real VCSEL-MMF links. For instance, the VCSEL spectrum is assumed to be continuous Gaussian while the received pulse shape is assumed to be an ideal raised-cosine. More importantly, the MPN penalty calculation treats the link to be an SMF link with multi-mode VCSEL. Hence any MCDI effects that influence the MPN calculations are also not taken into account.

These assumptions work quite accurately for MMF optical links with bitrates up to 10Gbit/s, and this model has been used quite effectively for several years by the optical link designers across the world. However, for bitrates 25Gbit/s and higher, the symbol period reduces significantly resulting in the ISI and noise effects becoming prominent. In particular, the ISI due to MD in the fiber, along with the CD, limits the reach of the link. Thus, the interaction between the modal and chromatic dispersion effects (the MCDI effects) become significant and cannot be neglected for assessing the link performance. Also, the symbol duration at these high bitrates is shorter than the impulse response of the fiber and the Gaussian model for these fiber links is no longer an accurate representation of the MMF channel. In addition, the MPN model used currently in the IEEE 802.3 spreadsheet model is insufficient for several reasons, which will be discussed in detail in subsequent sections.

Owing to these limitations, there is a need for a comprehensive numerical model that is a more accurate representation of the end-to-end MMF optical links at high bitrates. As part of this research, an end-to-end full physical simulation model was developed that generates and physically propagates pseudo-random bit sequences (PRBS) through an end-to-end MMF optical link with all the impairment and noise effects [13]. The performance of the end-to-end link is then evaluated through a direct counting of the BER at the receiver. This advanced full physical simulation model makes use of the Georgia Tech mode solver [14], which numerically calculates the excited fiber guided mode groups for an arbitrary alpha profile of an MMF with the corresponding modal delays and their coupling coefficients. The GT end-to-end MMF link simulator replaces all the simplifying assumptions discussed previously with a more realistic representation of the link, giving more accurate predictions on the performance of VCSEL-based end-to-end MMF links. In addition, it includes a new model to characterize RIN and MPN simultaneously in VCSEL-MMF links that is more accurate than the simplistic O-A model for MPN [15].

CHAPTER 3

PRIOR ART

3.1 Link Penalties in High Speed MMF Links: Temperature Dependence

The growing demand for bandwidth in short reach optical links has resulted in a need to increase the data rates of multimode fiber links [16], [6]. As long-haul and metro fiber optic links have begun deploying 100Gb/s systems, the need to upgrade short-reach optical links for local and storage area networks to keep pace has prompted the development of 40/100 Gigabit Ethernet (GbE) standards. One prominent standard in development is 100GBASE-SR4, utilizing four parallel ~25 Gb/s lanes with vertical cavity surface emitting lasers (VCSELs) over multimode fiber (MMF). Some recent investigations on VCSEL-based MMF links have indicated that the MPN penalty is a limiting noise factor for realizing longer reaches of MMF links [17]. In fact, the IEEE 802.3bm standards link model uses a worst-case k_{mpn} parameter of 0.3 which makes the MPN penalty contribution significant to the total penalty of the link [2]. For this reason, it is important to study the MPN characteristics of VCSELs and factors affecting it in more detail. MMF must be treated from a statistical perspective due to variations in modal bandwidth that result from the interaction of the VCSEL-launched fiber mode power distribution (MPD) with the fiber's differential modal delay (DMD), both of which exhibit significant variation while remaining within their respective specifications [18, 19]. It has been reported that the intensity noise and MPN for Fabry-Perot based MMF links are highly dependent on the laser MPD and so vary dramatically with the drive conditions, in particular with the temperature [20].

Commercial high-speed VCSELs all employ multiple quantum wells and apertures large enough for multiple transverse modes which compete for gain in the active region, resulting in mode fluctuations [21, 22]. It is known that the VCSEL spectrum and thus the MPD and its fluctuations vary with temperature [11]. Also, the collection apparatus that couples light from the VCSEL output at the transmitter is sensitive to temperature changes which results in the fiber MPD being temperature dependent. Since the MPN is a result of the interplay between the MPD fluctuations and the fiber DMD, we expect the VCSEL MPN to be dependent on temperature. Furthermore, it is known that the transmitter's directly-modulated VCSEL characteristics, including output power, spectral content, RIN and mode partition factor k , all depend on both drive conditions and VCSEL operating temperature in addition to device structure, in part due to polarization mode switching instabilities [23]. Thus it is justifiable to be concerned about potential link failures due to MPN for specific temperatures as the VCSEL mode power fluctuations may experience local maxima over the desired operating temperature range.

3.2 Mode Partition Noise in VCSEL-Based MMF Links

The performance of VCSEL-based optical links is mainly limited by the penalty due to dispersion and penalty due to the noise in the VCSEL output. VCSEL noise has two aspects to it; 1) Fluctuations in the composite power output or the relative intensity noise (RIN) and 2) Random fluctuations of optical power among different transverse modes of the VCSEL. The multi-mode nature of low-cost VCSELs used in data centers and LANs results in random fluctuations among the different transverse modes due to mode competition [24] [25]. These random fluctuations then manifest as a random timing

jitter due to the wavelength-dependence of the group velocity which is different for different modes. This random jitter results in an amplitude variance at the optimal sampling instant, and is referred to as Mode Partition Noise. Ogawa [24] proposed, via simplifying assumptions, a simple model to estimate the variance due to MPN in single-mode and multi-mode fiber links which was then used by Agrawal [12] to derive closed-form expressions for the power penalty due to MPN under additional idealizing assumptions. This extended Ogawa-Agrawal (O-A) model is the basis for the model used by the IEEE standards group to estimate high-speed VCSEL-based MMF link performance [25]. It uses major simplifying assumptions which are not valid for VCSELs:

- 1) The composite power in all modes of a laser at any given instant in time is constant

$$\sum_{i=1}^N a_i = 1 \quad (3.1)$$

In other words, the MPN is treated independently to the RIN.

- 2) The cross-correlation parameter, γ_{cc} of the power fluctuations between any two modes of the laser is constant

$$\gamma_{cc} = \frac{\langle a_i a_j \rangle}{\langle a_i \rangle \langle a_j \rangle} = \text{constant for all } i \neq j \quad (3.2)$$

- 3) The power in a given mode remains constant throughout the duration of a bit period.

The variance for the normalized power in each mode is thus calculated by the O-A model in a heuristic manner following above assumptions [26] without any consideration of the physical basis of how the modes actually fluctuate inside a laser. For a VCSEL however, the lasing transverse modes continuously compete for gain in the active region. Consequently, the extent of intensity overlap between the spatial distributions of any two modes is a primary factor determining the cross-correlation

coefficient (r_{ij}) of those modes. Thus, the random fluctuations among different VCSEL modes result from a complicated interaction of mode profile and various mode-coupling mechanisms. Also, these correlations in the mode power fluctuations impact the value of RIN for the device. Thus, each of the assumptions 1) - 3) are violated when the standard MPN model is applied for VCSELS.

Another assumption in the O-A model for MPN is that the modes in a VCSEL are all anti-correlated. Recent experiments [27] showed different k_{mpn} measured from the statistics in each transverse mode of an 850nm VCSEL, contrary to the standard model assumption. Similar experiments have measured the correlated fluctuations between polarization modes of a VCSEL [28], and correlations between transverse modes of an optically injected VCSEL [29].

Studies on the RIN of single-mode lasers were done using the rate equations and adding Langevin noise sources to them [39], [40]. VCSEL mode dynamics and hence its noise behavior differs from the analysis of longitudinal semiconductor lasers since it outputs multiple transverse modes with different spatial profiles. The VCSEL mode dynamics had been studied extensively using the spatio-temporal model of the rate equations [41], [42], [43] [44]. Though few attempts have been made using the Langevin approach for the noise analysis of VCSELS, they were mostly focused on single mode cases which required an analysis of only the autocorrelation of the lasing mode [22], [45], [46], [40]. No comprehensive analytical modeling was reported for the multiple transverse mode VCSELS, which require a thorough analysis of the cross-correlations as well as autocorrelations of individual modes to accurately characterize the VCSEL noise. Importantly, the numerical models developed using the Langevin approach on VCSELS

did not incorporate the impact of the non-uniform gain profile in the spatial overlap integrals of the VCSEL transverse modes [45], [46]. It will be shown mathematically that the non-uniform gain profile of the VCSEL active region will impact the cross-correlations by deriving closed-form expressions incorporating the overlap of the mode spatial profiles and the gain profile of the active region where the modes compete for the available overall gain.

3.3 High Speed Experimental Demonstrations of VCSEL-MMF Links

Current low cost implementations of short reach communication links use direct modulation of VCSELs with MMF. The emerging 100GBASE-SR4 standard uses 25Gbit/s VCSELs to achieve 100Gbit/s using four MMF lanes. However, for the deployment of 200G and 400G systems, there is a need to increase the capacity of the system while controlling the density of the front panel interface and also the cost and complexity of the system. Thus, it is essential to increase the bit rate in a single MMF to 50Gbit/s per wavelength while retaining the benefits of direct intensity modulation, direct detection and MMF.

VCSEL-MMF links with bitrates $>50\text{Gbit/s}$ have been reported in the past using OOK modulation [7], but the capability to robustly support $> 50\text{Gbit/s}$ is limited. Advanced modulation formats like the multilevel modulation schemes that support multiple bits per symbol, offer a practical solution. In particular, PAM-4 has been demonstrated to support 32Gbit/s [8] using 850nm VCSELs. So far, reaches up to 200m at 30Gbit/s [10] and 50m at 50Gbit/s [9] were demonstrated at 850nm. The reach for these links was mainly limited by the CD penalty at 850nm, since the new OM4 fibers exhibit very high bandwidth properties. Thus, moving to longer wavelengths where the

dispersion penalty for glass fiber is reduced seems helpful. Longer wavelength solutions using InGaAs VCSELs near 1micron have been proposed. The active layers are strained, resulting in large differential gain and higher modulation bandwidths for these VCSELs. Advances in this technology have enabled 1050nm VCSEL-based MMF links with high reliability [3]. One potential problem with links at longer wavelengths is the fiber DMD which would be high for the standard OM3 and OM4 fibers at wavelengths other than their optimal operation point, i.e., 850nm. To counter this issue, specialty fibers have been proposed which are designed for operation in broadband region, i.e., at wavelengths from 850nm to 1100nm.

3.4 25Gbit/s POF Links and Impact of Electronic Equalization

The recent advances in manufacturing [51]-[53] and understanding [54]-[56] of plastic optical fiber (POF) as a medium for multigigabit optical systems and their inherent advantage in the ease of preparation and connectorization make POF-based links well-suited for short-reach applications at bitrates of 25Gbit/s and above [6], [51]. The

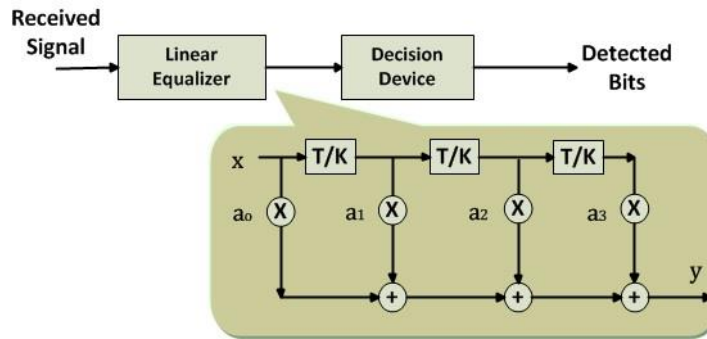


Fig. 3.1. Block diagram of fractional spaced FFE.

development of perflourinated (PF) POF has enabled high-speed VCSEL-based links due to the lower attenuation values compared to the PMMA-POF in the 850nm band [16], [6]. Indeed the IEEE 802.3 study group on MMF, 100G-SR4 standard is considering 25Gbit/s

per channel using 850nm VCSEL-based transceivers [22]. Robust performance may require equalization techniques to compensate for the penalties incurred due to various sources of inter-symbol interference (ISI) which become more significant at 25Gbit/s. Error-free transmission of VCSEL-based GI-PF-POF optical links at 25Gbit/s have been previously demonstrated by us with a reach of 100m [57] without equalization at the receiver end. In this work, the link penalties are analyzed and it will be shown that simple fractionally-spaced analog linear equalizers (Fig. 3.1) having a modest tap-length yield a significant improvement in performance. High-speed 100m POF links are typically loss limited due to the higher attenuation compared to silica-based MMF links [5]. This increases the requirements to minimize ISI penalties. The degradation of an MMF link is caused by a number of impairments which contribute to a power penalty that can be reduced to some extent by strategic signal processing at the receiver. The two impairments can be categorized mainly into: 1) ISI causing effects such as CD, DMD, BLW, limited bandwidth of the transmitter and the receiver; and 2) Noise effects such as receiver noise, RIN and MPN.

The power penalty due to the ISI caused by deterministic effects such as dispersion, DMD and BLW can be compensated for by electronic equalization of the received signal by a simple FIR-based feed-forward equalizer (FFE) structures with modest number of taps. The power penalty due to the ISI caused by deterministic effects such as dispersion, DMD and BLW can be compensated for to some extent by strategic signal processing at the receiver [14].

Although significant work has been reported on the performance improvement achieved using electronic equalization in silica-based MMF links [14], [58], [59], the

impact of equalization of high-speed GI-PF-POF links is not well documented. POF DMD is strongly influenced by the high mode coupling (MC), 4-5 orders of magnitude stronger than that found in silica fibers [5]. This yields a POF impulse response which generally has less temporal structure than that observed from silica fibers and the impact of low complexity equalizer structures is expected to be different from that experienced with silica fiber.

Equalization of POF links with reach up to 100m has been demonstrated using a complex MLSE equalizer structure [60]-[62] and a linear FFE structure with a large tap length [61]-[63], which makes the implementation impractical for low cost applications. Recently, there have been reports of equalization of POF links using modest tap-length FFE structures at 10Gbit/s using 1mm-large core step index PMMA-POF with reach below 35m [64], [65].

CHAPTER 4

END-TO-END VCSEL-MMF LINK MODELING FOR 100GBIT/S

4.1 Full Physical Simulation Model

An advanced numerical model was developed for simulating the end-to-end high speed MMF links. This full physical simulation model generates and propagates several ISI bit patterns through the end-to-end MMF link with all possible physical effects included [13]. The link performance is then evaluated through a direct error counting of the received bits by the sampling and decision circuit at the receiver.

A schematic of the end-to-end simulation model is shown in Fig. 4.1. The physical ISI effects included in this model are the limited bandwidth of the VCSEL, finite extinction ratio and the non-ideal response of the transmitter, DMD of the MMF, CD,

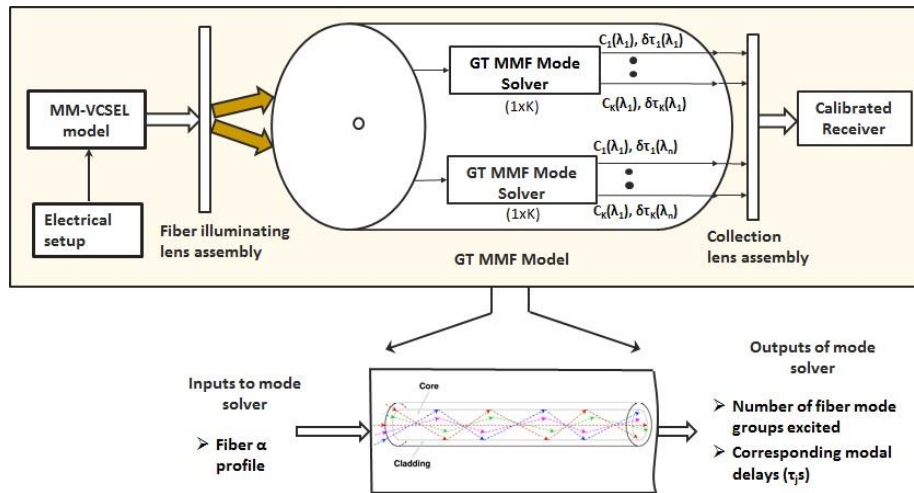


Fig. 4.1. Block diagram of the full physical simulation model for end-to-end link with bitrates > 25Gbit/s.

BLW effects due to the receiver AC-coupling filter and the limited bandwidth at the receiver. The noise effects include the receiver thermal noise, amplifier noise and shot noise along with the VCSEL RIN and MPN.

The end-to-end MMF link simulation model consists of the following main components:

- i. Multimode-VCSEL model: The multimode VCSEL model is a simple behavioral VCSEL model that outputs optical power spread across multiple transverse modes for a given electric drive signal. The output is assumed to follow the drive signal ideally and all the modes turn ON and OFF simultaneously. The VCSEL noise effects, namely the RIN and inter-mode power fluctuations (resulting in MPN in the link) are accurately incorporated in the model. The VCSEL output mode field is assumed to be that of Gaussian LP modes. The finer details of the physical modal dynamics inside a VCSEL (like the mode power dependence on bias current) are however not included in this model.
- ii. GT MMF mode solver: The GT MMF mode solver is an important component in this end-to-end MMF link simulation model. It was developed at the Terabit optical networking consortium lab by K. Balemarthy et al., [14] for accurately calculating the supported guided mode groups in a fiber for an arbitrary alpha profile. For a given VCSEL L-P mode incident on an MMF with an arbitrary alpha profile, the mode solver calculates the mode shapes of all the excited guided mode groups and corresponding coupling coefficients and modal delays. In this work, the GT MMF mode solver has been incorporated in the end-to-end MMF link simulation model in such a way that for a given VCSEL launch mode power distribution and the MMF alpha profile, all excited guided mode groups with respective coupling coefficients and the group delays are calculated. The group delays include both the modal delays and the chromatic delays which are calculated from the corresponding wavelengths of each mode group.

- iii. **GT MMF Model:** The GT MMF model uses the modal and chromatic group delays calculated from the VCSEL-GT MMF mode solver combination and implements the net delay for each fiber mode group in the frequency domain. The net delay is calculated by algebraically adding the modal and chromatic group delay values calculated from the fiber alpha profile and the corresponding wavelength of each mode group. Thus, the end-to-end MMF link simulation model accurately takes into account the MCDI effects arising out of the fiber alpha profile and the VCSEL MPD for the given launch conditions at the input of the fiber. The resultant power samples corresponding to each mode group are separately propagated with the net delays through the length of the MMF.
- iv. **Calibrated receiver model:** The last component of the link simulation model is the photo receiver model, consisting of the cascade of photodiode, the trans-impedance amplifier (TIA), an electrical amplifier followed by the decision circuit. The individual mode groups at the end of the MMF are incident on the photodiode through a collection lens assembly that emulates any mode-selective coupling at the receiver end which are then combined to give the composite electrical pulse. The receiver model further calculates the BER through a direct error counting of the received bits. This receiver model is calibrated with the receiver setup present in our test-bed to replicate the lab measurements for further analysis.

4.1.1 Noise Modeling

Noise modeling of the end-to-end VCSEL-based MMF links is critical since the performance of these links at high bitrates is limited by the transmitter and receiver noise sources. The noise in the end-to-end link mainly consists of the following sources:

- i. **Thermal noise from the TIA at the receiver:** Its standard deviation, σ_t is calculated as

$$\sigma_t = \sqrt{4kT\Delta f F_n / R_l} \quad (4.1)$$

Where ‘k’ is the Boltzmann constant [$\text{m}^2.\text{kg}.\text{s}^{-2}.\text{K}^{-1}$], ‘T’ is the temperature [$^{\circ}\text{K}$], ‘ Δf ’ is the receiver bandwidth [Hz], ‘ F_n ’ is the noise figure of the TIA in linear units and ‘ R_l ’ is the load resistor [Ω].

- ii. Shot noise due to quantum nature of light: Its standard deviation, σ_{sh} is given by

$$\sigma_{\text{sh}} = \sqrt{2q(RP_{1/0} + I_d)\Delta f} \quad (4.2)$$

Where ‘q’ is the electron charge [Coulomb], ‘R’ is the responsivity of the photodiode [A/W], ‘ $P_{1/0}$ ’ is the incident optical power [Watt] and ‘ I_d ’ is the dark current of the receiver [Amp].

- iii. VCSEL RIN which is the composite power fluctuations of the VCSEL output: The standard deviation due to RIN, σ_{RIN} is given by

$$\sigma_{\text{RIN}} = RP_{1/0}r_I \quad (4.3)$$

Where ‘ r_I ’ is the normalized std. dev. due to RIN and is related to the RIN parameter [dB/Hz] through

$$r_I = \sqrt{10^{\text{RIN}/10} * \Delta f} \quad (4.4)$$

- iv. MPN in the VCSEL-MMF link: The correlated random mode power fluctuations, when experiencing dispersive effects in the link, result in random timing jitter in the pulse at the receiver, which is known as the mode partition noise. MPN is measured at the sampling instant of the received pulse as an amplitude fluctuation.

The IEEE 802.3 model for MPN is based on a simplified model developed K. Ogawa in 1982 for Fabry-Perot based fiber links [24]. This model makes some idealizing assumptions on the laser mode power fluctuations which are not applicable to VCSELs as will be discussed in section 4.4. The IEEE 802.3 model incorporates MPN penalty based

up on the Ogawa's model for MPN, by making additional simplifying assumptions like the continuous Gaussian spectrum, SMF link with no modal dispersion and raised-cosine shape for the received pulse [12].

Our physical simulation model has two versions: One with the MPN added according to Ogawa's model, but without the additional simplifying assumptions mentioned above. This is done through a VCSEL model that generates transverse mode powers with variance given by the Ogawa model as follows:

$$\text{Var}\{a_i\} = k^2_{\text{mpn}}(\langle a_i \rangle - \langle a_i \rangle^2) \quad (4.5)$$

Here, $\{a_i\}_{i=1-N}$ represent the normalized VCSEL mode powers corresponding to modes with wavelengths $\{\lambda_i\}_{i=1-N}$ with mean $\{\langle a_i \rangle\}_{i=1-N}$ such that $\sum_{i=1}^N a_i = 1$. RIN is added separately to the composite power output of the VCSEL, according to Eq. (4.3).

The other version of the simulation model includes the new model for capturing MPN and RIN simultaneously in the VCSEL-based MMF links, using a single covariance matrix that describes the statistics of the mode power fluctuations, the details of which are elaborated in the subsequent sections.

In summary a full physical simulation model was presented to simulate high speed end-to-end VCSEL-based MMF optical links that is more accurate than the IEEE 802.3 spreadsheet model for speeds $> 25\text{Gbit/s}$. The simulation model particularly accounts for the impact of MCDI effect on the link, both on the fiber induced ISI penalty and also on the MPN penalty in the end-to-end optical link. It also removes the Gaussian impulse response assumption on the MMF channel and uses a more realistic MMF model based on the accurate modal and chromatic delays for any arbitrary alpha profile of the

GI-MMF. In addition, it overcomes the limitations of the O-A model for MPN used by IEEE 802.3 model.

4.2 IEEE 802.3 Conformed Analytic Model

Apart from the full physical simulation model described in the previous section, a simple analytic model was also developed to estimate the performance of the end-to-end MMF optical links. This analytic model predicts the performance of the end-to-end optical link through an estimation of BER starting from the standard Q-factor equation given by

$$Q = \frac{RP_{oma}}{\sigma_1 + \sigma_0} \quad (4.6)$$

The noise standard deviations for the 1 and 0 bits (σ_1 and σ_0) are equivalent to those used in the IEEE 802.3 link budget model. The standard deviations for the thermal noise, shot noise and the RIN are as given by equations (4.1) through (4.3). The standard deviation due to MPN in the optical link is given by

$$\sigma_{RIN} = RP_{1/0} r_{mpn} \quad (4.7)$$

Where r_{mpn} is the normalized standard deviation due to MPN and is given by

$$r_{mpn} = \frac{k}{\sqrt{2}} (1 - e^{-\pi BLD\sigma_\lambda^2}) \quad (4.8)$$

This equation assumes continuous Gaussian spectrum, raised cosine shape for the received pulse and SMF model for the optical channel. The full-blown Q-factor equation is given by

$$Q = \frac{RP_{oma}}{\sqrt{\sigma_{Rx}^2 + (Rr_{mpn}P_{oma})^2 \left(\frac{ER}{ER-1}\right)^2 + (Rr_{RIN}P_{oma})^2 \left(\frac{ER}{ER-1}\right)^2 + \sigma_{Rx}^2 + (Rr_{mpn}P_{oma})^2 \left(\frac{1}{ER-1}\right)^2 + (Rr_{RIN}P_{oma})^2 \left(\frac{1}{ER-1}\right)^2}} \quad (4.9)$$

All the ISI effects in the end-to-end link are included by the P_{oma} term in the equation (4.9) through an eye-closure penalty E_{ook} , which reduces the P_{oma} . The ISI impairments are due to the laser and receiver bandwidths, CD, MD, baseline wander and any other filtering effects in the link. The end-to-end link performance is then estimated from the BER calculated from the Q-factor through the standard equation

$$\text{BER} = 0.5\text{erfc}\left(\frac{Q}{\sqrt{2}}\right) \quad (4.10)$$

The analytic model has been developed for mainly the following reasons: 1) Readily estimate the performance of the end-to-end MMF links for very low BER ranges ($< 10^{-9}$) to a good accuracy for the cases when the MCDI effects and the MPN penalties are not dominant. 2) To compare the discrepancy in the prediction of IEEE 802.3 spreadsheet model in cases where MCDI effects and the MPN penalty are significant. 3) Extract out the ISI penalty and the noise parameters in the end-to-end link through a best fitting of the analytic model to the experimental measurements for back-to-back and fiber link cases. The ISI penalty then gives an estimate of parameters such as the CD, fiber EMBc and the VCSEL bandwidth, while RIN and MPN can be extracted out from the noise parameter estimation. Some of these results are discussed in the experimental results section.

4.3 Comparison Between Full Physical Simulation Model Versus Analytic Model

Fig. 4.2 gives a comparison between the full physical simulation model and the analytic model. When the bitrate is 10Gbit/s, the physical simulation model prediction matches very well with the analytic model for various cases of MPN, Fig. 4.2a. Note here that the VCSEL spectrum, shown in the figure 4.2 inset, is assumed to be Gaussian with an RMS spectral width of 0.55nm with the center wavelength at 849nm. The VCSEL

RIN is assumed to be $\sim -133\text{dB/Hz}$ and various values of k_{mpn} spanning from 0 to 0.6. The VCSEL is modulated using a PRBS-7 sequence at an ER of 3.5dB. Different lengths of MMF with a dispersion parameter of -117ps/nm.km and an EMBc of 10GHz-km have been simulated. The receiver has a sensitivity of -10.7dBm P_{avg} at a BER of 10^{-6} . The physical simulation results agree well with the analytic results for various combinations of the fiber length and k_{mpn} , as seen in Fig. 4.2(a).

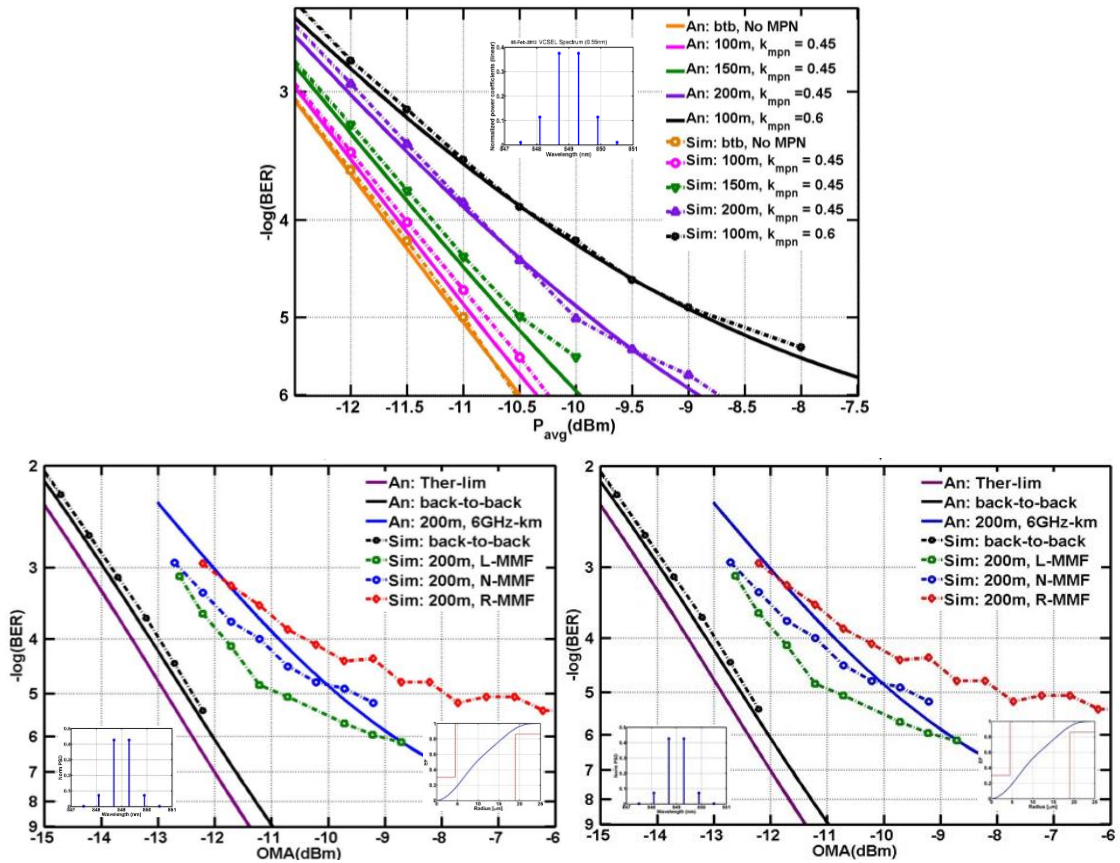


Fig. 4.2. Comparison between full physical simulation model and IEEE 802.3 conformed analytic model at (a) 10Gbit/s for varying MPN; (b) 25Gbit/s with no MPN; (c) 25Gbit/s with MPN.

The MPN model used in the analytic model assumes continuous Gaussian spectrum and SMF link. When the bitrate is increased to 25Gbit/s, there is a slight discrepancy in the predicted performance of analytic model compared to the physical simulation model. Results for a 200m MMF with an EMBc of 6GHz-km and no MPN are

shown in Fig. 4.2(b). The discrete Gaussian spectrum and the encircled flux of the simulated VCSEL, which conforms to the IEEE 10GbE specification, are shown in the figure inset. Here, the VCSEL with a RIN of -140dB/Hz is modulated using PRBS-7 sequence.

The unstressed sensitivity of the receiver used in the models is -11.5dBm OMA at a BER of 10^{-9} . The physical simulation results show a penalty difference of up to ~ 0.5 dB for different fiber alpha profiles with the same EMBC but with the opposite DMD slopes (under-compensated, optimum profile and over-compensated profiles). Further, the IEEE 802.3 based analytic model overestimates the fiber ISI penalty by about 0.3dB when compared to the physical simulation results corresponding to the optimum alpha profile. When MPN is added, the discrepancy in the predictions of the model increases further, Fig. 4.2(c). There is a mismatch in the slopes of the BER plots of the two models, due to the difference in the variances due to the power-dependent MPN. Similarly, there is also a bigger deviation between the under-compensated and over-compensated fiber alpha profiles.

CHAPTER 5

INVESTIGATION OF VCSE-MMF LINK PENALTIES

5.1 25Gbit/s Link Penalties at 850nm: Temperature Dependence

Recent investigations of VCSEL based MMF links have shown that mode partition noise (MPN), which is a variation in observed group delay resulting from the interaction of laser mode power fluctuations and dispersion, is a limiting noise factor for longer reaches of MMF links [2]. In fact the IEEE 802.3bm standards group, responsible for the 100GBASE-SR4 standards link model, uses an MPN penalty which is the dominant penalty at longer reach [3].

A simplified model for MPN in Fabry-Perot (FP) based links which characterizes MPN through a single laser-specific parameter k was first proposed by Ogawa [4, 5]. Although the Ogawa model may not be completely appropriate for VCSEL links [6], it does yield a BER noise floor and this model is used to bind the MPN k parameter, thereby comparing these results directly with the previous work done within the IEEE standards efforts. The MPN and RIN for FP based MMF links are highly dependent on the laser mode power distribution (MPD) and hence may vary dramatically with drive conditions, and in particular with temperature [7]. Similarly high-speed VCSELs all support multiple transverse modes which compete for gain resulting in mode power fluctuations [8, 9]. Furthermore, it is known that directly-modulated VCSEL characteristics, including output power, spectral content, RIN and mode partition parameter k [10], all depend on drive conditions and VCSEL operating temperature in addition to device structure, in part due to polarization mode switching instabilities [11,

12].

Thus it is important to investigate the temperature dependence of the primary link impairments. In particular, it is justifiable to be concerned about potential link failures due to MPN and its temperature dependence, as the VCSEL mode power fluctuations may experience local maxima over the desired operating temperature range.

MMF links must be treated from a statistical perspective due to variations in performance that result from the interaction of the VCSEL-launched fiber MPD with the fiber's differential modal delay (DMD), both of which exhibit significant variation while remaining within their respective specifications [13, 14, 15]. The results of an experimental study reported here explore the bit error ratio (BER) and penalty for 25Gbit/s VCSEL-MMF links operating across 150m of three examples of OM4 fiber and two spectrally distinct VCSELs as a function of VCSEL operating temperature. From the BER performance and a comparison with the end-to-end analytic link model discussed earlier, the individual penalties including the MPN penalty have been extracted as a function of the VCSEL operating temperature. The random jitter arising out of the differential delays of the fluctuating VCSEL modes shows up as amplitude fluctuations at the optimal sampling instant which affects the BER measurement. Hence the MPN extracted out of the BER performance is accurate. MPN is found to be negligible and RIN and chromatic dispersion (CD) are found to be the dominant impairments for 25Gbit/s VCSEL-based MMF links of 150m.

5.2 Experimental Setup

The link BER, optical spectrum, eye diagrams and associated metrics were recorded via an automated experimental setup, Fig. 5.1. The VCSELs used are pre-

commercial 25G prototypes provided by EMCORE’s VCSEL division (since acquired by Sumitomo). The VCSELs are mounted on a thermo-electric cooler (TEC), enabling wide temperature control. The VCSEL’s active region temperature will be somewhat higher than the reported TEC surface temperature, T_{VCSEL} . The VCSEL output was collected via a commercial 10GbE transmitter optical sub-assembly lens positioned with a precision-mechanical translation stage.

Collection was adjusted for optimum power. The custom receiver incorporated an InGaAs PIN photodiode having 20 μ m diameter with responsivity $\sim 0.36A/W$ at 850nm and TIA on a laser-etched board with >25 GHz bandwidth. The receiver and drive electronics have sufficient bandwidth, so the back-to-back (btb) response is primarily determined by the VCSEL bandwidth. The MMF power splitter and variable optical

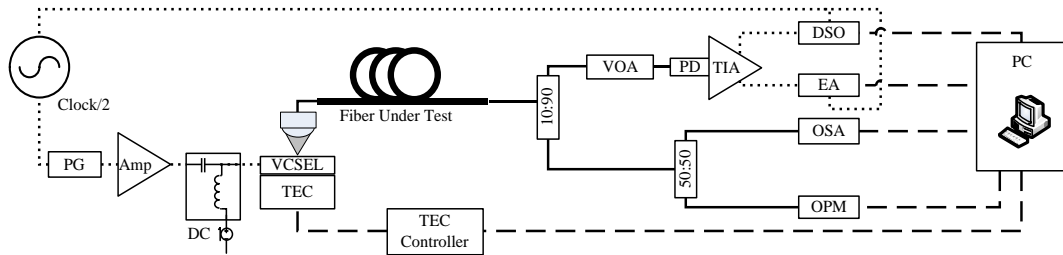


Fig. 5.1. Automated measurement setup. DSO: Digital Sampling Oscilloscope; EA: Error Analyzer; OPM: Optical Power Meter; OSA: Optical Spectrum Analyzer; PD: Photo-Diode; PG: Pattern Generator; TEC: Thermo-Electric Cooler; TIA: Trans-Impedance Amplifier; VOA: Variable Optical Attenuator.

attenuator at the receiver allowed accurate control and assessment of the received power without influencing launch condition. The PRBS pattern length used in these experiments is $2^{15}-1$.

The three fibers used in this study were all standard OM4-grade fibers of 150m length; one very high bandwidth fiber with $\sim 10,000MHz\cdot km$ calculated effective modal bandwidth (EMBc) (“std-OM4-1”), and two OM4 fibers (“std-OM4-2” and “std-OM4-

3”) having EMBc values of $\sim 5700\text{MHz}\cdot\text{km}$ and $\sim 5200\text{MHz}\cdot\text{km}$ respectively at 850nm and having peak EMBc at different wavelengths.

The two VCSELs used have significantly different spectral characteristics: “VCSEL A” has four primary modes and a spectral width (at the nominal bias current) which ranges from 0.54nm at 20°C to 0.4nm at 70°C, while “VCSEL B” has five primary modes and a spectral width which ranges from 0.74nm at 20°C to 0.4nm at 70°C. The

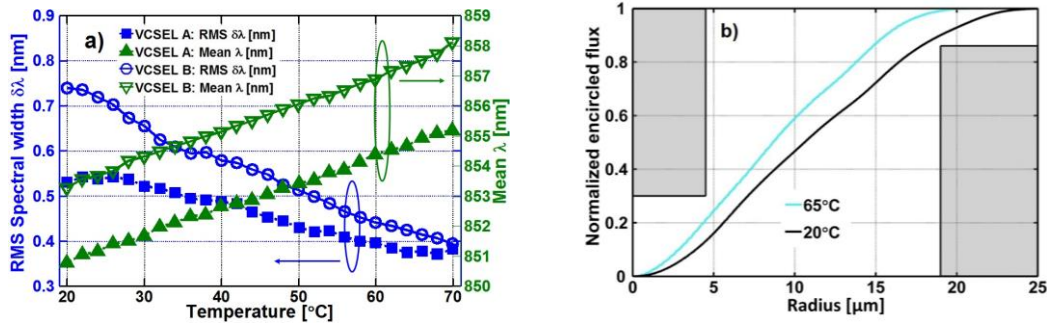


Fig. 5.2. a) Spectral width and mean wavelength vs. VCSEL temperature at nominal bias current 8.4mA, b) Extrema of total encircled flux observed at 20 and 65°C for VCSEL B, are compliant to 10Gigabit Ethernet restrictions; too tightly confined (hot inside) and too spread out (hot outside) mode powers are prohibited as indicated by the shaded regions.

spectral width *decreases* and systematically redshifts with increasing temperature for both the VCSELs, Fig. 5.2a, under the conditions of constant bias current and modulation voltage. The launched encircled flux (EF) was separately measured and found to conform to the 10GbE specification across the entire temperature range from 20 to 70°C. The EF for VCSEL B at the extrema, hottest outside at 20°C and hottest inside at 65°C is shown in Fig. 5.2b.

5.3 Estimation of Link Penalties using the End-to-end Analytic Link Model

The analytic link model predicts the performance of an end-to-end MMF link by calculating the BER resulting from all possible noise variances and all possible ISI effects including laser and receiver bandwidths, CD, DMD, baseline wander and finite

ER of the transmitter. The variances are added assuming each is an independent Gaussian noise source. The link Q-factor and BER are then determined. The BER calculations are consistent with the IEEE 802.3bm link budget model for 25Gbit/s MMF links [3]. A detailed description of the model is provided in the Appendix. Note that the model determines the MPN penalty based solely on CD neglecting the DMD, as per the IEEE 802.3bm link model. Depending on whether the modal dispersion adds or subtracts with the CD penalty, the exact value of the MPN might be slightly higher or lower. However, the fibers used here each have high EMBc and the DMD penalty is shown to be small compared to the CD. Thus the CD-based MPN calculation is accurate. Results of the analytic model are compared to the experimental results and through best fitting of these results, the noise parameters including RIN and MPN are systematically estimated along with the power penalties due to individual ISI impairments. The noise figure of the receiver was measured separately and the ISI penalty due to receiver bandwidth was calculated from the measured receiver bandwidth. The corresponding unstressed receiver sensitivity at BER 10^{-12} is $\sim -10.8\text{dBm OMA}$. Using this known receiver sensitivity in the analytic model, a best-fit to the experimental data was determined for the btb case by allowing the ISI penalty due to VCSEL bandwidth and the RIN to be free parameters. Note that the ISI penalty shows up as a constant shift of the BER data while the RIN which results in a noise floor, will generally appear as a changing slope when plotted versus power OMA. Thus, these two parameters (RIN and ISI penalty) can be uniquely determined by matching the analytic model with the btb experimental results. RIN is a power dependent penalty and leads to a noise floor, thus the slope variation from the thermal limit is determined by the RIN and a pure OMA penalty is determined by the net

ISI penalty. Using these parameters determined from the btb performance and the fiber performance results the ISI penalties resulting from CD and DMD can be accurately determined. MPN also results in a noise floor and results in a similar impact on the BER slope when present. Therefore, since the RIN is relatively the same with fiber added, the appearance of a noise floor or the “flattening” of the BER slope compared to the btb case would indicate significant MPN.

5.4 Results: Temperature Dependence of Back-to-Back and 150m Link Penalties

5.4.1 Back-to-Back

For each VCSEL the BER versus received OMA was measured for T_{VCSEL} from 20 to 70°C in 2 degree increments using a fixed bias and modulation voltage. The btb case, which is inherently free of MPN and chromatic dispersion, for VCSEL A ($T_{VCSEL} =$

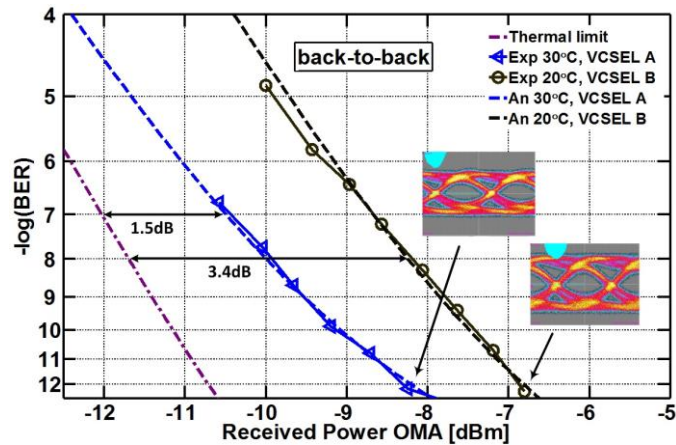


Fig. 5.3. Back to back performance at 25Gbit/s for VCSEL A at $T_{VCSEL} = 30^\circ\text{C}$ and B at $T_{VCSEL} = 20^\circ\text{C}$. Analytic model (dotted lines) reveals a combined RIN and bandwidth penalty of $\sim 1.5\text{dB}$ for VCSEL A and $\sim 3.4\text{dB}$ for VCSEL B near a BER of 10^{-8} .

30°C) is shown together with the btb performance with VCSEL B ($T_{VCSEL} = 20^\circ\text{C}$), Fig. 5.3, with sample eye diagrams at $\sim -8.2\text{dBm}$ and $\sim -6.8\text{dBm}$ OMA respectively. The T_{VCSEL} chosen for Fig. 5.3 correspond to the best BER performance for each VCSEL.

The corresponding link sensitivities at BER 10^{-12} are $\sim -8.2\text{dB}$ and $\sim -6.8\text{dB}$ for VCSEL A and B respectively, which are consistent with 25Gbit/s 850nm VCSELs without transmitter pre emphasis [16, 17]. The analytic best fit for VCSEL A revealed an ISI penalty of $\sim 0.8\text{dB}$ and a RIN of -135dB/Hz . These penalties are with respect to the separately measured ideal thermal limit of our receiver. For VCSEL B, an ISI penalty of $\sim 2.8\text{dB}$ and a RIN of -140.5dB/Hz is found. This corresponds to a total penalty of $\sim 3.4\text{dB}$ near a BER of 10^{-8} . The higher RIN of VCSEL A is readily apparent from the reduced BER slope compared to that of VCSEL B. This also shows the sensitivity of the BER slope to RIN thus enabling good assessment of the RIN parameter. The ISI penalties extracted from the model in btb cases allow an estimate of the combined VCSEL-receiver bandwidth. Since the receiver bandwidth of 28GHz results in negligible penalty for a 25Gbit/s system, the btb ISI-penalty is mostly due to the VCSEL bandwidth.

For VCSEL A, a bandwidth of $\sim 17\text{GHz}$ was estimated, while for VCSEL B it was $\sim 11.6\text{GHz}$. A set of representative BER versus temperature are shown in Fig. 5.4a, and 5.4b. The performance of the btb case typically exhibited increasing penalty with

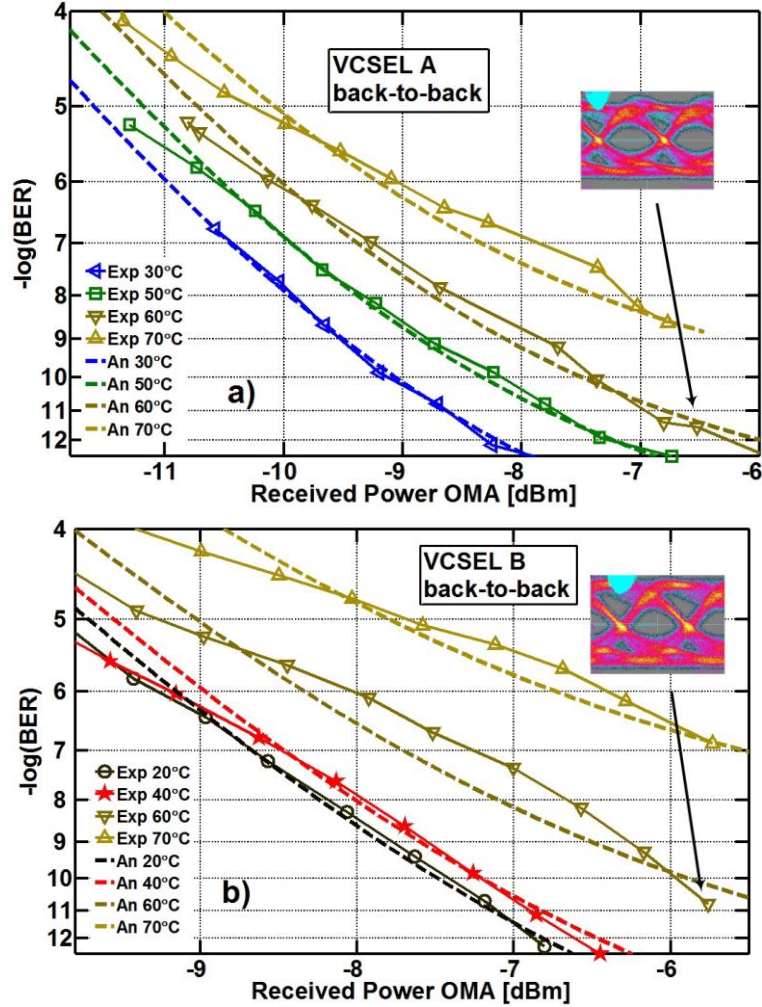


Fig. 5.4. BER vs. OMA for btb cases for a range of operating temperatures of (a) VCSEL A and (b) VCSEL B. Best fit analytic model (dash lines) reveals RIN and bandwidth effects for btb.

increasing temperature for both VCSELs A and B as expected for constant bias and modulation. The observed BER performance together with the eye diagrams and power measurements reveal *i*) the optical power decreases and the RIN increases monotonically with increasing T_{VCSEL} [18] for both VCSELs and *ii*) the VCSEL bandwidth generally decreases with increasing T_{VCSEL} leading to a higher ISI penalty although the optimum

bandwidth is near 30°C for VCSEL A and near 20°C for VCSEL B. Representative eye diagrams of both VCSELs at 60°C are shown. The measured ER varied slightly from 3.5dB at $T_{VCSEL} = 20^{\circ}C$ to ~3.2dB at higher temperatures. Note that the impairments are less severe and the model fits are better for $T_{VCSEL} < 60^{\circ}C$ particularly for VCSEL B.

Examination of the 70°C performance for VCSEL A reveals that the RIN and ISI penalty have increased from -135dB/Hz and ~ 0.8dB to -133.5dB/Hz and ~ 1.5dB compared to the 20°C case. For VCSEL B, the RIN increases from -140.5dB/Hz at 20°C to -136.5dB/Hz at 70°C and the ISI penalty increases from ~2.8dB to ~3.6dB. Note that re-optimization at each T_{VCSEL} yields an improved performance at the higher temperatures.

5.4.2 150m OM4 Fiber Links

The link performance for the three 150m OM4 fibers was next examined, with each VCSEL over the entire 20°C to 70°C range with specific attention to any increase in MPN. As mentioned, the ISI penalties from the btb results have been used as measures of the VCSEL and receiver performance which remain the same when fiber is added to the link. The total ISI penalty is expected to increase with fiber added, the net impact determined by the fiber EMBc and CD. The BER performance for a range of T_{VCSEL} for two of the six fiber-VCSEL combinations examined are shown in Fig. 5. The ER is ~3.5dB for all cases. The 5,200MHz-km fiber (std-OM4-3) with VCSEL A, Fig. 5.5a and the 10,000MHz-km fiber (std-OM4-1) with VCSEL B, Fig. 5.5b. For all six combinations, a well behaved BER vs OMA performance was observed with no dramatic increase in noise floor. Thus, independent of the precise model fitting, the absence of any increase in noise floor demonstrates that MPN remains low for all temperatures

investigated. By fitting the end-to-end analytic model results with the following constraints, the quantitative metrics of the link impairments were extracted; ISI due to

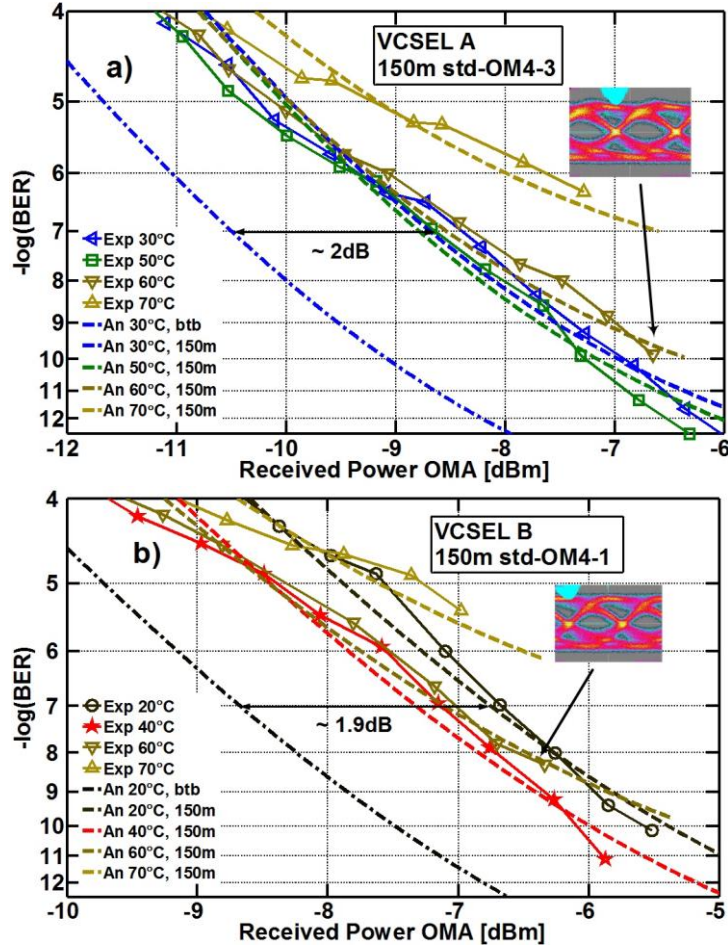


Fig. 5.5. BER vs. OMA for a range of operating temperatures for two of 6 cases examined (a) VCSEL A with 150m 5200MHz-km fiber and (b) VCSEL B with 150m 10,000MHz-km fiber. CD, DMD and MPN effects are revealed from the btb and 150m best fits of analytic model (dotted lines).

limited BW of Tx and Rx are determined via the btb data. Initially the RIN was restricted to be no greater than that observed in the btb case. MPN is added if the RIN is not sufficient to accurately fit the data at low BER. After identifying the total ISI penalty the constituent parts of the ISI were then determined.

Examination of the 5,200MHz-km fiber with VCSEL A performance, Fig. 5.5a, reveals a total additional link penalty of $\sim 2\text{dB}$ with $T_{\text{VCSEL}} = 30^\circ\text{C}$. The 10,000MHz-km

fiber with VCSEL B, Fig. 5.5b, exhibits an additional penalty compared to its corresponding btb performance at $T_{\text{VCSEL}} = 20^{\circ}\text{C}$ of $\sim 1.9\text{dB}$. Importantly, the additional link penalty is essentially independent of BER. Thus the observed fiber impairment is a pure OMA penalty (shift) in the BER result compared to the btb. The measured penalties of the 6 VCSEL-fiber combinations at two representative temperatures are listed in Table 5.1.

Table 5.1. Measured penalties of the 6 VCSEL-MMF combinations at 2 representative temperatures

T_{VCSEL}	VCSEL	Measured fiber Penalty [dB]			Computed CD penalty [dB]
		OM4-1	OM4-2	OM4-3	
20°C	A	0.8	1.6	1.5	1.1
	B	1.9	2.0	2.5	1.8
50°C	A	0.4	1.1	0.8	0.5
	B	1.1	1.8	1.5	0.7

With the known fiber dispersion and VCSEL spectral parameters, our analytic model predicts an ISI penalty of $\sim 1.1\text{dB}$ for VCSEL A links and $\sim 1.8\text{dB}$ for VCSEL B links due to CD alone and a small modal dispersion penalty of $< 0.5\text{dB}$ for the three fibers at 20°C . Interestingly, the CD penalty decreases with T_{VCSEL} since the VCSEL spectral width decreases with temperature. Note that the computed ISI penalty due to CD exceeds the measured ISI penalty. This is understood by recognizing that CD and modal penalties may either add or compensate depending on the sign of the modal delay. i.e., whether higher order modes are either faster or slower than lower order modes. All penalties have an uncertainty of $\pm 0.25\text{dB}$.

All of the link data with fiber for both VCSELs exhibit a slightly lower RIN, $\sim 1\text{dB/Hz}$, compared to the same conditions exhibit in btb. This is likely as a result of the decreased reflected power back into the VCSEL when fiber is added. With the 150m

fiber added, the signal experiences an optical fiber path of length 300m. With the attenuation at 850nm $\sim 2.8\text{dB/km}$, the total loss due to the addition of the fiber is $\sim 1\text{dB}$. At this operating point of BER, the back reflections begin to have significant impact on the signal noise, so the reduced amplitude fluctuations due to the back reflections from the receiver will reduce the RIN value slightly ($\sim 1\text{dB/Hz}$ in this case). For example, the analytic fit at 60°C reveals a RIN of -135.3dB/Hz which is $\sim 0.8\text{dB/Hz}$ better than that for the btb at the same T_{VCSEL} . This marginal change in the RIN results in a slight increase in slope which is systematic for all the temperatures. This issue can be overcome by using a receiver with very less reflection coefficient.

The analytic model best fits the experimental BER data for all the 150m fiber cases for the two VCSELs when only allowing for the predicted additional penalty due to CD and modal dispersion to the btb results with no additional noise penalty. This constrains the MPN penalty to be small and implies a k parameter below 0.1 [5]. As noted, MPN is a power dependent penalty and thus creates a noise floor. For the link parameters here, ER and RIN most importantly, significant MPN would create an easily observable change to the BER compared to the btb. Furthermore, the MPN penalty remained stable across the range of VCSEL temperatures examined with no observable anomalies in the MPN. Note here that these results are specifically for VCSEL based links and cannot be readily extrapolated to FP based links. The laser physics underlying the output mode power fluctuations and the corresponding laser-fiber coupling are significantly different for the FP laser and VCSEL. Hence a separate examination of FP based links is required to characterize the impact of MPN in such links.

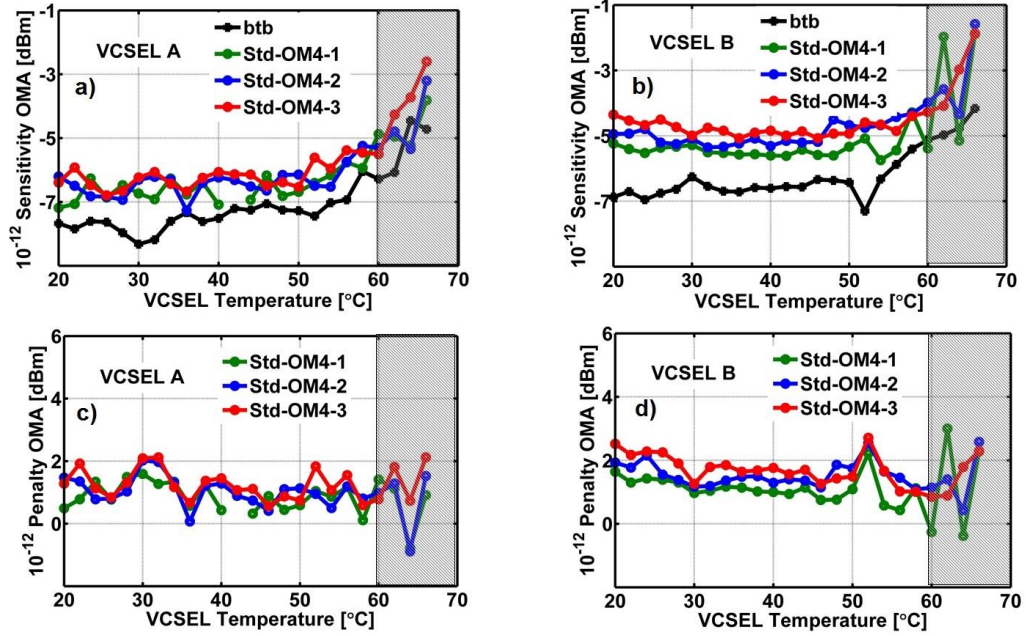


Fig. 5.6. Link sensitivity and penalty with respect to btb at BER 10^{-12} versus VCSEL temperature. There is no temperature where a significant increase in penalty is observed that could be associated with increased MPN. The apparent peak at 52°C for VCSEL B is due to an anomalous drop in the corresponding btb ISI penalty and data $> 60^{\circ}\text{C}$ is extrapolated and has relatively larger uncertainties. There is a systematic decrease in penalty with increasing temperature resulting from decreasing spectral width and a corresponding decreasing CD penalty.

Thus, it can be concluded that the majority of the link penalty observed in 150m OM4 links is due to CD with a modest additional modal dispersion penalty (that for some fibers compensates the CD) and MPN penalty that remains low for all VCSEL temperatures. All the analytic fits are substantially better than the worst case shown in Fig. 5a for the 70°C VCSEL A link.

Link sensitivities more clearly reveal changes in link performance with temperature. Therefore, the link sensitivities at BER 10^{-12} were determined for the btb and the three fibers for both VCSELs, Fig. 5.6a, and 5.6b. For T_{VCSEL} above 60°C , where a BER of 10^{-12} was not achievable due to power limitations, the available data was extrapolated by performing a fit to the BER vs. OMA results for each fiber, which are all qualitatively similar to those of Fig. 4 and Fig. 5. As discussed, the analytic model

reveals RIN/MPN through a best fit with the measured BER vs. received power. Furthermore this fit is very sensitive to the RIN/MPN and thus provides good estimates of both. For $T_{\text{VCSEL}} < 66^\circ\text{C}$, the best fits do not show an error floor for $\text{BER} > 10^{-12}$. Thus, it is justified to extrapolate experimental data to BER of 10^{-12} for T_{VCSEL} between 55°C and 66°C . Further, the extrapolated sensitivity/penalty data for each of the 6 VCSEL-fiber combinations agrees well with the analytic model predictions for $T_{\text{VCSEL}} < 66^\circ\text{C}$, with the extrapolated power levels being within 2dB of the measured power. This extrapolation however creates a relatively larger uncertainty in the determined sensitivities for T_{VCSEL} above 60°C (shaded region in Fig. 5.6a and 5.6b).

In the btb configuration the sensitivity is relatively constant with VCSEL temperature for T_{VCSEL} up to $\sim 55^\circ\text{C}$ at $\sim -7.5\text{dBm}$ for VCSEL A and $\sim -6.9\text{dBm}$ for VCSEL B. Above 55°C , the sensitivity decreases steadily. The previous analytic model fits attribute this increase in penalty to RIN and ISI at the higher temperatures. Importantly, the changes in sensitivity of the fiber links closely follow that of the back to back changes. This reflects the nearly constant RIN penalty and very low MPN.

The changes in sensitivity for the fiber cases are best shown via the OMA penalty, Fig. 5.6c and 5.6d. The penalties are larger for VCSEL B by $\sim 0.5\text{dB}$ to $\sim 1\text{dB}$, compared to VCSEL A at all VCSEL temperatures for the three fibers examined, primarily due to the larger CD penalty. Our link model confirms this observation; a change in spectral width from 0.54nm for VCSEL A to 0.74nm for VCSEL B at 20°C results in an increase in ISI penalty of $\sim 0.6\text{dB}$. For both VCSELs an increase in temperature results in a reduction in CD penalty, though this effect is more significant for VCSEL B due to its larger reduction of spectral width with temperature (0.74nm to 0.4nm) compared to

VCSEL A (0.54nm to 0.4nm). The std-OM4-1 fiber with the highest EMBc (~10,000MHz-km) performs the best for both VCSELs for all temperatures, followed by std-OM4-2 (EMBc~57,000MHz-km) and std-OM4-3 (EMBc ~5,200MHz-km). However, the overall difference between the penalties of the three fibers is < 0.5dB for both VCSELs. This supports the model results which show that the dominant fiber penalties arise from CD and ISI due to VCSEL bandwidth limitations.

In these studies, fixed bias and drive conditions, (optimized at 20°C) were used over the entire temperature range. However, commercial VCSELs are typically deployed with bias and drive conditions dynamically optimized for the operating temperature. These experiments were repeated with bias and drive conditions optimized at 68°C and found that the btb improves by ~ 1dB (corresponding to a total ISI penalty ~ 0.6dB) at 70°C. Again, in these additional measurements the MPN penalty remained low for all temperatures. Thus, when three fiber examples and two VCSEL samples were examined, a negligible and steady behavior of MPN was observed for the examined values of T_{VCSEL} with no anomalies. The contributions of all significant penalties have been quantitatively identified and MPN was shown to be negligible although the analytic models show that these links would readily reveal significant MPN. However, additional VCSEL samples should be examined, particularly from other vendors before concluding that all 25G compliant VCSELs exhibit stable MPN characteristics across a large range of VCSEL temperature.

CHAPTER 6

NEW MODEL FOR MPN BASED ON LANGEVIN-RATE EQUATIONS

The recent interest in the multilevel modulation formats for the short reach optical links to keep up with the ever-increasing bandwidth requirements of datacenter applications resulted in tighter budget allocations to the physical layer link impairments [30]. In fact, high-speed demonstrations using PAM-4 modulation at 50Gbit/s and higher have been reported using 850nm and 1050nm VCSELs for reaches up to 300m on standard OM4 and OM3 MMF [31], [32], [33] [34]. The performance of high-speed VCSEL-based PAM-4 optical links is mainly limited by the penalty due to dispersion and penalty due to the noise in the VCSEL output. The vertical eye-closure due to ISI that is a measure of the dispersion penalty in optical links is doubled for PAM-4 modulation compared to the conventional OOK (NRZ) modulation. Recent studies have shown that the impact due to the power-dependent VCSEL noise on the link performance is even higher compared to the OOK (NRZ) signaling [32], [33].

6.1 VCSEL Noise and MPN

Penalty due to VCSEL noise in optical links can be seen as having two different aspects; 1) Random fluctuations in the composite power at the output of the VCSEL, or the relative intensity noise (RIN) and 2) Correlations in the fluctuations of optical power among different transverse modes of the VCSEL. The multi-mode nature of low-cost VCSELs used in data centers and LANs results in random fluctuations among the different transverse modes due to mode competition [17]. When dispersion-inducing fiber is added to the link, these correlated fluctuations manifest as a random timing jitter due to

the wavelength-dependence of the group velocity which is different for different VCSEL modes. This random jitter results in an additional amplitude variance at the optimal sampling instant, and is referred to as mode partition noise (MPN).

When there is no dispersion in optical link, the variance due to RIN is the only power penalty due to the VCSEL noise for a back-to-back link. When fiber is added, the additional variance due to the differential delays in the correlated VCSEL mode power fluctuations imposes an additional penalty, called the MPN penalty. Ogawa [24], [26] proposed, via simplifying assumptions, a simple model to estimate the variance due to MPN in optical links using single-transverse-mode Fabry-Perot (F-P) lasers with low RIN and having multiple longitudinal modes. This was later extended by Agrawal [12] to derive closed-form expressions for the power penalty due to MPN in single mode fiber (SMF) links under additional idealizing assumptions. This extended Ogawa-Agrawal (O-A) model has been adopted without modifications by the IEEE 802.3 standards group to estimate high-speed VCSEL-based MMF link performance [2], [35]. Recent experiments revealed that the O-A model does not accurately describe the noise characteristics of a VCSEL-based optical link [15], [36], [37].

As will be discussed in the following sections of this chapter, the major underlying assumptions of the O-A model that were accurate for the single-transverse-mode F-P lasers, are not true for the present optical interconnects that are based on VCSELs having multiple transverse modes. The penalty estimations resulting from these simplifying assumptions are particularly inaccurate for next generation multi-level modulation links which are impacted significantly by the MPN. Thus, there is a need to improve on the existing O-A model for evaluating the effect of MPN on the performance

of the VCSEL-based optical links. Several attempts have been made recently to accurately model the MPN penalty for VCSEL-based links [15], [38], [36], [35]. However, a complete physical modeling of VCSEL noise that is based on the underlying rate equations, yet simple enough to be adopted by the IEEE 802.3 standards model, is described.

In this chapter, a comprehensive physical model for MPN in VCSEL-based fiber optic links that relaxes all the major assumptions of the O-A model without compromising on the mathematical simplicity is described. The new model is based on the correlations derived from the coupled spatio-temporal rate equations, representing the evolution and interaction of the transverse mode powers in multi-mode VCSELs with the Langevin noise sources added to represent the spontaneous-emission noise of the carrier and photon population. The Langevin approach for the rate equations had been widely used for the noise analysis of semiconductor lasers with single and multiple longitudinal modes [39], [40].

VCSEL mode dynamics and thus its noise characteristics differ from the longitudinal semiconductor lasers due to the unique spatial interaction of the multiple transverse modes of the VCSEL. The steady-state VCSEL mode dynamics which ignores the noise terms were studied extensively using the spatio-temporal rate equations [41], [42], [43] [44]. Though few attempts have been made using the Langevin approach for the noise analysis of VCSELs, they were mostly focused on single mode cases which required an analysis of only the autocorrelation of the lasing mode [22], [45], [46], [40]. No comprehensive analytical modeling was reported for the multiple transverse mode VCSELs, which require a thorough analysis of the cross-correlations as well as

autocorrelations of individual modes to accurately characterize the VCSEL noise. Importantly, the numerical models developed using the Langevin approach on VCSELS did not incorporate the impact of the non-uniform gain profile in the spatial overlap integrals of the VCSEL transverse modes [47], [46]. It will be mathematically shown that the non-uniform gain profile of the VCSEL active region impacts the cross-correlations by deriving closed-form expressions incorporating the overlap of the mode spatial profiles and the gain profile of the active region where the modes compete for the available gain.

6.2 Underlying Assumptions in the IEEE Standard O-A Model for MPN

The basis of the O-A model for MPN is the following major assumptions; 1) any given pair of modes are always anti-correlated (i.e., they have negative cross-correlation) and fluctuate with the same degree of anti-correlation. The O-A model defines a cross-correlation parameter between mode pairs, $\gamma_{cc} = \frac{\overline{a_i a_j}}{\bar{a}_i \bar{a}_j}$ which is assumed to be constant for a given laser. Here, $\overline{f(t)}$ is the time-average of a time-dependent function $f(t)$ and the instantaneous mode powers $\{a_i\}_{i=1}^M$ are normalized to their time-averaged versions, i.e., $\sum_{i=1}^N \bar{a}_i = 1$. This assumption was developed for use with single-transverse-mode lasers with a mode intensity profile that does not vary much with wavelength. In a VCSEL where the transverse modes compete for gain, the cross-correlation coefficient actually depends on the mode spatial intensity profiles over the gain region and is not the same for any two modes; Also, the higher RIN shows up as a positive correlation in each mode pair, thus making it possible for the γ_{cc} between the mode to be positive. Our new model allows the inter-modal fluctuations to vary based on the physical mode dynamics and

captures the MPN effects through fundamental parameters α , k_n and Γ_p ; 2) Laser RIN is independent of the link dispersion. This assumption allows the O-A model to calculate the MPN penalty separate from any RIN penalty by initially assuming RIN to be zero. Since the anti-correlated fluctuations do not contribute to the composite power fluctuations, RIN always shows up as positive correlations among VCSEL modes. When the VCSEL modes undergo relative group delays due to the fiber, these positive correlations will impact the random timing jitter much like the way anti-correlations do. Thus, the amplitude variance of the sampling instance of the received pulse will vary with RIN and the fiber dispersion. Since this is a dispersion-dependent effect, it is not sufficient to separately add the RIN penalty calculated for back-to-back link and leave it out while calculating the MPN penalty in the fiber link. It will be quantitatively shown how the new model incorporates this effect of RIN on the MPN penalty through standard RIN dB/Hz parameter. The COV matrix approach in the new model is generic and can be used to characterize the laser noise penalty in high-speed optical links using any multi-mode semiconductor laser. Using VCSEL mode correlations that are derived from the Langevin-based spatio-temporal rate equations, the COV matrix is further reduced to the VCSEL-specific parameters α , k_n and Γ_p .

Direct experimental measurements of 900nm VCSELS validate the assumptions made in our model on the covariance matrix elements. Also, unequal cross-correlations were measured between different mode pairs, including a positive correlation for modes 1 and 3. This contradicts the O-A model assumptions and is consistent with the new model predictions. Further, the experimental findings support the assumptions made on the Covariance matrix in the new model.

6.3 Langevin Noise-Driven Spatio-Temporal Rate Equations for VCSELs

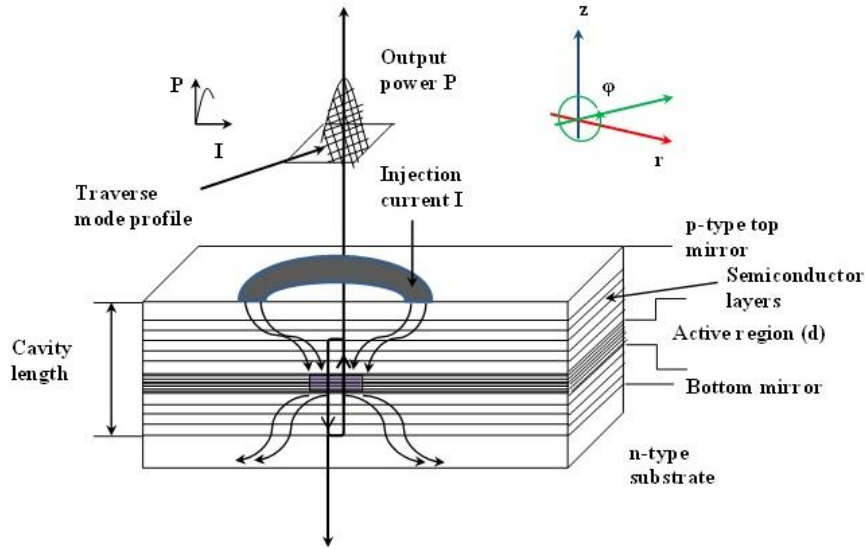


Fig. 6.1, Schematic of a VCSEL structure showing the important physical elements.

The schematic of a VCSEL with the working principle is shown in Fig. 6.1. Intensity noise in a VCSEL is a result of the quantum fluctuations of the spatially dependent carrier density and the photon population in each of the individual modes. Furthermore, the transverse modes spatially overlap in the active region and hence compete for the available gain. These spatial interactions of the VCSEL modes give rise to correlated fluctuations in the optical powers of the VCSEL modes. The quantum fluctuations can be modeled by adding the Langevin noise operators to the well-known laser rate equations. [39], [42], [22], [45], [47].

The instantaneous carrier density varies spatially (cylindrical coordinates with units cm^{-3}) and temporally. The noise-inclusive rate equations for the instantaneous carrier density $N(r, \varphi, t)$ [cm^{-3}] and the instantaneous photon number $P_i(t)$ of the i^{th} transverse mode are

$$\frac{dP_i(t)}{dt} = \left[G_i(t) - \frac{1}{\tau_{p,i}} \right] P_i(t) + \frac{\beta_i d \iint_0^{R_a, 2\pi} N(r, \varphi, t) r dr d\varphi}{\tau_n} + F_{p,i}(t) \quad (6.1)$$

$$\frac{\partial N(r, \varphi, t)}{\partial t} = \frac{I(t)}{qV_a} - \frac{1}{\tau_n} N(r, \varphi, t) - \sum_{k=1}^M A_k \psi_k^2(r, \varphi) g(r, \varphi, t) P_k(t) + F_n(t) \quad (6.2)$$

Cylindrical coordinates with CGS units are presumed. Here, v_g is the group velocity [cm/s], $A_k = \frac{\Gamma_k}{d}$ [1/cm] is a measure of the confinement of the k^{th} mode in the active region, with Γ_k representing the longitudinal confinement factor of the k^{th} mode and d , the total thickness of the gain region. $G_i(t)$ and $\tau_{p,i}$ are the modal gain and photon lifetime of the i^{th} VCSEL mode respectively, β_i is the fraction of the spontaneous emission injected into the i^{th} mode, τ_n is the carrier lifetime, q is the electron charge. $I(t)$ is the noiseless injection current and $V_a = \pi R_a^2 d$, is the volume of the gain region with radius R_a .

$\psi_k(r, \varphi)$ [1/cm] is the spatial intensity profile of the k^{th} transverse mode, normalized so that $\langle \psi_k^2(r, \varphi) \rangle_{r, \varphi} = \iint_0^{R_a, 2\pi} \psi_k^2(r, \varphi) r dr d\varphi = 1$. Here, the integral is over the cross-sectional area $A = \pi R_a^2$. For the rest of this chapter, $\langle \rangle_{r, \varphi}$ shall be used to represent the spatial integral operator. $g(r, \varphi, t)$ [1/s] is the gain given by

$$g(r, \varphi, t) = a_o v_g (N(r, \varphi, t) - N_t) \quad (6.3)$$

where a_o is the gain cross section in cm^2 , and N_t [1/cm³] is the carrier density at transparency. $g(r, \varphi, t)$ is related to the total modal gain $G_i(t)$, as

$$G_i(t) = \iint_0^{R_a, 2\pi} \psi_i^2(r, \varphi) a_o v_g (N(r, \varphi, t) - N_t) r dr d\varphi = \iint_0^{R_a, 2\pi} \psi_i^2(r, \varphi) g(r, \varphi, t) r dr d\varphi$$

(6.4)

Note that $G_i(t)$ is proportional to the degree of overlap between the mode spatial profile and the carrier density $N(r, \varphi, t)$ in the gain region. Eq. (6.2) represents the spatio-temporal evolution of the carrier distribution, where the spatial evolution is taken into account through the term $\psi_k(r, \varphi)$.

$F_{p,i}(t)$ [1/s] and $F_n(t)$ [1/cm³-s] are the zero-mean Langevin noise sources that characterize the quantum noise fluctuations of the i^{th} mode of the photon population and the carrier density respectively. Physically $F_{p,i}(t)$ arises from the spontaneous emission of the i^{th} mode photons while $F_n(t)$ has its origins in the spontaneous recombination and generation of the carriers. Note that the carrier recombination contains both radiative and non-radiative (Surface recombination or Augur recombination) events. Clearly, the correlation properties of the VCSEL mode powers depend upon those of the Langevin sources, described further in Appendix A.

Any additional noise sources such as optical reflections are neglected, thus noise is due to the spontaneous emission alone. The same methodology used in the RIN analysis of single-mode lasers has been followed, namely, linearization of the spatio-temporal rate equations via a perturbation analysis of the photon number and carrier density $\delta P_i(t)$ and $\delta N(r, \varphi, t)$ around their steady-state values $\overline{P_i(t)}$ and $\overline{N(r, \varphi, t)}$, the detailed in Appendix A.

Using the rate equations for the steady-state analysis and after neglecting the second order term $\delta G_i(t)\delta P_i(t)$, Eq. (6.1) results in

$$\frac{d\{\delta P_i(t)\}}{dt} = -\left(\frac{\beta_i d}{\tau_n \overline{P_i(t)}} \iint_0^{R_a, 2\pi} \overline{N(r, \varphi, t)} r dr d\varphi\right) \delta P_i(t) + \overline{P_i(t)} \delta G_i(t) + F_{p,i}(t) \quad (6.5)$$

Here, the initial assumption that $\delta N(r, \varphi, t) \ll \overline{N(r, \varphi, t)}$ has been used. Similarly,

perturbing Eq. (6.2) around the steady-state values of the carrier density and photon populations results in

$$\begin{aligned}
& \frac{\partial\{\delta N(r, \varphi, t)\}}{\partial t} \\
&= -\frac{1}{\tau_n} \delta N(r, \varphi, t) - \sum_{k=1}^M A_k \psi_k^2(r, \varphi) \overline{P_k(t)} \delta g(r, \varphi, t) \\
& \quad - \sum_{k=1}^M A_k \psi_k^2(r, \varphi) \overline{g(r, \varphi, t)} \delta P_k(t) + F_n(t)
\end{aligned} \tag{6.6}$$

6.4 Comprehensive Physical Model for VCSEL Noise From the Rate Equations

It is helpful to convert the partial differential equation to a regular differential equation in the differential modal gain $\delta G_i(t)$. This can be achieved by multiplying Eq. (6.6) with $a_o v_g \psi_i^2(r, \varphi)$ and integrating over the cross-sectional area $A = \pi R_a^2$ which gives

$$\begin{aligned}
& \frac{\partial\{\delta G_i(t)\}}{\partial t} = -\frac{1}{\tau_n} \delta G_i(t) - \frac{\delta G_i(t)}{G_i(t)} \sum_{k=1}^M \{a_o v_g A_k C_{fac} C_{ikg} \overline{P_k(t)}\} \\
& \quad - \sum_{k=1}^M a_o v_g A_k C_{fac} C_{ikg} \delta P_k(t) + a_o v_g F_n(t)
\end{aligned} \tag{6.7}$$

Here, $\{C_{ikg}\}_{i,k=1}^M$, denotes the normalized spatial overlap integral of the intensity profiles for the transverse modes i, k and the time-averaged spatial gain density $\overline{g(r, \varphi, t)}$, given by

$$C_{ikg} = \frac{\langle \psi_i^2(r, \varphi) \psi_k^2(r, \varphi) \overline{g(r, \varphi, t)} \rangle_{r, \varphi}}{\sqrt{\langle \psi_i^4(r, \varphi) \overline{g(r, \varphi, t)}^2 \rangle_{r, \varphi} \langle \psi_k^4(r, \varphi) \rangle_{r, \varphi}}} \quad (6.8)$$

$$C_{ikg} = \frac{\iint_0^{R_a, 2\pi} \psi_i^2(r, \varphi) \psi_k^2(r, \varphi) \overline{g(r, \varphi, t)} r dr d\varphi}{\sqrt{\iint_0^{R_a, 2\pi} \psi_i^4(r, \varphi) \overline{g(r, \varphi, t)}^2 r dr d\varphi \iint_0^{R_a, 2\pi} \psi_k^4(r, \varphi) r dr d\varphi}} \quad (6.9)$$

In Eq. (6.7), C_{fac} [1/cm²-s] is the normalization factor

$$C_{fac} = \sqrt{\iint_0^{R_a, 2\pi} \psi_i^4(r, \varphi) \overline{g(r, \varphi, t)}^2 r dr d\varphi \iint_0^{R_a, 2\pi} \psi_k^4(r, \varphi) r dr d\varphi} \quad (6.10)$$

which can be approximated to [See Appendix A for details] to

$$C_{fac} = \frac{a_o v_g \overline{N(t)}}{(\pi R_a^2)^2 d} \quad (6.11)$$

Equation (6.7) thus incorporates the effect of mode competition through the terms containing C'_{ikg} . Transverse modes within a VCSEL compete for the available gain at every point inside the active region. Thus the overall gain of the i^{th} mode $G_i(t)$ depends on the extent of overlap of the i^{th} mode with every other mode along with the gain profile of the active region. This is done through the inclusion of the gain density $\overline{g(r, \varphi, t)}$ in the overlap integral, Eq. (6.8). Note that spatial hole-burning is included in Eq. (6.7) through the terms containing time-averaged mode power $\overline{P_k(t)}$. The spatial overlaps, $\{C_{ikg}\}_{i,k=1}^M$ depends on the average carrier population through the gain coefficient (Eq. 3).

Finally a set of M linear coupled equations involving only the $\delta P_i(\omega)$ are derived by Fourier transforming Eq. (6.5) and (6.7) and substituting to eliminate $\delta G_i(\omega)$

$$\mathcal{A}_i \delta P_i(\omega) + \sum_{k \neq i}^M \{\mathcal{M}_k C_{ikg}\} \delta P_k(\omega) = \mathcal{N}_i(F_n, F_{p,i}) \quad (6.12)$$

where

$$\mathcal{A}_i = \left[\frac{\rho_{ni}\rho_i}{P_i(t)} + a_o v_g A_i C_{fac} C_{iig} \right] \quad (6.13)$$

$$\mathcal{N}_i(F_n, F_{p,i}) = a_o v_g F_n(\omega) + \frac{\rho_{ni}}{P_i(t)} F_{p,i}(\omega) \quad (6.14)$$

$$\mathcal{M}_k = a_o v_g A_k C_{fac} \quad (6.15)$$

$$\rho_i = \left\{ j\omega + \frac{\beta_i d}{\tau_n P_i(t)} \iint_0^{R_a, 2\pi} \overline{N(r, \varphi, t)} r dr d\varphi \right\} \quad (6.16)$$

$$\rho_{ni} = \left\{ \left(j\omega + \frac{1}{\tau_n} \right) + \frac{1}{G_i(t)} \sum_{k=1}^M \{ a_o v_g C_{fac} C_{ijg} A_k \overline{P_k(t)} \} \right\} \quad (6.17)$$

Eq. (6.12) shows how the photon fluctuations are driven by the Langevin sources included in $\mathcal{N}_i(F_n, F_{p,i})$, where the \mathcal{N}_i [1/s²] represent the fluctuations in both the photon population and carrier density.

The coefficients $\{\mathcal{M}_k\}_{k \neq i}^M$ on the left side of Eq. (6.12) represent the effect of mode competition of the i^{th} mode with the k^{th} mode in the common VCSEL gain medium. Note that these terms include the normalized overlap integral C_{ikg} , indicating that the effect of mode competition depends on the extent of overlap of the spatial transverse mode profiles in the gain region as discussed previously. Thus, in the system of equations represented by Eq. (6.12), the mode competition terms with \mathcal{M}_k result in negative cross-correlations between VCSEL modes while the common carrier density Langevin noise terms F_n included in the \mathcal{N}_i terms result in positive cross-correlations. Thus, in the absence of $\{\mathcal{M}_k C_{ikg}\}_{k \neq i}^M$ and F_n terms in Eq. (6.12), the cross-correlations between VCSEL modes would be zero since $\{F_{p,i}\}_{i=1}^M$ are orthogonal noise sources as described in the Appendix A.

Lastly, $\mathcal{A}_i[1/s^2]$ represents the extent of autocorrelation in the i^{th} VCSEL mode arising due to the carrier density and photon fluctuations in that mode since the autocorrelations result directly from the spontaneous emission of the carrier density and photons in i^{th} mode, it follows that \mathcal{A}_i depends on the i^{th} mode power, Eq. (6.13). \mathcal{A}_i also accounts for the second-order effects such as the spatial hole burning (SHB) through ρ_{ni} , Eq. (6.17). Eqs. (6.12) can be solved using Cramer's rule which gives

$$\delta P_i(\omega) = \frac{\Delta_i(\omega)}{\Delta(\omega)} \quad (6.18)$$

where $\Delta(\omega)$ and $\Delta_i(\omega)$ are given by the determinants

$$\Delta(\omega) = \begin{vmatrix} \mathcal{A}_1 & \mathcal{M}_2 C_{12g} & \mathcal{M}_3 C_{13g} & \cdots & \mathcal{M}_M C_{1Mg} \\ \mathcal{M}_1 C_{21g} & \mathcal{A}_2 & \mathcal{M}_3 C_{23g} & \cdots & \mathcal{M}_M C_{2Mg} \\ \vdots & \vdots & \vdots & \ddots & \vdots \\ \mathcal{M}_1 C_{M1g} & \mathcal{M}_2 C_{M2g} & \mathcal{M}_3 C_{M3g} & \cdots & \mathcal{A}_M \end{vmatrix} \quad (6.19)$$

and

$$\Delta_i(\omega) = \begin{vmatrix} \mathcal{A}_1 & \mathcal{M}_2 C_{12g} & \cdots & \mathcal{N}_1 & \mathcal{M}_{i+1} C_{1(i+1)g} & \cdots & \mathcal{M}_M C_{1Mg} \\ \mathcal{M}_1 C_{21g} & \mathcal{A}_2 & \cdots & \mathcal{N}_2 & \mathcal{M}_{i+1} C_{2(i+1)g} & \cdots & \mathcal{M}_M C_{2Mg} \\ \vdots & \vdots & \ddots & \vdots & \vdots & \ddots & \vdots \\ \mathcal{M}_1 C_{M1g} & \mathcal{M}_2 C_{M2g} & \cdots & \mathcal{N}_M & \mathcal{M}_{i+1} C_{M(i+1)g} & \cdots & \mathcal{A}_M \end{vmatrix} \quad (6.20)$$

Now the covariance between modes i, j is given in the frequency domain by

$$\widetilde{cov}_{ij}(\omega) = \overline{\delta P_i(\omega) \delta P_j^*(\omega)} = \lim_{T \rightarrow \infty} \frac{1}{T} \delta P_i(\omega) \delta P_j^*(\omega) \quad (6.21)$$

Substituting $\delta P_i(\omega)$ and $\delta P_j(\omega)$ from Eq. (6.34), we have

$$\widetilde{cov}_{ij}(\omega) = \lim_{T \rightarrow \infty} \frac{1}{T} \frac{\Delta_i(\omega) \Delta_j^*(\omega)}{\Delta(\omega) \Delta^*(\omega)} = \frac{1}{|\Delta(\omega)|^2} \lim_{T \rightarrow \infty} \frac{1}{T} \{\Delta_i(\omega) \Delta_j^*(\omega)\}, \text{ for } i \neq j \quad (6.22)$$

For $i = j$, this becomes

$$\overline{var}_i(\omega) = \lim_{T \rightarrow \infty} \frac{1}{T} \frac{\Delta_i(\omega) \Delta_j^*(\omega)}{\Delta(\omega) \Delta^*(\omega)} = \lim_{T \rightarrow \infty} \left\{ \frac{1}{T} \frac{|\Delta_i(\omega)|^2}{|\Delta(\omega)|^2} \right\} \quad (6.23)$$

In evaluating Eq. (6.22) and (6.23), Eq. (6.19) and (6.20) were used along with the correlations between the Langevin noise sources corresponding to the photon and carrier fluctuations, given by Eq. (A.5) through (A.8) in Appendix A.

Eqs. (6.19) through (6.23) represent a comprehensive solution for modeling VCSEL noise, and can be used to derive the covariance (COV) matrix normalized to the composite power output of a VCSEL.

$$\overline{COV}\{a_i\} = \begin{bmatrix} \frac{\overline{var}_1(\omega)}{P_1(t) P_1(t)} & \frac{\overline{cov}_{12}(\omega)}{P_1(t) P_2(t)} & \dots & \frac{\overline{cov}_{1M}(\omega)}{P_1(t) P_M(t)} \\ \frac{\overline{cov}_{21}(\omega)}{P_2(t) P_1(t)} & \frac{\overline{var}_2(\omega)}{P_2(t) P_2(t)} & & \frac{\overline{cov}_{2M}(\omega)}{P_2(t) P_M(t)} \\ & \vdots & \ddots & \vdots \\ \frac{\overline{cov}_{M1}(\omega)}{P_M(t) P_1(t)} & \frac{\overline{cov}_{M2}(\omega)}{P_M(t) P_2(t)} & \dots & \frac{\overline{var}_M(\omega)}{P_M(t) P_M(t)} \end{bmatrix} \quad (6.24)$$

The COV matrix contains the correlation properties of mode fluctuations and hence represents the RIN and MPN characteristics of VCSEL transverse modes. When Eq. (6.22) and (6.23) are substituted in Eq. (6.24), the resultant COV matrix contains C_{ijg} terms which represent the extent of spatial overlap between the intensity profiles of i and j transverse modes along with the gain profile $g(r, \varphi, t)$.

6.4.1 Closed-Form Expressions for VCSEL Mode Correlations

Equations (6.22) through (6.24) together provide a comprehensive description of the VCSEL noise properties. However, the complexity makes them difficult to incorporate into an optical link model. Thus the COV matrix is simplified by making a

few assumptions while remaining consistent with the physics incorporated in the previous section.

The major contribution to the cross-correlations is likely through the direct interaction between any two modes through the common gain medium. Thus, the columns corresponding to the modes other than that of i and j in the determinants, Eq. (6.19) and (6.20) can be neglected. For a broad range of frequencies, it can be derived from Eq. (6.23) [Details in Appendix A],

$$\begin{aligned} \overline{var_i(\omega)} = & \left[\left\{ |\mathcal{A}_j|^2 - 2C_{ijg} \text{Re}(\mathcal{M}_j \mathcal{A}_j) \right\} (a_o v_g)^2 \frac{\overline{F_n(\omega) F_n^*(\omega)}}{\overline{P_i(t)} |\mathcal{A}_i \mathcal{A}_j|^2} + |X_i|^2 |\mathcal{A}_j|^2 \frac{\overline{F_{p,i}(\omega) F_{p,i}^*(\omega)}}{\overline{P_i(t)} |\mathcal{A}_i \mathcal{A}_j|^2} \right. \\ & \left. + \mathcal{M}_j^2 C_{ijg}^2 \frac{\overline{F_{p,j}(\omega) F_{p,j}^*(\omega)}}{\overline{P_i(t)} |\mathcal{A}_i \mathcal{A}_j|^2} \right] \overline{P_i(t)} \end{aligned} \quad (6.25)$$

Here, $X_i = \frac{\rho_{ni}}{\overline{P_i(t)}}$, Eq. (A.35) Appendix A. Each individual term in Eq. (6.25) represents the contribution of the carrier density fluctuations, photon fluctuations in i^{th} mode and photon fluctuations in j^{th} mode respectively. As can be intuitively understood, the impact of the j^{th} mode photon fluctuations on the variance of i^{th} mode is through mode competition effect incorporated in the C_{ijg} in the equation. In deriving Eq. (6.25), the contribution from the cross-fluctuations between the carrier and photon reservoirs of the Langevin sources, $\overline{F_n(\omega) F_{p,i}^*(\omega)}$ and $\overline{F_n(\omega) F_{p,j}^*(\omega)}$ has been neglected as they are small for the typical VCSEL parameters, Table 6.1.

It is useful to convert the photon numbers $\overline{P_i(t)}$ into normalized mode powers $\{\overline{\bar{a}_i}\}_{i=1}^M$ related to photon population as $\overline{P_i(t)} = \bar{a}_i \overline{P_T(t)}$. Rewriting Eq. (6.25) in terms of the normalized mode powers, we have

$$\overline{var_i(\omega)} = \overline{\alpha(\omega)}^2 \bar{a}_i \quad (6.26)$$

where $\overline{\alpha(\omega)}$ is the frequency domain proportionality constant, given by

$$\begin{aligned} \overline{\alpha(\omega)}^2 = & \left[\left\{ |\mathcal{A}_j|^2 - 2C_{ijg} \text{Re}(\mathcal{M}_j \mathcal{A}_j) \right\} (a_o v_g)^2 \frac{\overline{F_n(\omega) F_n^*(\omega)}}{\bar{a}_i |\mathcal{A}_i \mathcal{A}_j|^2} + |X_i|^2 |\mathcal{A}_j|^2 \frac{\overline{F_{p,l}(\omega) F_{p,l}^*(\omega)}}{\bar{a}_i |\mathcal{A}_i \mathcal{A}_j|^2} \right. \\ & \left. + \mathcal{M}_j^2 C_{ijg}^2 \frac{\overline{F_{p,j}(\omega) F_{p,j}^*(\omega)}}{\bar{a}_i |\mathcal{A}_i \mathcal{A}_j|^2} \right] \overline{P_T(t)} \end{aligned} \quad (6.27)$$

To get an intuitive understanding of the proportionality constant $\overline{\alpha(\omega)}$, let us consider the case where the rate of spontaneous emission for the carrier density is low compared to that for the photons. This results in the carrier density fluctuations being negligible, i.e., $\overline{F_n(\omega) F_n^*(\omega)} \approx 0$. In this case, the Eq. (6.27) reduces to

$$\overline{\alpha(\omega)}^2 = \frac{2R_{sp} \overline{P_T(t)}^2}{\left| j\omega + \frac{\beta_i dN_T(t)}{\tau_n \bar{a}_i P_T(t)} \right|^2} \quad (6.28)$$

Note here that the spontaneous emission factor $\bar{\beta}_i$ is proportional to the power in that mode and hence the ratio is independent of \bar{a}_i . The normalized RIN parameter in the i^{th} mode is defined using Eq. (6.26), (6.28) as

$$RIN_i(\omega) = \frac{\overline{var_i(\omega)}}{\bar{a}_i^2} = \frac{\overline{\alpha(\omega)}^2}{\bar{a}_i} \quad (6.29)$$

In the high frequency region, it is easy to see from Eq. (6.27) that the $var_i(\omega)$ falls off as square of the frequency ω , which is also true for the single mode lasers [39].

Table 6.1. Typical VCSEL parameters

<u>VCSEL Parameter</u>	<u>Symbol</u>	<u>Typical value</u>
Group velocity	v_g	$\frac{3}{4.2} \times 10^{10}$ cm/s
Material gain coefficient	a_o	1×10^{-16} cm ²
Spontaneous emission factor	β_i	$\sim 0.7 \times 10^{-5}$
Rate of spontaneous emission	R_{sp}	2×10^8 s ⁻¹
Rate of carrier recombination	γ_n	1×10^9 s ⁻¹
Carrier density at transparency	N_t	4×10^{19} cm ⁻³
Carrier lifetime	τ_n	1 ns
Longitudinal confinement factor	Γ_i	0.09
Thickness of the quantum well	d	30 nm
Radius of active region	R_a	4 μ m
Photon density at transparency	P_t	9×10^{15} cm ⁻³

The variance in the time-domain is obtained by inverse Fourier Transform of Eq. (6.29) yielding a frequency dependent variance. The traditional single RIN parameter is obtained by averaging over the measurement bandwidth as

$$\overline{RIN}_{i,avg} = \frac{1}{2\pi \Delta f} \int_0^{2\pi \Delta f} \overline{RIN}_i(\omega) d\omega = \frac{1}{2\pi \Delta f} \frac{\alpha^2}{\bar{a}_i} \quad (6.30)$$

where

$$\alpha^2 = \int_0^{2\pi \Delta f} \overline{\alpha(\omega)}^2 d\omega \quad (6.31)$$

The variance of the i^{th} mode in the time-domain can be derived for a measurement bandwidth of Δf as

$$var_i = 2\pi \Delta f R \widetilde{N}_{l,avg} \bar{a}_i^2 = \alpha^2 \bar{a}_i \quad (6.32)$$

It is easy to see that this result can be extended even when we take into account the effect of all the other modes in the VCSEL. In that case, we simply treat the j^{th} mode as a sum of the rest of the modes, i.e., $\bar{a}_j = 1 - \sum_{k \neq i}^M \bar{a}_k$. Eq. (6.30) shows that the average RIN parameter in the i^{th} mode is inversely proportional to the mode power, which is consistent with our understanding of the RIN spectrum for single mode lasers. Fig. 6.2 illustrates this dependence where the $R \widetilde{N}_{l,avg}$ is calculated from the $\widetilde{\alpha(\omega)}^2$ using Eq. (6.31) for the VCSEL parameters and a bandwidth of 25GHz. Both the frequency dependence and the corresponding single RIN parameter -130 to -140 dB/Hz of Fig. 6.2 are consistent with 25G capable VCSELs [48]

Following the same procedure [See Appendix A for full derivation], the covariance between modes i and j , $\widetilde{cov}_{ij}(\omega)$ can be derived for the generic case of unequal overlap of spatial profiles with the gain region in the VCSEL active region as

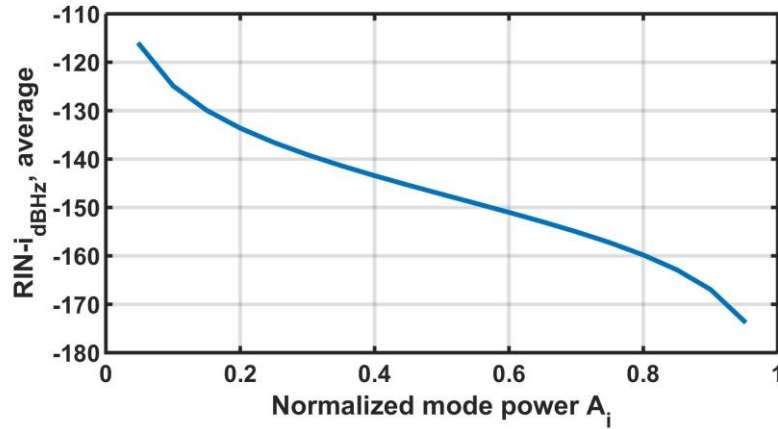


Fig. 6.2, Average RIN in a single VCSEL mode vs. normalized time-averaged mode power, Eq. (6.27), (6.30) for typical values of a VCSEL, Table 6.1.

$$\begin{aligned}
& \widetilde{\text{cov}}_{lj}(\omega) \\
&= \overline{P_i(t)} \overline{P_j(t)} \left[\frac{(a_o v_g)^2}{\mathcal{A}_i \mathcal{A}_j^* \overline{P_i(t)} \overline{P_j(t)}} \left(\frac{2R_{sp} \overline{P_T(t)} + \gamma_n \overline{N_T(t)}}{V_a^2} \right) \right. \\
&\quad - \frac{C_{ijg}}{|\mathcal{A}_i \mathcal{A}_j|^2 \overline{P_i(t)} \overline{P_j(t)}} \left\{ (\mathcal{M}_j \mathcal{A}_i^* \right. \\
&\quad + \mathcal{M}_j^* \mathcal{A}_j) (a_o v_g)^2 \left(\frac{2R_{sp} \overline{P_T(t)} + \gamma_n \overline{N_T(t)}}{V_a^2} \right) + \mathcal{M}_j \mathcal{A}_i^* |X_j|^2 2R_{sp} \overline{P_j(t)} \\
&\quad \left. \left. + \mathcal{M}_j^* \mathcal{A}_j |X_i|^2 2R_{sp} \overline{P_i(t)} \right\} \right] \\
\end{aligned} \tag{6.33}$$

Writing Eq. (6.33) in terms of the normalized mode powers $\{\bar{a}_i\}_{i=1}^M$, we have

$$\widetilde{\text{cov}}_{lj}(\omega) = \bar{a}_i \bar{a}_j [\Gamma_p(\omega)^2 - C_{ijg} \mathbf{k}_n(\omega)^2] \tag{6.34}$$

where $\Gamma_p(\omega)$ and $\mathbf{k}_n(\omega)$ are the frequency domain proportionality constants, given by

$$\Gamma_p(\omega)^2 = \frac{(a_o v_g)^2}{\mathcal{A}_i \mathcal{A}_j^* \bar{a}_i \bar{a}_j} \left(\frac{2R_{sp} \overline{P_T(t)} + \gamma_n \overline{N_T(t)}}{V_a^2} \right) \tag{6.35}$$

and

$$\begin{aligned}
\mathbf{k}_n(\omega)^2 &= \frac{1}{|\mathcal{A}_i \mathcal{A}_j|^2 \bar{a}_i \bar{a}_j} \left\{ (\mathcal{M}_j \mathcal{A}_i^* + \mathcal{M}_j^* \mathcal{A}_j) (a_o v_g)^2 \left(\frac{2R_{sp} \overline{P_T(t)} + \gamma_n \overline{N_T(t)}}{V_a^2} \right) \right. \\
&\quad \left. + \mathcal{M}_j \mathcal{A}_i^* |X_j|^2 2R_{sp} \bar{a}_j \overline{P_T(t)} + \mathcal{M}_j^* \mathcal{A}_j |X_i|^2 2R_{sp} \bar{a}_i \overline{P_T(t)} \right\} \\
\end{aligned} \tag{6.36}$$

The photon and carrier populations in $\Gamma_p(\omega)$, Eq. (6.35), correspond to the

variance in the carrier density Langevin noise F_n . Thus, as discussed in the previous section, the positive cross-correlations in the VCSEL mode power fluctuations mainly come from the carrier fluctuations that are common to all the modes. If the VCSEL active region is designed in such a way that these carrier fluctuations are reduced, the resultant VCSEL modes will exhibit only negative cross-correlations, through the mode competition terms in $\widetilde{\mathbf{k}}_n(\omega)$, Eq. (6.36). In this case, when the carrier density fluctuations are negligible, ie., $\overline{F_n(\omega)F_n^*(\omega)} \approx 0$, Eq. (6.35) and (6.36) reduce to

$$\widetilde{\Gamma}_p(\omega)^2 = 0 \quad (6.37)$$

and

$$\widetilde{\mathbf{k}}_n(\omega)^2 = \frac{2R_{sp}\overline{P_T(t)}^2 a_o v_g A_k C_{fac}}{\omega^4(\omega^2 + \frac{1}{\tau_n^2})} \left\{ \frac{\beta_i d \overline{N_T(t)}}{\tau_n^2 \bar{a}_i \overline{P_T(t)}} - \omega^2 \right\} \quad (6.38)$$

Note that these equations, Eq. (6.37), (6.38) are also applicable for the case of highly overlapping modes, where the $\widetilde{\mathbf{k}}_n(\omega)$ dominates over the $\widetilde{\Gamma}_p(\omega)$. Now in Eq. (6.36), each of the terms representing anti-correlations in the VCSEL modes contains \mathcal{M}_j which is the mode competition term as discussed in the last section. It can be deduced from Eq. (6.13) that the first term in \mathcal{A}_i dominates giving $|\mathcal{A}_i| \propto \frac{1}{\bar{a}_i}$. Using this proportionality, it is easy to see from Eq. (6.35) that $\widetilde{\Gamma}_p(\omega)$ is independent of the mode powers \bar{a}_i and \bar{a}_j . Similarly, noting that $|X_i| \propto \frac{1}{\bar{a}_i}$ It can be seen from Eq. (6.36) that the last two terms are independent of the mode powers, while the first term varies with it. However, the contribution of $(a_o v_g)^2$ term in $\widetilde{\mathbf{k}}_n(\omega)$ is typically low. Thus, we can treat

$\widetilde{\mathbf{k}_n(\omega)}$ to be independent of the mode powers.

Two important observations can be made from Eq. (6.34) through (6.36): The cross-correlation between modes i, j has both a positive as well as a negative component. Secondly, it is a strong function of the spatial overlap of the intensity profiles with the spatial gain profile, C_{ijg} and hence it is not a constant for a VCSEL. Previous formulations of VCSEL noise did not account for the impact of overlap integrals, in particular the non-uniform gain profile.

The normalized cross spectral density (CSD), $\widetilde{RIN}_{ij}(\omega)$ parameter is defined to represent the normalized correlations between modes i, j as

$$\widetilde{RIN}_{ij}(\omega) = \frac{\widetilde{\text{cov}}_{ij}(\omega)}{\bar{a}_i \bar{a}_j} = \widetilde{\Gamma}_p(\omega)^2 - C_{ijg} \widetilde{\mathbf{k}_n(\omega)}^2 \quad (6.39)$$

Just like the individual mode \widetilde{RIN}_i , the CSD $\widetilde{RIN}_{ij}(\omega)$ also falls off as square of the frequency ω . However, CSD $\widetilde{RIN}_{ij}(\omega)$ is independent of the mode powers \bar{a}_i and \bar{a}_j . Covariance in the time-domain can be derived by taking the Inverse Fourier Transform of Eq. (6.39) and integrating over the measurement bandwidth. Just like the RIN treatment in single-mode lasers, a constant \widetilde{RIN}_{ij} parameter shall be used that is averaged over the measurement bandwidth, calculated as

$$\widetilde{RIN}_{ij,avg} = \frac{1}{2\pi\Delta f} \int_0^{2\pi\Delta f} \widetilde{RIN}_{ij}(\omega) d\omega = \frac{1}{2\pi\Delta f} [\widetilde{\Gamma}_p^2 - C_{ijg} \widetilde{\mathbf{k}_n^2}] \quad (6.40)$$

Here, where $\widetilde{\Gamma}_p^2$ and $\widetilde{\mathbf{k}_n^2}$ are the integrals over the measurement bandwidth Δf of the respective frequency domain proportionalities, given by

$$\Gamma_p^2 = \int_0^{2\pi \Delta f} \Gamma_p(\omega)^2 d\omega \quad (6.41)$$

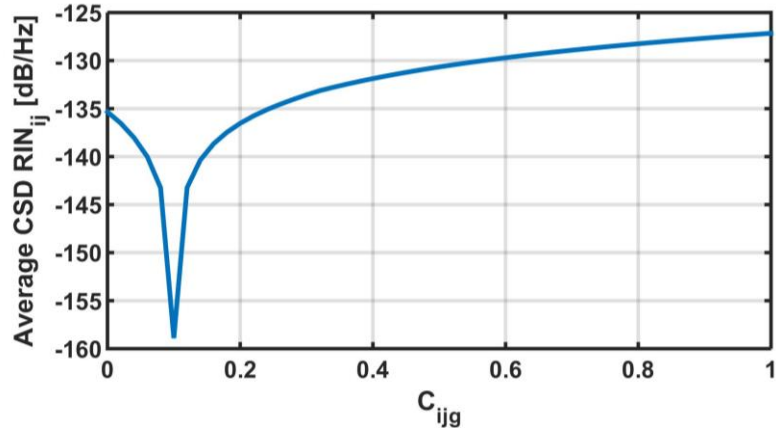


Fig. 6.3. Variation of the normalized average cross spectral density, $RIN_{ij,avg}$ calculated from Eq. (6.40) for a 2-mode VCSEL with mode powers $\bar{a}_i = 0.2$ and $\bar{a}_j = 0.8$ with normalized overlap integral C_{ijg} for typical values of a VCSEL, Table 6.1.

$$\mathbf{k}_n^2 = \int_0^{2\pi \Delta f} \mathbf{k}_n(\omega)^2 d\omega \quad (6.42)$$

The covariance between the modes i, j in the time-domain can be derived for a measurement bandwidth of Δf as

$$cov_{ij} = 2\pi \Delta f \widetilde{RIN}_{ij,avg} \bar{a}_i \bar{a}_j = [\Gamma_p^2 - C_{ijg} \mathbf{k}_n^2] \bar{a}_i \bar{a}_j \quad (6.43)$$

Figure 6.3 illustrates the dependence of the covariance on C_{ijg} quantitatively. The average CSD falls with C_{ijg} initially due to the increasing negative component in the cov_{ij} , Eq. (6.43).

The inflection point corresponds to the point when the negative part of the cov_{ij}

crosses the positive value, which increases in magnitude with further increase in C_{ijg} . For typical VCSEL values, it is seen that the covariance becomes negative for a C_{ijg} as low as ~ 0.1 . Thus, the VCSEL modes were mostly found to be anti-correlated to each other. A widely used metric of the extent of correlation typically used in statistics is the standard cross-correlation coefficient $R_{ij}(\tau = 0) = \frac{cov_{ij}(0)}{\sqrt{var_i(0)var_j(0)}}$. from Eq. (6.32), (6.43). R_{ij} ranges between -1 and 1, with perfect anti-correlations corresponding to -1 and perfect correlations corresponding to +1.

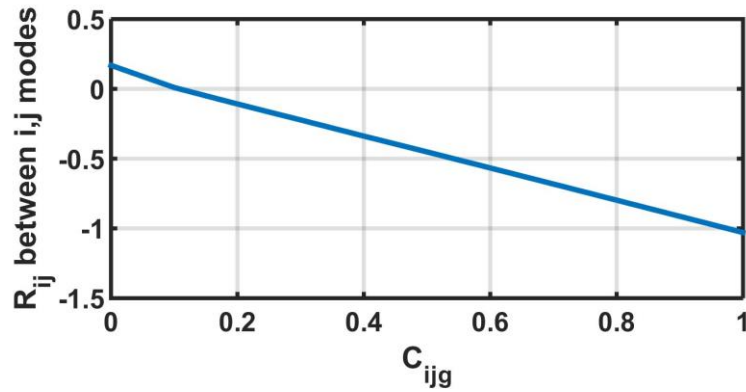


Fig. 6.4. Variation of the cross-correlation coefficient, $R_{ij}(0)$ calculated from Eq. (6.32) and (6.43) for a 2-mode VCSEL with mode powers $\bar{a}_i = 0.2$ and $\bar{a}_j = 0.8$ with normalized overlap integral C_{ijg} for typical values of a VCSEL, Table 6.1.

For typical VCSEL physical parameter values, the computed R_{ij} can vary anywhere between +0.1 to -1, Fig. 6.4, as the normalized overlap integral C_{ijg} , increases from 0 (low overlapping modes) to 1 (high overlapping modes). From Fig. 6.3 and Fig. 6.4, it is clear that the effect of C_{ijg} on the cross-correlations is significant and will impact the MPN noise penalty considerably. In addition, the overall RIN of the VCSEL will also have a notable impact due to the C_{ijg} .

Equations (6.32) and (6.43) together represent the noise properties of a VCSEL. Using the typical values for the VCSEL parameters, Table 6.1, the values of the model

parameters, Eq. (6.31), (6.41), (6.42), are calculated to be $\alpha = 0.01$, $\Gamma_p = 0.01$ and $k_n = 0.03$ respectively.

6.4.2 Analytic Model for the VCSEL Noise: Simplified Covariance Matrix

The dynamics of mode-fluctuations in a VCSEL lasing with ‘M’ transverse modes can be completely described by a covariance matrix (COV) of the normalized instantaneous mode powers $\{a_i\}_{i=1}^M$ having dimensionality (MxM):

$$COV\{a_i\} = \begin{bmatrix} var_1 & cov_{12} & \dots & cov_{1M} \\ cov_{21} & var_2 & \dots & cov_{2M} \\ & & \ddots & \\ cov_{M1} & cov_{M2} & \dots & var_M \end{bmatrix} \quad (6.44)$$

Here, $var_i = \overline{a_i^2} - \overline{a_i}^2$ is the variance of the fluctuation from mean value of the i^{th} VCSEL mode and $cov_{ij} = \overline{a_i a_j} - \overline{a_i} \overline{a_j}$ is the covariance of modes i and j . Note here that the notation $\{a_i\}_{i=1}^M$ is the same as that used in O-A model with the exception that the instantaneous sum of the mode powers is no longer assumed constant, i.e., $\sum_{i=1}^M a_i \neq 1$. The COV matrix completely captures the noise properties of a laser. The RIN which is the composite power fluctuations, defined by the standard $RIN_{\frac{dB}{Hz}}$ parameter is given by

$$\sigma_{RIN}^2 = \Delta f * 10^{\frac{RIN_{dB}}{Hz}} = var \left(\sum_{i=1}^M a_i \right) = \sum_{i=1}^M var_i + \sum \sum_{i \neq j}^M cov_{ij} \quad (6.45)$$

where Δf is the 3-dB bandwidth of the VCSEL. The cross-correlations in the fluctuations, given by the non-diagonal elements in the COV matrix define the extent of MPN.

The VCSEL-specific parameters introduced in this model can be related to the

standard RIN parameter by calculating the composite variance due to RIN by making use of the frequency domain form of the Eq. (6.45) to be

$$RIN_{comp}(\omega) = \alpha(\omega)^2 + (\Gamma_p(\omega))^2 - \mathbf{k}_n(\omega)^2 C_{ijg}) \sum \sum_{i \neq j}^M \bar{a}_i \bar{a}_j \quad (6.46)$$

The average value of the composite RIN, $RIN_{comp,avg}$ is then calculated as

$$\begin{aligned} RIN_{comp,avg} &= \frac{1}{2\pi \Delta f} \int_0^{2\pi \Delta f} RIN_{comp}(\omega) d\omega \\ &= \frac{1}{2\pi \Delta f} \left[\alpha^2 + (\Gamma_p^2 - C_{ijg} \mathbf{k}_n^2) \sum \sum_{i \neq j}^M \bar{a}_i \bar{a}_j \right] \end{aligned} \quad (6.47)$$

Here, α , Γ_p and \mathbf{k}_n are as defined before. While studying MPN, it is important to evaluate the effect of the relative time-delays between VCSEL modes after they undergo differential mode delays due to the fiber. Extending the correlations to include the relative time-delay τ between modes i , j , Eq. (6.32) and (6.43) can be re-written in terms of time delay τ as

$$var_i(\tau) = \alpha^2(\tau) \bar{a}_i \quad (6.48)$$

$$cov_{ij}(\tau) = \bar{a}_i \bar{a}_j (\Gamma_p^2(\tau) - \mathbf{k}_n^2(\tau) C_{ijg}) \quad (6.49)$$

Here, the time-domain proportionality constants $\alpha(\tau)$, $\Gamma_p(\tau)$, and $\mathbf{k}_n(\tau)$ are related to their frequency counterparts defined in Eq. (6.27), (6.35), (6.36) by

$$\alpha^2(\tau) = \int_0^{2\pi \Delta f} \alpha(\omega)^2 e^{i\omega\tau} d\omega \quad (6.50)$$

$$\Gamma_p^2(\tau) = \int_0^{2\pi \Delta f} \Gamma_p(\omega)^2 e^{i\omega\tau} d\omega$$

(6.51)

$$\mathbf{k}_n^2(\tau) = \int_0^{2\pi\Delta f} \overline{\mathbf{k}_n(\omega)}^2 e^{i\omega\tau} d\omega$$

(6.52)

Note that the model parameters α , Γ_p and \mathbf{k}_n are nothing but the time-domain versions of the proportionality constants given in Eq. (6.50) through (6.52) at $\tau = 0$, i.e., $\alpha = \alpha(\mathbf{0})$, $\Gamma_p = \Gamma_p(\mathbf{0})$ and $\mathbf{k}_n = \mathbf{k}_n(\mathbf{0})$. To understand the impact of the overlap integrals $\{C_{ijg}\}_{i \neq j}^M$ on the composite RIN of a VCSEL, the composite RIN for a 2-mode VCSEL was calculated with mode power distribution $\{\bar{a}_i\}_{i=1}^M = [0.2 \ 0.8]$.

Here the same typical values as before, Table 6.1, are used and they correspond to the model parameters of $\alpha = 0.01$, $\Gamma_p = 0.01$ and $\mathbf{k}_n = 0.03$ respectively. The RIN spectrum of this VCSEL with the same exact MPD for each individual mode is shown along with the composite RIN spectrum for two extreme cases- 1) Low overlap $C_{ijg} \approx 0$, red solid line; and 2) High overlap $C_{ijg} = 0.9$, black solid line, Fig. 6.5(a).

Each mode exhibits a resonant peak that is $< 10\text{GHz}$ and separated from each other by $\sim 4\text{GHz}$. The composite RIN (shown in Red for the low overlap case and Black for the high overlap case) will thus have multiple resonant peaks corresponding to each individual peak. In the case of a VCSEL with M number of modes, the composite RIN will exhibit M discrete peaks corresponding to each mode. The separation between the peaks will depend on the MPD of the VCSEL spectrum.

As predicted, the RIN spectrum is notably lower for the high overlap case compared to the low overlap case. For the physical parameters chosen in this example, since the $\bar{a}_1 < \bar{a}_2$, we see that $RIN_1 > RIN_2$ as expected. For the MPD $\{\bar{a}_i\}_{i=1}^M$ chosen

here, the composite RIN turns out to be lower than RIN_1 but higher than RIN_2 , for both the values of C_{ijg} . However, it should be noted that, for a specific MPD, for high \mathbf{k}_n and low Γ_p , the composite RIN can be smaller than the RIN in each of the individual modes.

It can be seen from Fig. 6.5(a) that the difference in the PSD of composite RIN between the cases of low C_{ijg} and high C_{ijg} is only prominent at low frequencies, upto

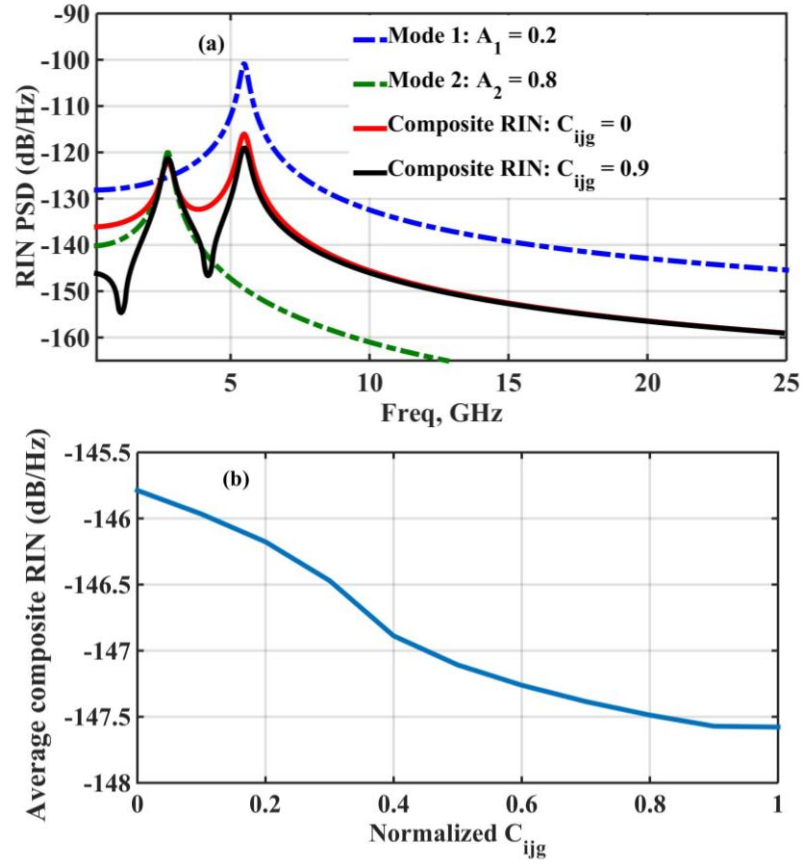


Fig. 6.5. Effect of C_{ijg} on the composite RIN for a 2-mode VCSEL with mode powers $\bar{\alpha}_i = 0.2$ and $\bar{\alpha}_j = 0.8$ and typical VCSEL parameters, Table 6.1. The corresponding model parameters are calculated to be $\alpha = 0.01$, $\Gamma_p = 0.01$ and $\mathbf{k}_n = 0.03$. (a) RIN spectrum for individual modes and composite RIN from Eq. (6.29), (6.46) for two extreme cases of C_{ijg} ; (b) Average composite RIN vs. C_{ijg} from Eq. (6.47)

~10GHz. At higher frequencies, the RIN drops drastically, so does the effect of C_{ijg} . However, this difference at low frequencies is sufficient to cause a significant impact on the average composite RIN, Fig. 6.5(b). For the normalized overlap C_{ijg} ranging from 0

to 1, the average composite RIN may vary from -145.5dB/Hz to -147.5dB/Hz, strictly decreasing with C_{ijg} . This difference of ~ 2 dB/Hz is significant particularly for the PAM-based high speed optical links using VCSELs with tight power budgets.

Thus, the COV matrix has been reduced to three VCSEL-specific parameters α , Γ_p , and k_n that represent the RIN and MPN in the VCSEL-based optical links. One important consequence of this model is that the cov_{ij} can be positive if the Γ_p term dominates in Eq (6.49) which can occur for low overlapping modes. Another important consequence is that the cross-correlations between different pair of VCSEL modes is different, in contrast to the assumption in IEEE model. The magnitude of these correlations depend directly on the extent of overlap of the spatial profiles in the gain region, $\{C_{ijg}\}_{i \neq j}^M$. Direct experimental measurements done on 900nm and 850nm VCSELs confirm these predictions, as will be shown in the subsequent sections. The normalized overlap integrals $\{C_{ijg}\}_{i \neq j}^M$ can either be directly measured or numerically calculated, provided we know the spatial intensity profiles of the VCSEL modes $\{\psi_i^2(r, \varphi)\}_{i=1}^M$ and the gain density profile in the active region $g(r, \varphi)$. One approach is to assume the VCSEL transverse mode profiles resemble Laguerre-Gaussian mode family as seen in a quadratic refractive index waveguide structure [67].

6.4.3 Special Cases: VCSEL With High and Low Overlapping Modes

As discussed in section 6.4.1, for a VCSEL in which the transverse spatial mode profiles have very high overlap i.e., $\{C_{ijg}\}_{i \neq j}^M \gg 0$, the negative part of the cross-covariance, $\widetilde{k_n(\omega)}$ term dominates over the $\widetilde{\Gamma_p(\omega)}$ term. It is apparent from Eq. (6.47) that this case corresponds to the RIN of a VCSEL being the lowest due to maximum anti-

correlations. Thus these cases are of practical interest that can be potentially exploited for reducing noise in the VCSEL-based links. In both the cases, Eq. (6.32) and (6.43) reduce to

$$var_i = \alpha^2 \bar{a}_i \quad (6.53)$$

$$cov_{ij} = -\mathbf{k}_n^2 C_{ijg} \bar{a}_i \bar{a}_j \quad (6.54)$$

where

$$\alpha^2 = 2R_{sp} \overline{P_T(t)^2} \int_0^{2\pi \Delta f} \frac{1}{\left| j\omega + \frac{\beta_i d\overline{N_T(t)}}{\tau_n \bar{a}_i \overline{P_T(t)}} \right|^2} d\omega \quad (6.55)$$

and

$$\mathbf{k}_n^2 = 2R_{sp} \overline{P_T(t)^2} a_o v_g A_k C_{fac} \int_0^{2\pi \Delta f} \frac{1}{\omega^4 \left(\omega^2 + \frac{1}{\tau_n^2} \right)} \left\{ \frac{\beta_i d\overline{N_T(t)}}{\tau_n^2 \bar{a}_i \overline{P_T(t)}} - \omega^2 \right\} d\omega \quad (6.56)$$

The corresponding time-domain versions are given by using Eq. (6.50) through (6.52). Thus, the MPN in this case can be represented by just two parameters α and \mathbf{k}_n , which can be derived through direct variance measurements of any single mode of the VCSEL with known RIN. α is extracted from the variance measurement in the individual VCSEL mode, Eq. (6.32). \mathbf{k}_n is then calculated from the relatively simple measurement of composite RIN by putting $\Gamma_p = 0$ and substituting the value of α in Eq. (6.47). This case is also applicable to a VCSEL in which rate of spontaneous emission of the carriers is much smaller than that of the photons in which case the carrier fluctuations become negligible.

Similarly, for the other extreme case of low overlapping modes, i.e., $\{C_{ijg}\}_{i \neq j}^M \ll 1$, it can be seen from Eq. (6.43) that Γ_p term dominates over the k_n making the covariance positive. This results in VCSELS with high RIN, Eq. (6.47).

6.5 Direct Experimental Validation of the New MPN Model

6.5.1 Experimental Methodology

COV matrix of 900nm VCSELS is extracted through direct real-time measurements of the correlation properties between various VCSEL modes. The 900nm

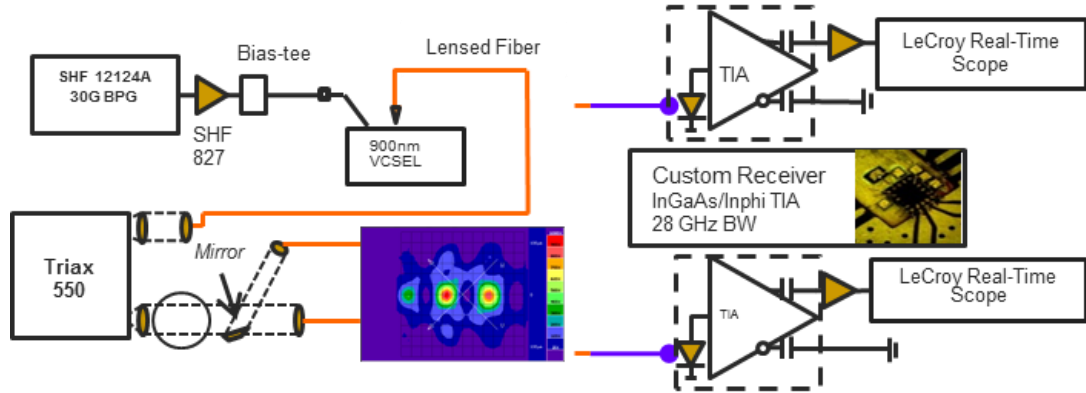


Fig. 6.6. (a) Mode splitting experimental setup with beam analysis (at circle); (b) Block diagram of the dual receiver setup.

VCSEL had a 17GHz bandwidth, $RIN < -147\text{dB/Hz}$ at the measurement bias of 8mA, and provide sufficient optical power for error free >25Gbps OOK transmission and error free >50Gbs PAM4 transmission with low MPN for OM4 links as long as 100m.

The 900nm VCSELS support 25Gbps with 3 primary modes. The VCSEL output was collected with a lensed multimode fiber, Fig. 6.6(a). The output of this fiber was imaged onto the entrance port of a Horiba Jobin Yvon Triax 550 imaging spectrometer with grating efficiency $\sim 69\%$ for TE and $\sim 62\%$ for TM polarization. The image plane of the exit port was focused onto two separate multimode fibers using a mirror to further

separate one of the modes. By carefully controlling the grating and mirror position, light was simultaneously collected from any two of the three dominant VCSEL modes.

The total efficiency of the mode separation process is at worst-case -4dB, allowing for sufficient power to detect the weakest of the three modes. Each collection fiber was connected to a 62.5 μ m lensed fiber and coupled into a separate receiver custom designed at Georgia Tech, Fig. 6.6(b). Each receiver output was amplified using a linear SHF 807 wideband amplifier and the resulting output was captured by a LeCroy 830Zi real-time Oscilloscope. Careful calibrations eliminated the impact of slight variations in the net gain of each signal path.

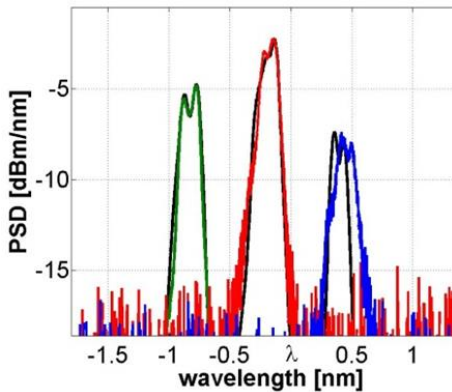


Fig. 6.7. Optical spectrum of VCSEL with overlaid captured modes

The lasing VCSEL modes are identified starting from the longest wavelength corresponding to the fundamental mode LP_{01} and going higher in the mode group numbers. For the 3rd mode, there are 2 degenerate LP modes (LP_{21} and LP_{02}). It is justified to assume that the mode seen here is LP_{21} as it will have higher probability to lase faster than the LP_{02} due to its low spatial overlap with the other modes.

6.5.2 Results and Discussions

For each correlation experiment the mode coupling in each arm was verified with an optical spectrum analyzer which performs two important checks; verifying that the

Triax and collection optics precisely retains the original mode spectral shape, Fig. 6.7, and verifying that the mode of interest is sufficiently isolated ($\geq 15\text{dB}$) from all other modes. 200k samples were recorded for each channel (receiver) for both 5 and 8mA DC bias without modulation and the average power was measured for each mode at the receiver.

The cross correlation coefficient of the noise was calculated using the standard equation:

$$R_{ij}(\tau) = \frac{\langle P_i(t)P_j(t + \tau) \rangle_t - \langle P_i(t) \rangle_t \langle P_j(t) \rangle_t}{\sigma_i \sigma_j} \quad (6.57)$$

where $P_i(t)$ represents the instantaneous power in the i^{th} mode, $P_j(t + \tau)$ is the time-delayed version of the instantaneous power in j^{th} mode, and σ_i, σ_j are the standard deviations in the i^{th} and j^{th} modes. The calculated R_{12} , R_{13} , and R_{23} for 8mA bias is depicted in Fig 6.8.

Figure 6.8 shows that for delay time τ greater than $\pm 500\text{ps}$ there is essentially no correlation. However, within 400-600ps there is clear and strong correlation. Specifically, R_{12} and R_{23} are anti-correlated, in contrast R_{13} shows a positive correlation.

The normalized COV matrix calculated from the direct measurements of the 900nm VCSEL here is:

$$\text{COV}\{a_i\} = 10^{-4} \begin{bmatrix} 1.36 & -0.87 & 0.46 \\ -0.87 & 4.68 & -1.3 \\ 0.46 & -1.3 & 3.4 \end{bmatrix} \quad (6.58)$$

Note that the thermal noise of the receivers is small and uncorrelated. The average VCSEL RIN $RIN_{dB} \frac{dB}{Hz}$ can be calculated from this measured COV matrix using Eq. (6.44) and is found to be consistent with the separately measured RIN of $< -147dB/Hz$ for this VCSEL and drive conditions [49].

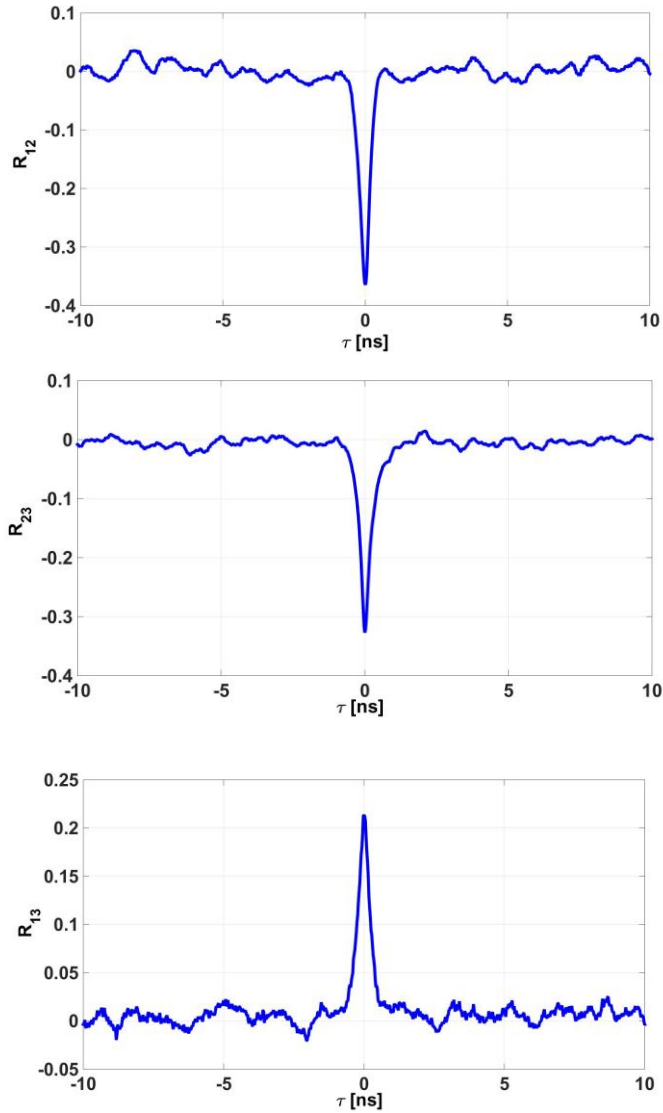


Fig. 6.8, Cross-correlation between modes at 8mA (a) R_{12} ; (b) R_{23} ; (c) R_{13} . Delay offset is due to different signal path lengths of the two receivers.

Measurements show that the degree of anti-correlation is not the same for the various mode pairs measured, which contradicts the standard O-A model assumptions,

i.e., γ_{cc} is not constant. A positive correlation between modes (1, 3) is also observed which is not explained by the standard model. Both these observations are explained by the new model as discussed in section 6.4.

From the measured variances, the unique VCSEL-specific parameter α is derived using Eq. (6.32). The derived α for the three different VCSEL modes is found to be constant, Table 6.2, which validates Eq. (6.32) for the measured 900nm VCSEL modes. One reason for the deviation in the extracted α of the third mode is the SHB effect which introduces second order power dependence of the variance.

Table 6.2, Calculated α for each mode from the direct measurements along with their corresponding time-averaged normalized mode powers.

Mode	$\langle a_i \rangle$	α
1	0.18	0.02
2	0.58	0.02
3	0.24	0.04

Now, to verify the measured non-diagonal elements of the COV matrix, normalized overlap integrals $\{C_{ijg}\}_{i \neq j}^M$ are needed, which require the knowledge of intensity spatial profiles $\{\psi_i^2(r, \varphi)\}_{i=1}^M$ and $g(r)$. $\{\psi_i^2(r, \varphi)\}_{i=1}^M$ can be calculated assuming the VCSEL transverse mode profiles resemble Laguerre-Gaussian mode family as seen in a quadratic refractive index waveguide structure [67]. Assuming constant gain density profile $g(r, \varphi)$, we numerically estimate $\{C_{ijg}\}_{i \neq j}^M$ of the first three L-P modes identified for the VCSEL spectrum under study to be $\{0.99; 1; 0.58\}$, Fig. 6.9. Using these overlap integrals and the $\{\bar{a}_i\}_{i=1}^M$ in Eq. (6.47), we get three linear equations in \mathbf{k}_n and $\mathbf{\Gamma}_p$ corresponding to each of the measured $\{cov_{ij}\}_{i \neq j}^M$. From a pair of any two

equations, \mathbf{k}_n and $\mathbf{\Gamma}_p$ can be extracted, Table 6.3. The extracted \mathbf{k}_n and $\mathbf{\Gamma}_p$ show a deviation of $\sim 7\%$ for $\mathbf{\Gamma}_p$ and $\sim 30\%$ for \mathbf{k}_n with the corresponding mean. One reason for this deviation is our assumption of constant gain profile while estimating $\{C_{ijg}\}_{i \neq j}^M$. In real VCSELs, these may vary slightly depending on the asymmetries in the device structure.

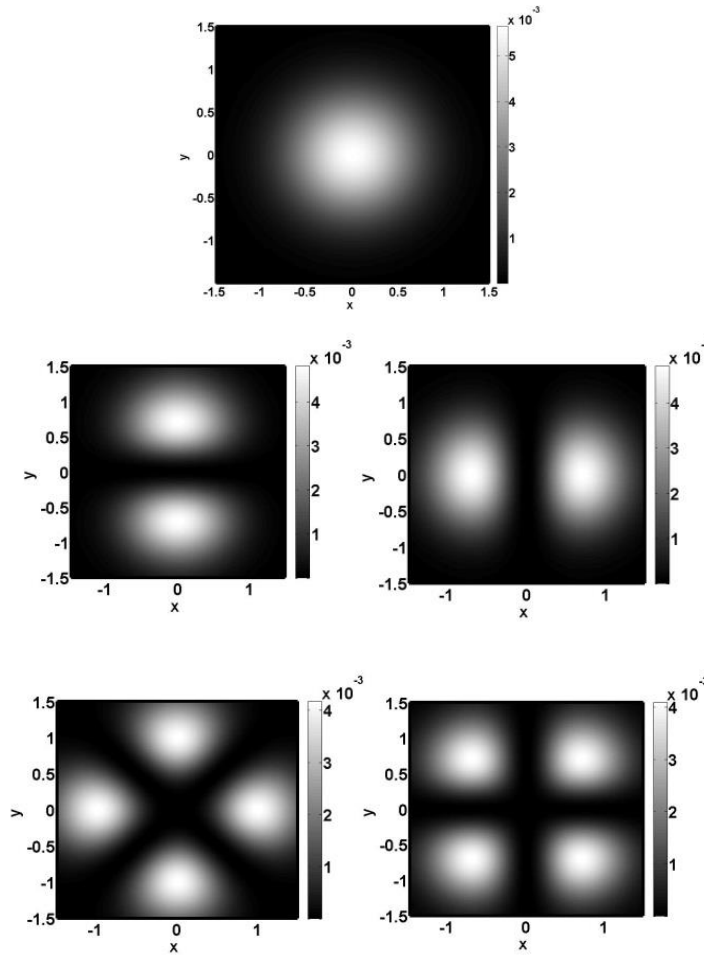


Fig. 6.9. Simulated intensity profiles of (a) LP01 mode; (b) LP11 mode; and (c) LP21 mode for the 900nm VCSEL under study. Normalized intensity overlap of mode profiles $\{I_{ij}\}_{i \neq j}$ are calculated from these simulated profiles.

Importantly, the results show that the modes 1 and 3 having the least overlapping integral and lower relative mode powers compared to the 2nd mode, show positive correlation, as predicted by the Eq. (6.47) in the new model. Also, the covariances

$\{cov_{ij}\}_{i \neq j}^M$ in general are different among the three modes, which is explained by the different overlap integrals, $\{C_{ijg}\}_{i \neq j}^M$.

6.6 Penalty Due to MPN and COV Matrix

Power penalty due to the VCSEL noise in optical links is given by a sum of the penalty due to RIN and the MPN. RIN penalty is calculated as the additional optical power required for maintaining the BER when RIN is added to the system, and is expressed in terms of the standard $RIN_{\frac{dB}{Hz}}$ parameter as [12]:

$$Pen_{RIN}(dB) = 5 \log\left(\frac{1}{1 - Q_{opt}^2 \sigma_{RIN}^2}\right) \quad (6.59)$$

Table 6.3, Extracted Γ_p and k_n for each mode pair from the direct measurements.

Extracted from	Γ_p	k_n
cov_{12} and cov_{23}	0.08	0.1
cov_{23} and cov_{13}	0.07	0.07
cov_{12} and cov_{13}	0.07	0.07

Here Q_{opt} is the standard optical Q factor of the VCSEL-based fiber link and σ_{RIN}^2 is given in Eq. (6.45). Similarly, MPN penalty is defined as the additional power required for maintaining the BER in order to compensate for the additional noise at the receiver due to the MPN. In the absence of ISI, it is calculated as [12]

$$Pen_{MPN}(dB) = 5 \log\left(\frac{1}{1 - Q_{opt}^2 \sigma_{MPN}^2}\right) \quad (6.60)$$

Here σ_{MPN} is the standard deviation corresponding to the additional noise that shows up at the receiver as a result of the correlated fluctuations of VCSEL modes

undergoing differential delays due to chromatic and modal dispersion of the fiber. It is given by, Appendix B,

$$\sigma_{\text{MPN}}^2 = \alpha^2(\Delta\tau_{ij}) \sum_{i=1}^M \{r_{ik}^2 - 1\} \bar{a}_i + \sum_{i \neq j} \{r_{ik}r_{jk} - 1\} \{\Gamma_p^2(\Delta\tau_{ij}) - \mathbf{k}_n^2(\Delta\tau_{ij})C_{ijg}\} \bar{a}_i \bar{a}_j \quad (6.61)$$

where r_{ik} or $r_i(t_k)$ is the i th mode received waveform sampled at k^{th} sampling instant.

Note that the covariance cov_{ij} , and thus the composite RIN depends on the relative delays between i and j , $\Delta\tau_{ij} = \tau_i - \tau_j$. However, the IEEE standard model for MPN neglects this dependence of the $\{cov_{ij}\}_{i \neq j}^M$ on $\Delta\tau_{ij}$ and calculates the MPN penalty assuming that the correlations are unaffected by the fiber induced delay. Recent experiments conducted on 850nm VCSELs show that the VCSEL correlations as measured on unmodulated VCSEL in fact depend on the fiber length. For comparison with the O-A model, let us assume that the dependence of $\{cov_{ij}\}_{i \neq j}^M$ on the time delays $\{\tau_{ij}\}$ can be neglected. Eq. (6.61) can then be re-written as

$$\sigma_{\text{MPN}}^2 = \alpha^2 \sum_{i=1}^M \{r_{ik}^2 - 1\} \bar{a}_i + \sum_{i \neq j} \{r_{ik}r_{jk} - 1\} \{\Gamma_p^2 - \mathbf{k}_n^2 C_{ijg}\} \bar{a}_i \bar{a}_j \quad (6.62)$$

To quantify the difference between the new model and the standard O-A model,

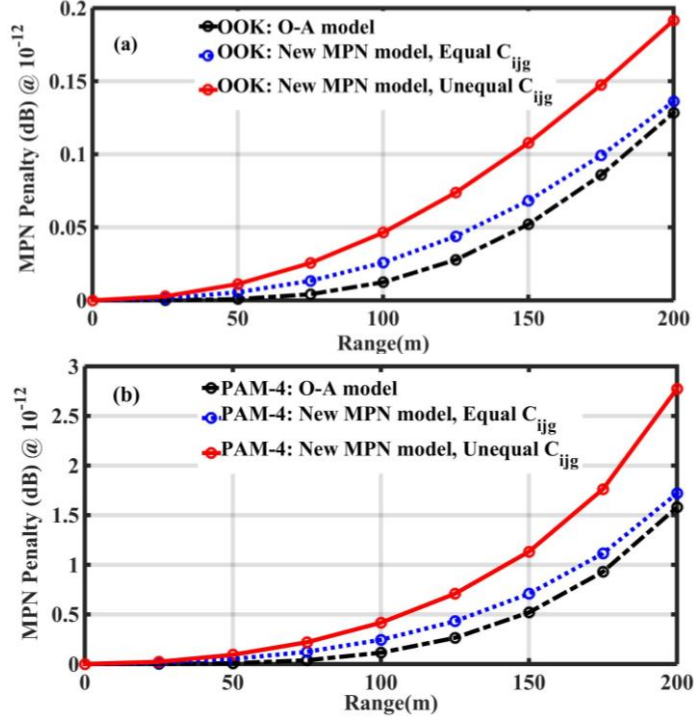


Fig. 6.10. Power penalty due to MPN vs. Reach for a 5 mode VCSEL-based optical link at 25GBaud with RIN of -145dB/Hz and normalized variance in the dominant mode of 2.7×10^{-3} : New model with $\alpha = 0.08$, $k_n = 0.09$ for the uniform $\{C_{ijg}\}_{i \neq j}^M$ and $k_n = 0.14$ for the non-uniform $\{C_{ijg}\}_{i \neq j}^M$ (Blue dot lines and Red solid lines) and IEEE standard O-A model with $k_{mpn} = 0.1$ (Black dash-dot lines) (a) For OOK modulation; (b) For PAM-4 modulation.

the estimated penalty due to MPN has been plotted as a function of the reach for an 850nm VCSEL-based SMF link with 25GBaud OOK modulation, using Eq. (6.60), for a 5 mode VCSEL with discrete Gaussian mode power distribution having RMS width 0.5nm. Fig 6.10(a). To provide a common basis for comparing the two models, it is assumed that the variance of the dominant mode is given to be 2.7×10^{-3} and the VCSEL RIN to be -145dB/Hz. For simplicity of analysis, Γ_p is assumed to be 0 in the new model and α , k_n are calculated using Eq. (6.32) and (6.47) to be 0.08 respectively. To illustrate the effect of the overlap integral on the MPN penalty, results from the new model for the two cases of uniform and non-uniform $\{C_{ijg}\}_{i \neq j}^M = \{0.99; 1; 0.58\}$ are shown. For the new

model, the MPN variance from Eq. (6.62) has been used. For both the models, a CD of $\sim 117\text{ps/nm.km}$ and receiver BW of 20GHz were used. The penalties are calculated for a target BER of 10^{-12} .

A penalty difference of $< 0.1\text{dB}$ is seen for a reach of 200m for the OOK links between the O-A model estimation and the new model estimation, Fig. 6.10(a). This indicates that the difference in estimated MPN penalty between the two models is not significant for OOK links. However, the error in the MPN penalty estimation by O-A model increases considerably with the extent of inequality among the mode overlap integrals $\{C_{ijg}\}_{i \neq j}^M$. The deviation is exacerbated considerably when we move to multi-level modulation schemes. Figure 6.10(b) shows a comparison of estimated MPN penalties for new model and the O-A model for 25GBaud PAM-4 case for a target BER of 10^{-12} . As seen from Fig. 6.10(b), the penalty estimated by O-A model is conservative by up to $>1\text{dB}$ for a reach of 200m , which increases for higher speeds. One important thing to notice from the Fig. 6.10(b) is that the new model result itself varies by $\sim 0.6\text{dB}$ between the cases of equal and unequal overlap integrals $\{C_{ijg}\}_{i \neq j}^M$. This indicates to the fact that most of the deviation in the penalty estimation is due to the implicit assumption in the O-A model that the overlap integrals are equal.

The COV matrix approach developed here can be readily included in modeling the penalty due to the modal noise (MN) in multi-mode laser based optical links, since they both are caused due to the same effect of correlated mode fluctuations inside the lasers. The only change in the model while adopting it for MN penalty would be in deriving Eq. (6.62) starting from the COV matrix. It will have an additional mode-selective attenuation term in it since the MN is caused due to the differential mode

attenuation (DMA).

6.7 Summary

A comprehensive model for estimating the MPN penalty has been developed starting from the Langevin noise driven spatio-temporal rate equations for VCSELs. The analysis has been carried out assuming an ideal noiseless injection current source and neglecting any reflections in the system. Thus, the noise is solely due to the spontaneous emission of the photon and carrier populations. The new model relaxes the simplifying assumptions of the O-A model which are inaccurate for the multi-transverse mode VCSEL-based optical links. The COV matrix formulation used in this model is very generic and can be used to represent the noise characteristics of any semiconductor laser. Using some reasonable approximations on the covariances that are derived from the noise rate equations, the COV matrix had been reduced to the three parameters α , Γ_p , and k_n that are unique to any VCSEL and completely capture its noise characteristics in an optical link. For highly overlapping modes, the positive component of the correlation, Γ_p becomes negligible, thus reducing the model to two parameters α and k_n which together characterize the RIN and MPN of the VCSEL-MMF links. Experimental measurements done on 900nm VCSELs validate the new model and demonstrate that positive correlations between VCSEL modes are possible when the spatial overlapping of the modes in the gain medium is low, as predicted by the new model. Power penalty due to MPN in VCSEL-based links was derived based on the new model, which is shown to deviate from the O-A model calculations significantly for 25GBaud PAM-4 links with typical parameters.

CHAPTER 7

EXPERIMENTAL STUDIES: PAM-4 LINKS BEYOND 50GBIT/S

With the recent efforts in the deployment of 400GbE short reach links by the IEEE 802.3 work group, focus on solutions for increasing throughput per lambda has increased significantly [31]. Advances in the VCSEL technology have made available VCSELs that support the deployment of high speed fiber-optic links up to 25Gbit/s using NRZ modulation [8]. However, future high speed short reach solutions require much higher data rates per lambda which will be difficult to achieve using NRZ-based systems even with the error correction techniques like FEC added. Although VCSELs have been reported with NRZ based 50Gbit/s links [7], the capability to robustly support 50Gbit/s and above is limited. Multilevel modulation schemes such as PAM-4 based links offer reliable solution to this challenge by doubling the throughput per lambda for the same bandwidth. In fact, recently IEEE 802.3bs adopted the PAM-4 modulation as a standard for short reach applications using single-mode fiber (SMF) [25]. With successful PAM-4 based VCEL-MMF link demonstrations reported recently, efforts to standardize the 50Gbit/s PAM-4 solutions even for the VCSEL-MMF based applications are underway. There have been a few high speed demonstrations using PAM-4 at 50Gbit/s and higher [8]-[10], [64], recently. In particular, reaches up to 50m at 50Gbit/s [10] and 200m at 30Gbit/s [9] have been shown to be possible at 850nm. However, none of them offer a comprehensive demonstration of the error-free performance over a wide range of fiber profiles. The nature of the MMF is such that slight variations of the fiber alpha profile can potentially result in significant penalties even for the same fiber modal dispersion

(MD) bandwidth, EMBc due to the complex interactions of the modal and chromatic dispersion (MCDI) which are not seen in the case of SMF-based links. Thus, for a reliable assessment of the deployable MMF-based links, comprehensive statistical analysis needs to be done across the whole span of standard OM4 and OM3 fibers with different fiber profiles and EMBc.

Major limitations in the VCSEL-MMF links include both chromatic dispersion (CD) and differential modal delay (DMD); however the new OM4 fibers exhibit very low DMD and the primary penalty is typically CD when using 25Gbit/s capable VCSELs. The dispersion profile of the silica based MMF indicates that the magnitude of dispersion reduces sharply as we move to longer wavelengths. To take advantage of this, longer wavelength solutions have been proposed using InGaAs/GaAs VCSELs near 1050nm. The active layers in the VCSEL are strained which contributes to larger differential gain and higher modulation bandwidth. Advances in this technology have enabled 1050nm operation with high reliability due in part to lower current densities [3].

In this chapter, comprehensive demonstration of error-free performance of VCSEL-MMF links > 50Gbit/s using PAM-4 modulation is presented at 850nm and 1050nm. Using a statistical study of MMFs that span the entire range of alpha profiles currently deployed, it will be shown that PAM-4 links can be successfully deployed to give error-free performance with the standard OM4 and OM3 fibers. Penalties for several fiber types whose EMBc values range from 2.05GHz.km at 850nm to 10GHz-km at 850nm will be quantified. A 4-tap pre-emphasis finite impulse response (FIR) filter is optimized for best BER performance in the electrical domain at the transmitter. Overhead for a small FEC is allocated for 50Gbit/s transmissions.

Through a comparison of the experimental results for (btb) with the IEEE 802.3bm conformed analytic model results, VCSEL RIN and bandwidth are extracted. Fiber penalties for different fiber profiles are extracted from a comparison of the experimental link results with those from the analytic model.

Additionally, it will be shown that longer wavelength VCSELs at 1050nm support >50Gbit/s PAM-4 signaling with exceedingly low RIN and negligible CD and mode partition noise (MPN) penalty for link lengths > 250m. Three different fiber categories are reported for 1050nm link analysis: OM3 class fibers with EMBc between 2.05GHz-km to 2.86GHz-km at 850nm; OM4 class fibers with EMBc between 5.2GHz-km to 10GHz-km at 850nm; and a prototype wideband fiber which is specially designed for operation at wavelengths from 850 to 1100 nm [3].

7.1 PAM-4 Experimental Setup

The electrical PAM-4 signal is generated by power-combining two independent pseudo random binary channels (PRBS), Fig. 7.1(a). Each channel provides a PRBS-7 stream, and has an independent 4-tap symbol spaced pre-emphasis filter. A linear low-noise amplifier is used to boost the resultant signal. The resultant electrical signal at test point 1 (TP1) exhibits a quality factor of ~ 9.5 when loaded with 50Ω impedance, Fig. 7.1(b). Light is coupled from the VCSEL using a conical lens optimized for 850nm light. The coupling is optimized for maximum coupling efficiency. A variable attenuator was placed in front the photo receiver to vary the amount of power received. The attenuator was calibrated for 1050nm light. The receiver is custom designed at Georgia Tech consisting of an InGaAs photodiode and a low noise Inphi TIA yielding a net bandwidth of $\sim 28\text{GHz}$. Two 22.5 GHz low pass filters are used in front of the error analyzer and

digital oscilloscope. The receiver is custom designed at Georgia Tech consisting of an InGaAs photodiode and a low noise Inphi TIA yielding a net bandwidth of ~28GHz.

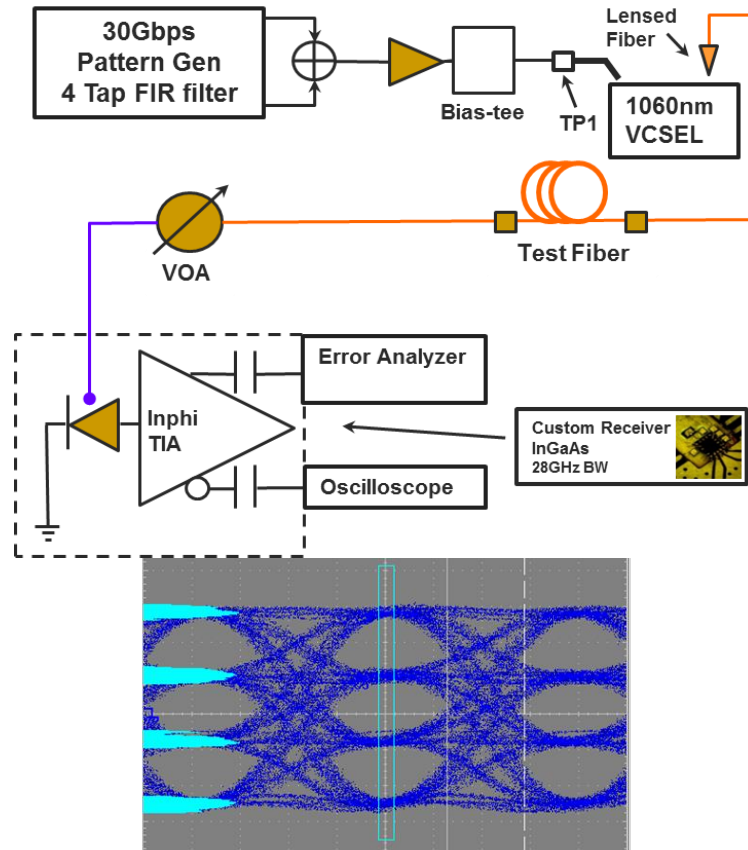


Fig. 7.1 (a) Link setup for PAM-4; (b) Eye diagram at TP1

7.1.1 VCSEL Characterization

The VCSEL has an active region of strained InGaAs/GaAs quantum wells (QW) with a 6 μm oxide aperture [3]. The VCSEL supports high modulation speeds > 25GHz with low power consumption and high reliability by making use of Al-free InGaAs/GaAs QWs and a double intra-cavity structure which eliminates current-flow in DBR layers. The L-I-V response of the VCSEL, Fig. 7.3, shows that output power > 3dBm can be achieved. The rise time of the VCSEL when modulated with a 1Gbit/s square wave was measured to be ~19ps corresponding to a 3dB bandwidth of ~18GHz.

The RMS spectral width of the VCSEL was measured to be $\sim 0.8\text{nm}$. Since the CD parameter of silica fiber at 1050nm is $< 40\text{ps/nm.km}$, this imposes a CD penalty of $< 0.5\text{dB}$ for a 25Gbaud , PAM-4 modulated 150m fiber link. The relative intensity noise (RIN) of the VCSEL is measured to be $< -150\text{dB/Hz}$. The optimum performance for PAM-4 modulation was obtained for a current bias of 6.1mA . The V-I data shows that the impedance of the VCSEL is $\sim 100\ \Omega$. This impedance mismatch results in electrical reflections at the transmitter which create an additional penalty in the link BER measurements.

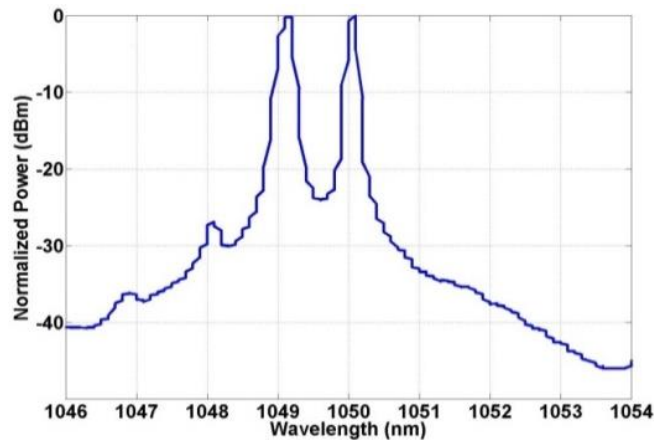


Fig. 7.2. VCSEL spectrum when biased at 25Gbit/s , 6.1mA

The same high-speed VCSEL was used for all the experiments reported. Figure 7.2 shows the spectrum of the VCSEL, when modulated at 26.26GBaud with a bias of 6.1mA . The measurement was taken with a 0.1nm resolution spectrum analyzer. The VCSEL spectrum is characterized by two main modes. The RMS spectral width is 0.72nm . Additional 1050nm VCSELs have similar spectral content.

Figure 7.3 shows the L-I-V curves for the VCSEL when modulated at 26.26Gbit/s . Optimum performance was obtained for a DC bias of 6.1mA , which is in the linear regime of the L-I curve. The L-I-V was measured by coupling light with a conical

lensed fiber optimized for 850 nm. The fiber was attached to a Germanium power sensor and the lens was optimized for maximum coupling efficiency.

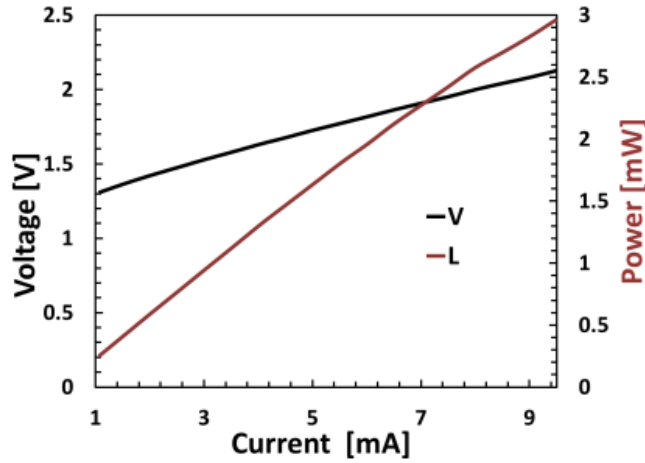


Fig. 7.3. L-I-V characteristics of the VCSEL.

7.1.2 PAM-4 BER Measurement

The bit error rate (BER) of the received PAM-4 signal is calculated using a conventional error analyzer (SHF 11100A). Three different threshold levels are used to measure the symbol error rates (SER) of the top, middle and the bottom eyes in the PAM-4 signal.

The BER can be calculated from the SER values, in high-SNR regime for the naturally coded PAM-4 signal [68]:

$$BER = \frac{1}{2}SER_{bot} + SER_{mid} + \frac{1}{2}SER_{top} \quad (7.1)$$

7.1.3 Forward Error Correction (FEC)

In this study, the overhead for a Reed-Solomon (RS) error correction has been included in the raw link speed. Several considerations are taken for choosing an appropriate FEC including: total latency, overclocking, and implementation penalty. It is

assumed that the RS (544, 514, 15, 10) FEC code will be implemented, which is in accordance with IEEE 802.3 standards for PAM-4 [25]. An over-clocking rate of 3 percent is included in all 50Gbit/s data. All equalization is feed-forward (FFE) and errors are assumed to be random, resulting in an effective coding gain of 6.5dB. No encoding or decoding results are presented.

7.1.4 Fiber Set Examined

As mentioned previously, MMFs that span across the entire range of modal bandwidths have been examined with 7 fiber alpha profiles and 4 different lengths, Table 7.1. For easy comparison between 850nm and 1050nm results, the results from each of the fibers here have been color-coded. The selected MMF set can be categorized broadly into three different types; 1) two standard OM3 fibers, with EMBC of 2.05GHz.km and 2.86GHz.km; 2) set of standard OM4 fibers with EMBC of 5.6GHz.km, 6GHz.km (two of these) and 10GHz.km; and 3) a prototype wideband fiber (WBF) specially designed for operation at wavelengths between 850nm and 1100nm. The selected fibers also have different MCDI behavior. For instance, the two OM4 fibers with the same EMBC ~5.6GHz.km have fiber alpha profiles such that the DMD slope in one of them acts to compensate the CD at 850nm (L-MMF) while in the other it acts to exacerbate it (R-MMF). Note that the chosen set of fibers thus covers the entire spectrum of behaviors of the commercial standard MMFs.

7.1.5 Electrical PAM-4 Implementation

Currently, conventional Non-return to zero (NRZ) or On-off keying (OOK) modulation could be accomplished with a simple setup. Without using a packaged

transmitter, the electrical setup involves a PRBS pattern generator, a bias-tee, possibly an amplifier, and a VCSEL probe. Advances in overall signal quality from pattern generators have resulted in signals with Q-Factors so high, that transmitter noise penalty is negligible. This, coupled with low sensitivities required for 25Gbaud NRZ, nullifies any transmitter noise that would be seen as a link penalty. However, PAM-4 requires a

Table 7.1: Complete set of MMF examined. EMBc spanning the entire range of current standard OM3 and OM4 fibers. Different lengths tested are not listed here.

MMF Type	Wavelengths Tested [nm]	EMBc [GHz.km]	DMD Slope (or) MCDI behavior
OM3	850, 1050	2.05	L-MMF
	850, 1050	2.86	L-MMF
OM4	850, 1050	5.6	L-MMF; R-MMF
	850, 1050	6	R-MMF
	850, 1050	10	R-MMF
WBF	1050	3.7	-

more complicated setup. This experiment combines two signals through an omnidirectional power divider to create the PAM-4 signal. In order to investigate link characteristics, the electrical setup is taken into consideration for PAM-4.

7.1.6 Extracting Fiber Penalties Using Analytic Model

The analytic model, as described earlier calculates the BER directly from the noise variances and the eye-closure penalty which is impacted by all possible ISI effects in the link. The noise variances are equivalent to those of the IEEE 802.3 link budget

model [2] while the ISI effects are determined assuming a Gaussian channel response to estimate the eye-closure penalty from the net channel response captured by the 10%-90% rise-time T_c . The worst-case eye-closure for each individual eye for PAM-4 is [68]:

$$E_{m,PAM-4} = 2.85 \exp\left(-1.28 \left(\frac{T}{T_c}\right)^2\right) \quad (7.2)$$

where ‘T’ is the symbol period. Through best fitting of the analytic model results with the back-to-back (btb) and fiber experimental data, power penalties due to individual ISI effects have been identified along with an accurate estimation of different noise parameters including RIN and MPN.

7.2 PAM-4 MMF Link Analysis: 850nm VCSELs

The BER performance for back-to-back (btb) with analytic results for NRZ and PAM-4 VCSEL-based links is shown in Fig. 7.4. The results reveal a total power penalty for the PAM-4 setup of ~8.6dB compared to NRZ. In this, the inherent penalty of going to a multi-level modulation, in this case 4 level, is about 4.8dB. The additional 3.8dB is

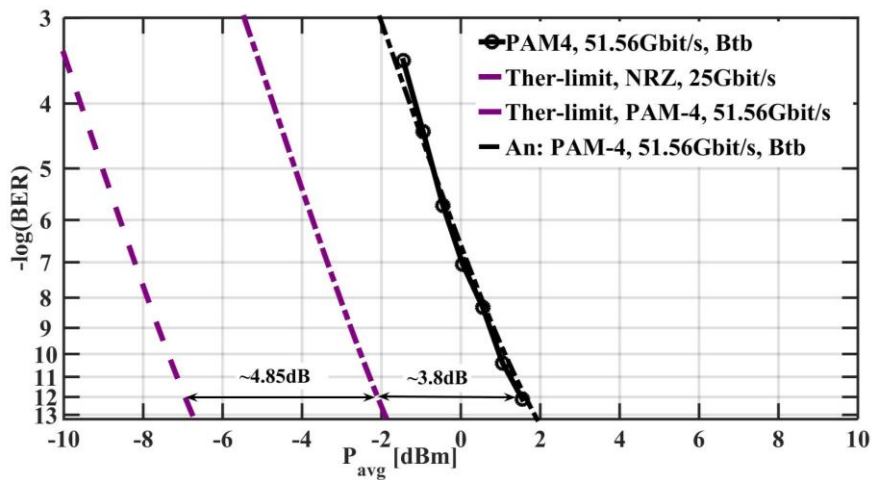


Fig. 7.4. 25.78GBaud at 850nm for Btb links using NRZ and PAM-4: Analytic (dash-dot and dash lines): RIN ~-147dB/Hz, and ISI penalty indicated. Experimental (solid lines)

from a combination of the VCSEL ISI and the non-ideal PAM-4 electrical setup that was used. Major component in this additional penalty is due to the nonlinear response of the VCSEL, evident from the nonlinear L-I-V curve, Fig. 7.3(a). VCSEL response to multiple levels at high modulation speeds can be nonlinear, resulting in an ISI penalty. In addition to this VCSEL-imposed penalty for PAM-4 modulation, the power combining way of generating the PAM-4 electrical signal reduces the quality of the PAM-4 eye resulting in penalty. This can be understood from an analysis of the electrical eye diagram of the PAM-4 signal that drives the VCSEL, Fig. 7.1(a). The noise also gets added up along with the signal power, degrading the SNR of each individual eye in the resultant PAM-4 signal by atleast a factor of 2. This can be readily overcome with custom PAM-4 drivers used close to the VCSELs. Best fitting of the analytic model results with the btb experimental data reveals a RIN of $\sim -154\text{dB/Hz}$. Error-free transmission ($\text{BER} \sim 10^{-12}$) for the entire set of OM3 and OM4 MMFs examined could be achieved, Fig. 7.5. The PAM-4 full ER (top/bottom) was maintained at $\sim 6\text{dB}$ with a baud rate of 25.78125GBaud allowing for FEC overhead. Results for the 100m fiber link with the same pre-emphasis as the btb case are also included for accurate estimation of CD/MD penalties from comparison with analytic model results. Two representative analytic fits are also included in the Fig. 7.5(a) and 5(b), each for the 100m OM3 with $\text{EMBc} \sim 2.05\text{GHz.km}$ and for the 100m OM4 with $\text{EMBc} \sim 10\text{GHz.km}$ respectively. As can be seen from the Fig. 7.5(b), error-free transmission for 100m OM4 with no MCDI effect is possible with a penalty of below 1dB, while a reach of 100m using OM3 is possible with an additional penalty of $\sim 2.5\text{dB}$, Fig. 7.5(a).

Note that OM3 fibers used here are both left-sloped, which means that the MCDI effects in the fiber result in a reduction of penalty due to dispersion, compared to a neutral OM3 of the same bandwidth with no MCDI effects. Comparison of the analytic best fit results to the experimental fiber data estimates the net effective bandwidth to be $\sim 2.3\text{GHz-km}$ and 3.2GHz-km respectively for the left-sloped OM3 fibers having EMBC of 2.05GHz-km and 2.86GHz-km . This is consistent with our understanding of the MCDI effects in L-MMF that they act to compensate the dispersion penalty partly, thus increasing the net effective bandwidth.

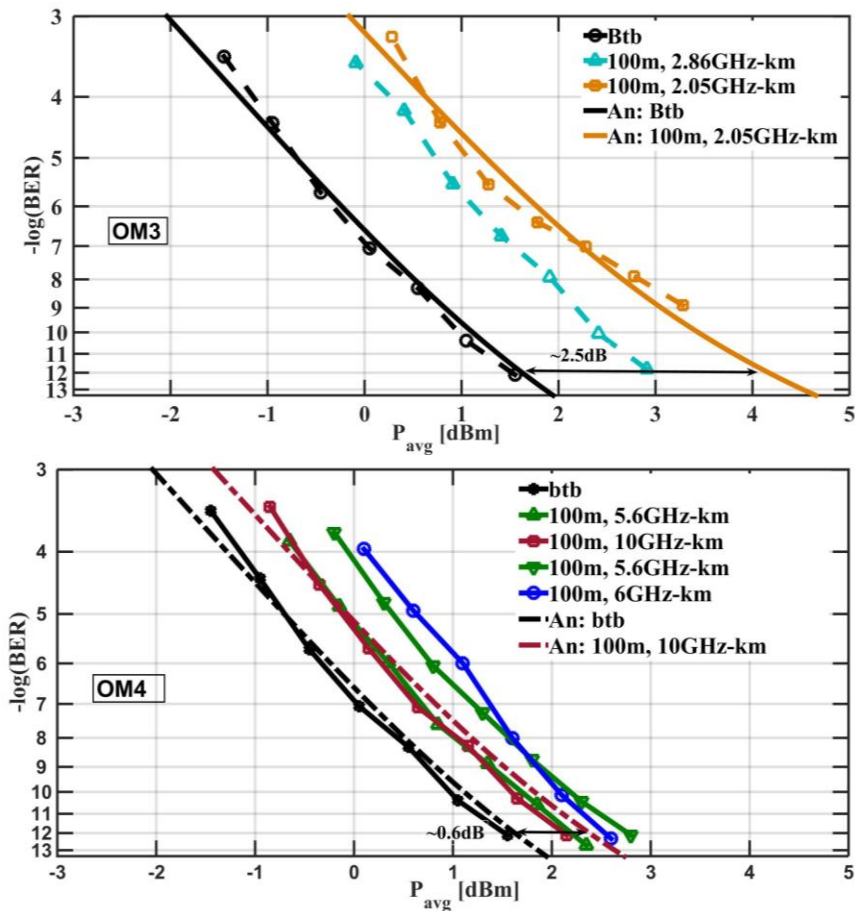


Fig. 7.5. 25.78GBaud using PAM-4 at 850nm: (a) OM3 MMF performance; (b) OM4 MMF performance; Analytic (dash-dot lines) and Experimental data (solid lines).

7.3 Moving to Longer Wavelengths: >50Gbit/s PAM-4 at 1050nm

The power penalty in PAM-4 links mainly comes from a combination of chromatic dispersion, modal dispersion and the VCSEL noise. As mentioned previously, the RIN of the VCSELs was estimated using the analytic model to be $\sim -147\text{dB/Hz}$ which is quite low. Also, however the new OM4 fibers exhibit very low DMD and the primary penalty is typically CD when using 25Gbaud VCSELs. Thus longer wavelength solutions have been proposed using InGaAs/GaAs VCSELs near $1\mu\text{m}$. From the frequency profile of the dispersion properties of silica, it is obvious that the CD penalty will improve by ~ 0.5 to 1dB at $1\mu\text{m}$ compared to 850nm . The active layers in the VCSEL are strained which contributes to larger differential gain and higher modulation bandwidth. With the VCSEL technology making advances in producing high-speed capable VCSELs around $1\mu\text{m}$, it is interesting to investigate the performance improvement that can be achieved moving to longer wavelengths. One challenge in this direction is that all the current MMFs are designed to give optimum performance around 850nm and their bandwidths are not wide enough to support wavelengths of $1\mu\text{m}$.

Consequently, there are prototype wideband fibers that were designed specially to have good EMBc properties for a wide range of wavelengths between 800nm to 1050nm . Such test fibers were used in this work to analyze the performance of PAM-4 links with $>50\text{Gbit/s}$ data rates at longer wavelengths. The BER performance of the btb PAM-4 and NRZ links at 1050nm and the corresponding analytic fits are shown in Fig. 7.6(a). Note that the btb ISI penalty in the PAM-4 compared to NRZ is reduced marginally from 3.8dB for 850nm case to 3dB for 1050nm case. This is attributed to the improvements in both the VCSEL linearity properties and reflections in the btb setup at the transmitter.

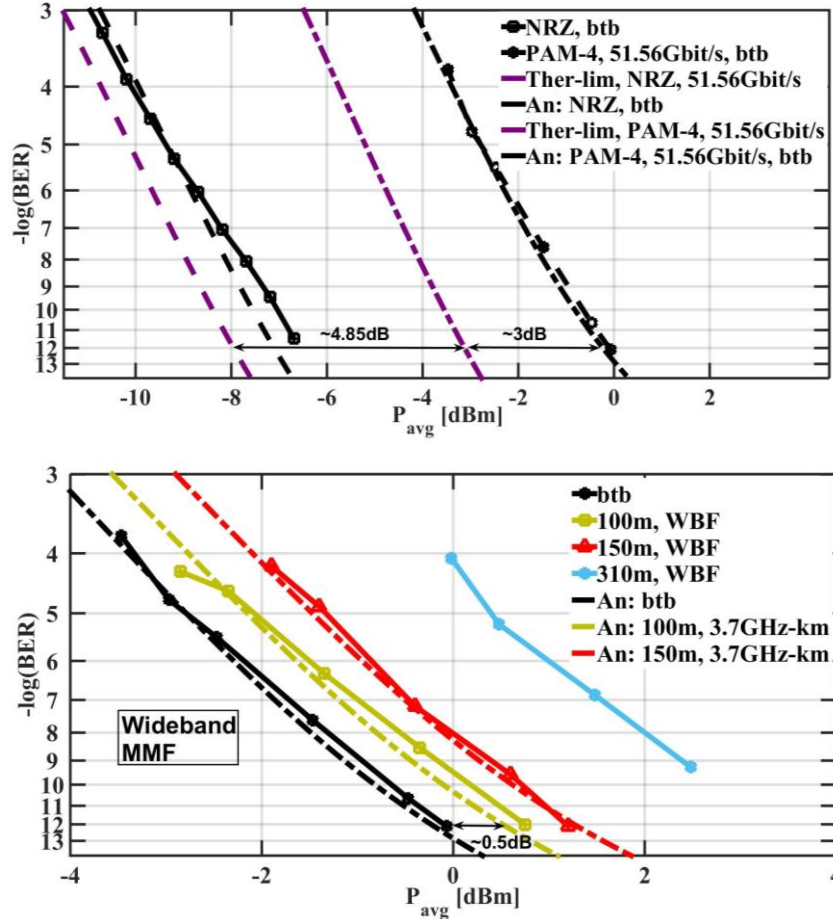


Fig. 7.6: 25.78GBaud at 1050nm: (a) Btb links using NRZ and PAM-4; (b) Wideband fiber (WBF) performance: Analytic (dash-dot lines) and Experimental data (solid lines).

Also, note that the responsivity of the photodiode at 1050nm increases from 0.3A/W to 0.38A/W and hence the thermal limit for the 1050nm shifts accordingly to the left compared to 850nm. Fig. 7.6(b) shows the performance of a prototype WBF designed for performance beyond the typical $\sim 850\text{nm}$. DMD measurements with a tunable laser show that modal bandwidth increases from $\sim 1.8\text{ GHz-km}$ at 775nm to as high as $\sim 4.2\text{ GHz-km}$ at 1000nm for these fibers.

The 310m fiber data shows that a BER of $< 10^{-5}$ can be achieved, which is limited only by the overall power available. Specifically, there is no evidence of a noise floor in

these measurements, which suggests negligible MPN penalty in these links. The peak bandwidth beyond 1000nm has not yet been determined. The experimental data shows

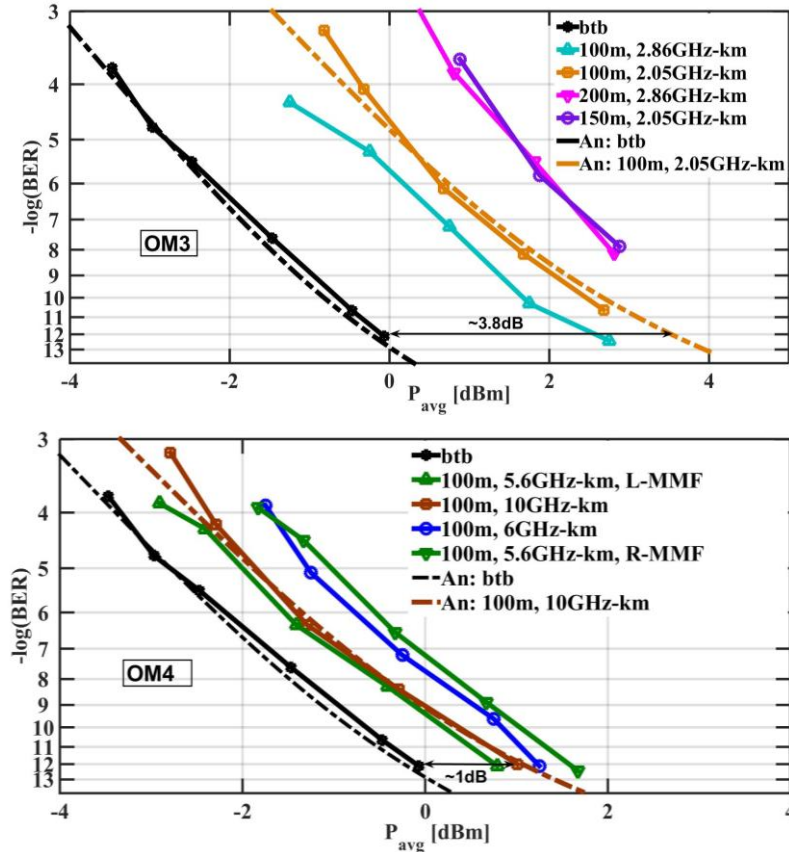


Fig. 7.7: 25.78GBaud using PAM-4 at 1050nm: (a) OM3 MMF performance; (b) OM4 MMF performance: Analytic (dash-dot lines) and Experimental data (solid lines).

that error-free performance is possible for reach up to 150m fiber without FEC and 310m with FEC at an additional fiber penalty of ~ 3 dB. Using the best-fitting of the analytic model results, the bandwidth of the WBF at 1050nm is estimated to be ~ 3.7 GHz-km.

The BER performance for btb, 100m and 200m of OM3 fiber, using pre-emphasis optimized for each link, is shown in Fig. 7.7(a). Results for the 100m fiber link with the same pre-emphasis as the btb case are also included for accurate estimation of CD/MD penalties from comparison with analytic model results. The PAM-4 full ER (top/bottom) was maintained at ~ 6 dB with a data rate of 51.56Gbit/s allowing for FEC overhead. This

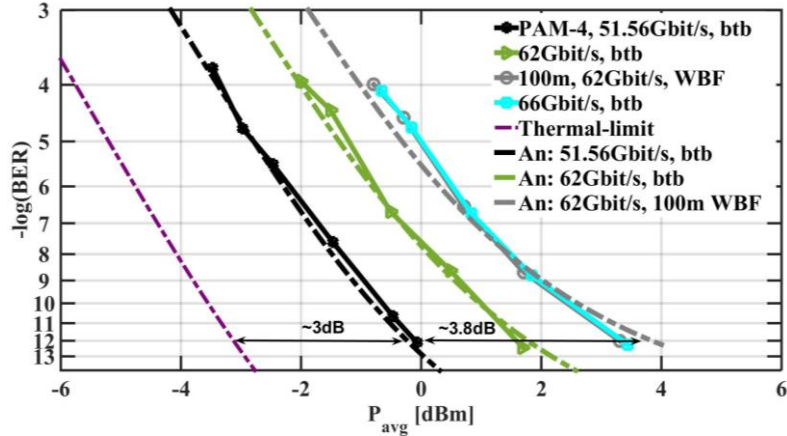


Fig. 7.8: Bit rates up to 66Gbit/s at 1050nm using PAM-4. Error-free transmission at 62Gbit/s with 100m WBF.

OM3 sample has its peak modal bandwidth between 900 and 950nm. The performance with 100m OM3 exhibits a 3.8dB fiber penalty for the worst OM3 when the same pre-emphasis as btb was used. Estimations deduced from fitting our analytic model results to the experimental data for 100m fiber link yield $\sim 2.4\text{GHz}\cdot\text{km}$ for the EMBc of the OM3 fiber at 1050nm. Here, a CD parameter of $\sim 40\text{ps}/\text{nm}\cdot\text{km}$ has been used in the analytic model which is typical of 50 micron MMFs at 1050 nm. The corresponding ISI penalties due to CD and MD for this 100m fiber link are $\sim 0.2\text{dB}$ and 1.5dB respectively.

For the OM4 fiber case, error-free transmission at 51.56Gbit/s at a BER of $\sim 10^{-12}$ was achieved with a fiber penalty of $\sim 1\text{dB}$ for the best OM4 and 1.5dB for the worst OM4 fiber examined, Fig. 7.7(b). The pre-emphasis has been optimized for the btb link for all the fibers. Analytic best fits reveal negligible MPN and an effective bandwidth of $\sim 4.2\text{GHz}\cdot\text{km}$ for the worst OM4 (R-MMF with EMBc $\sim 5.6\text{GHz}\cdot\text{km}$).

With successful link demonstrations at 51.56Gbit/s with all the OM3, OM4 and WBF MMFs, data rates of up to 66Gbit/s were also tested, Fig. 7.8. Error-free transmission of 100m WBF at 62Gbit/s was observed at a fiber penalty of 3.8dB. Analytic fit to this data suggests negligible MPN and fiber bandwidth at 1050nm of

3.7GHz-km, consistent with the estimation at 51.56Gbit/s for the WBF. Additionally, error-free demonstration at 66Gbit/s was observed for a btb penalty of ~3.8dB.

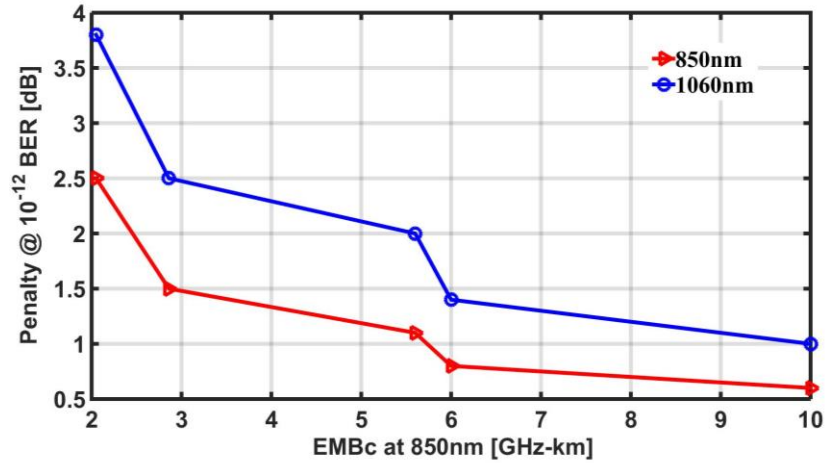


Fig. 7.9: Performance comparison of 850nm and 1050nm PAM-4 links at 25.78GBaud: Fiber penalty at BER $\sim 10^{-12}$ for 100m MMF with EMBc spanning the entire range of current standard OM3 and OM4 fibers.

7.4 Performance Comparison of 1050nm and 850nm PAM-4 Links

Although there is a significant improvement in the penalty due to the CD at longer wavelengths, the realization of such links would require that the currently deployed standard OM3 and OM4 fibers that are designed to have optimal bandwidth at 850nm should be able to support longer wavelengths. Specially designed fibers for longer wavelengths, such as the WBF used in these experiments represents future solution for exploiting the advantage we get in lowered CD penalty at 1050nm. But a smooth migration to future idealistic systems requires acceptable performance even with the standard OM3 and OM4 fibers that are optimized for 850nm links. Thus, the behavior of 1050nm links has been compared with that at 850nm for various OM3 and OM4 fibers at 100m reach, Fig. 7.9. Power penalty with respect to the corresponding btb cases at a BER

of 10^{-12} shows qualitatively the same behavior of both the 850nm and 1050nm links, with significant improvement in performance as the EMBc increases.

Table 7.2: Fiber penalty at BER $\sim 10^{-12}$ in 51.56Gbit/s VCSEL-MMF links for the set of MMF examined. EMBc spanning the entire range of current standard OM3 and OM4 fibers. The fiber penalties have been estimated by best analytic fits to the experimental data.

MMF Type	EMBc [GHz.km]	Length [m]	Fiber penalty @ 850nm [dB]	Fiber penalty @ 1050nm [dB]
OM3	2.05; (L-MMF)	100	2.5	3.8
		150	-	4.2
	2.86; (L-MMF)	100	1.5	2.5
		200	-	4.2
OM4	5.6; (L-MMF)	100	0.7	0.8
	5.6; (R-MMF)	100	1.1	2
	6; (R-MMF)	100	0.8	1.4
	10; (R-MMF)	100	0.7	1
WBF	3.7@1050nm	100	-	0.5
		150	-	1.2
		300	-	3.8

For 850nm links, the fiber penalty drops from 2.5dB for 100m OM3 having EMBc ~ 2.05 GHz.km to 0.6dB for 100m OM4 MMF having EMBc ~ 10 GHz.km. For 1050nm case, the respective fiber penalties are from 3.8dB to 1dB. This shows that the bandwidth degradation of the OM3 and OM4 fibers at 1050nm more than offsets the CD

penalty gain we achieved through reduced dispersion compared to 850nm, by imposing an average additional penalty of about ~1dB for 100m standard OM3 and OM4 links. However, a comparison of all the fiber penalties tested in these experiments estimated through best fitting of the analytic model to the experimental results, Table 7.2, reveals that the 1050nm link using 100m WBF shows the best performance among all the links examined. This proves beyond doubt that the longer wavelength systems, when used with the specially designed fibers having good bandwidth characteristics around 1 μ m, would outperform the current 850nm links especially when PAM-4 modulation is used.

7.5 RIN Dependence on Bias for 50Gbit/s PAM-4 Links; L-I-RIN Curves

RIN is primarily the result of spontaneous emission [67] and therefore generally decreases with increasing average laser power. Hence, the RIN penalty for a modulated VCSEL depends on the individual intensities of each possible amplitude. For NRZ links, a single RIN corresponding to the average output power may be a reasonable approximation as there are only two output power levels and the ER may be modest. The four distinct levels of PAM-4 together with the typical high ER associated however may result in significant variation of RIN with the power levels. Additionally, the reduced ER of the individual levels increases the BER sensitivity to RIN compared to NRZ links and a small error in RIN estimation causes larger deviations in the predicted link performance even at reasonably high ER. The effect increases with increasing VCSEL RIN, and is significant for RIN $>$ -150dB/Hz.

7.5.1 Dependence of VCSEL RIN Spectrum on Current Bias: L-I-RIN

The power spectral density (PSD) of the VCSEL RIN is measured when operating the VCSEL unmodulated at different DC-bias currents. The resultant spectra, Fig. 7.10(a), exhibit the expected peak resonance frequency shifts towards higher frequencies and increased damping with increasing bias. The average RIN at each bias is computed resulting in the L-I-RIN plots, Fig. 7.10(b). These 900nm VCSELs exhibit a very good average RIN less than -150dB/Hz for bias larger than 5mA.

7.5.2 Impact of L-I-RIN on 50Gbit/s PAM-4 Link Modeling

Error-free performance of 25.78GBaud PAM-4 using 900nm VCSELs at a full

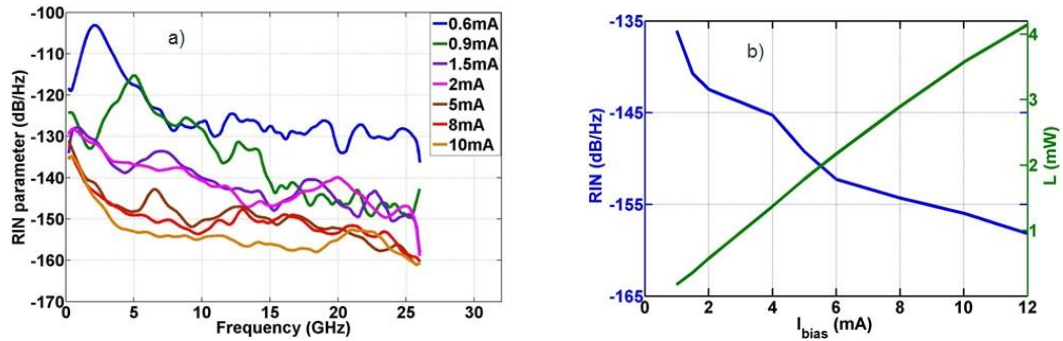


Fig. 7.10: (a) Unmodulated RIN spectra for various bias currents; (b) L-I-RIN for the 900nm VCSEL

(highest to lowest level) ER of ~ 5.4 dB, is readily achievable, Fig. 7.11a, in the back to back (btb) configuration. The measured data is fitted using both a fixed average RIN of -153.8dB/Hz corresponding to the average bias point (7.5mA) and an intensity dependent RIN of [-143.4, -150, -153.6 and < -155] dB/Hz for the 0, 1, 2 and 3 levels respectively.

The receiver sensitivity is fixed; therefore the only fitting parameter is the net ISI penalty. The variable RIN model yields notably better fits to the measured data than the fixed RIN model, Fig. 7.11a. Importantly, the ISI primarily determines the behavior at high BER and a combination of ISI and RIN determines the behavior at low BER. The extracted ISI is ~ 5.3 dB (5.5dB) for the variable RIN and fixed RIN model respectively.

Importantly, the apparent ISI penalty decreases by $\sim 0.2\text{dB}$ when using a variable RIN; thus the fixed RIN modeling overestimates the fiber ISI penalty. Furthermore, these deviations in the RIN penalty will be much larger for VCSELs with higher RIN. For

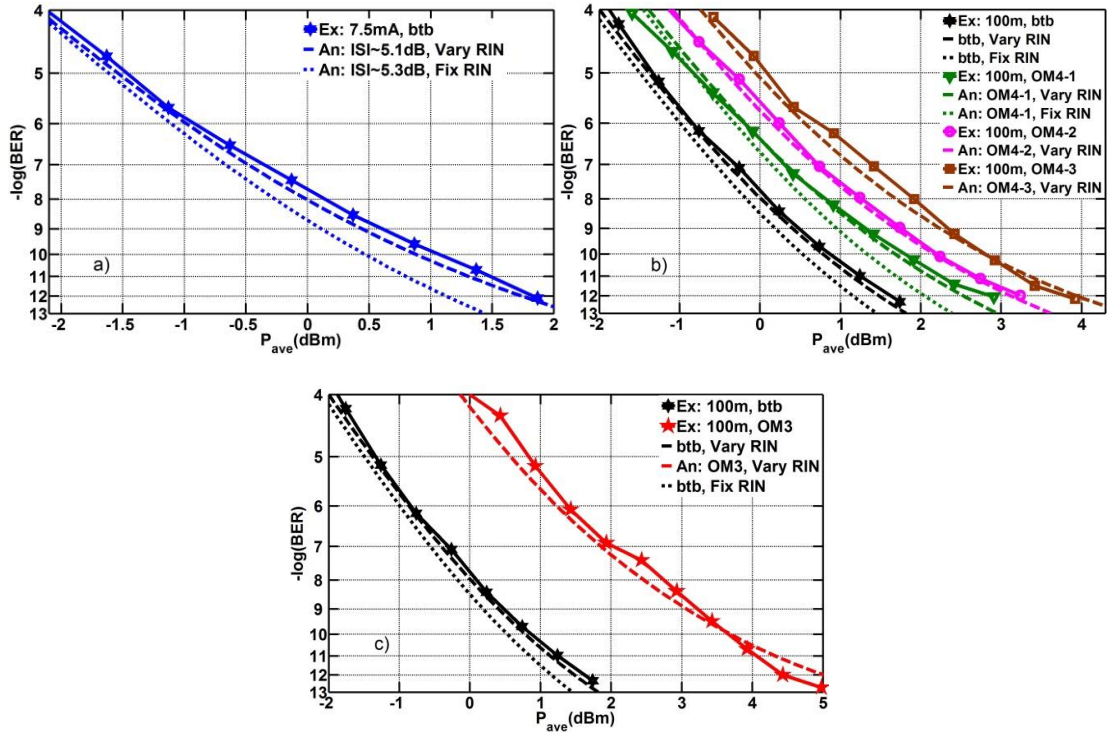


Fig. 7.11: 50Gbit/s PAM-4 for a) btb at 7.5mA bias; b) 100m of three standard OM4 fibers at 8.5mA. c) 100m of one standard OM3 fiber at 8.5mA. Ex: experimental, An: analytic model. Variable RIN yields improved fit to experiment.

example, our model predicts deviations of up to 2dB if the average RIN of the VCSEL is $> -145\text{dB/Hz}$ for an ER of $\sim 6\text{dB}$. Error-free transmission over 100m of three standard OM4 fibers and an OM3 fiber is also readily achieved, Fig. 7.11(b), (c). Here, a bias of 8.5mA and a full ER of $\sim 6\text{dB}$ was used. The EMBc of the three OM4 fibers are $\sim 10.0\text{GHz-km}$ (OM4-1), $\sim 6\text{GHz-km}$ (OM4-2) and $\sim 5.2\text{GHz-km}$ (OM4-3) with slightly different optimum wavelengths near 850nm.

The same individual RIN value was used as for the btb case resulting in a very good fit when an appropriate ISI penalty was used. On the other hand when using the single valued RIN the model deviates from the observed BER performance. Note that the

model predicts the MPN parameter k to be < 0.1 indicating negligible MPN in all the links.

7.6 Summary

It has been demonstrated, using comprehensive statistical data that error-free PAM-4 transmission is viable at both 850nm and 1050nm for speeds >50 Gbit/s over the standard OM3 and OM4 fibers with any fiber profile and EMBc between 2GHz.km to 10GHz.km. Using a special WBF that is designed to operate for wavelengths 850nm to 1100nm, it has been shown that error-free transmission of 62Gbit/s using 1050nm VCSELs with reach above 100m and 51.56Gbit/s with reach up to 300m. The 1050nm VCSEL exhibited a 3dB bandwidth of >18 GHz, modest nonlinearities, $RIN < -150$ dB/Hz, and negligible MPN up to 250m, demonstrating that these VCSELs support 51.56Gbit/s PAM-4 modulation. The spectral width of about 0.8nm creates negligible CD penalty since the CD parameter is ~ 40 ps/nm.km at 1050nm. It is also shown that, using an appropriate pre-emphasis filter at the transmitter, a FEC-conformed BER value of 10^{-5} can be achieved for 200m of this OM3 fiber. Analysis of the results reveals that, moving to longer wavelengths will improve the performance of the fibers, provided their bandwidth is maintained at that wavelength. The present standard OM3 and OM4 fibers which are optimized at 850nm, will offset the advantage we get from the decreased CD penalty by imposing an additional DMD penalty at 1050nm, resulting in a net average fiber penalty of ~ 1 dB compared to 850nm links. This can be overcome by employing the WBF, optimized for both 850nm and 1050nm operation. For the same fiber bandwidth estimated by the analytic model to be ~ 3.7 GHz.km, the 1050nm VCSEL links show better performance than the 850nm counterparts, as described in this work.

CHAPTER 8

POF STUDIES: IMPACT OF ELECTRONIC EQUALIZATION

The fast growing demand for bandwidth in short reach optical links has resulted in a need to increase the data rates of plastic optical fiber (POF) based links to 25Gbps and above. The development of perflourinated (PF) POF has enabled high-speed VCSEL-based links due to the lower attenuation values compared to the PMMA-POF in the 850nm band [60], [54]. Power penalty in any MMF link is caused by many impairment and noise effects namely, chromatic and modal dispersion, baseline wander (BLW) effect at the receiver, fiber and connector losses, laser noise and modal noise in the link. Among these, the penalty due to the inter-symbol interference (ISI) caused by deterministic effects such as dispersion, limited bandwidth of the channel and the BLW at the receiver can be compensated to some extent by strategic signal processing at the receiver[51][54]. It has been demonstrated that by using a simple FIR-based feed-forward equalizer (FFE) structure with modest number of taps, significant compensation of the penalty can be achieved. A digital implementation of an analog, fractionally-spaced FFE structure had been used here.

Using captured data streams we quantify the performance potential of analog, T/2-spaced FFE structures. We report ~3dB of link performance gain at 25Gbit/s with a modest tap-length FFE structure for a 100m-long 80 μ m-core POF that exhibits non-ideal DMD response. The FFE filter is also used to implement an effective channel estimation technique to determine the channel response of the POF-based optical link which showed a much lower bandwidth value for the POF than its calculated minimum effective modal bandwidth [85] (EMBc). The channel response thus calculated has been verified by a

direct measurement of the channel response from the experimental raw data. Thus it has been demonstrated that VCSEL based POF links benefit from low complexity FFEs, and that 100m POF links with equalization will have a similar overall power budget compared to silica OM4 links without equalization. FFE equalizers can be implemented fairly easily in hardware and thus allow high performance POF fiber to be used in 25Gbit/s links [71].

The performance of each element of the link has been quantified including VCSEL, fiber and receiver in an effort to produce an accurate and complete modeling of 25Gbit/s MMF optical links.

8.1 VCSEL Characterization

The experimental test bed includes state-of-the-art 25G-40G multimode oxide-aperture VCSEL die [72], various examples of 80 μ m core GI-PF-POF and a custom 30G optical-receiver capable of high responsivity and stable frequency response when coupled to MMF. A high-speed pattern generator is used to drive a VCSEL with a pseudo random binary sequence (PRBS) with a pattern length of $2^{15}-1$ and a bias-tee is used to supply the DC bias, Fig. 8.1. The amplifier used after the pattern generator provides the necessary drive signal amplitude for the VCSEL modulation. The VCSEL output is coupled into the POF under test as shown in the figure through a 2m 50 μ m core glass fiber. The lens between the VCSEL and the 50 μ m fiber was taken from a 10G commercial TOSA module. As a result, the 50 μ m fiber is filled and has an encircled flux that conforms to the IEEE 802.3ae standard, which was experimentally confirmed. The link experiments used a 100m long Lucina W-clad fiber with a core diameter of 80 μ m. 3-axis stages are used to align the 50 μ m launch fiber to the POF and the 62.5 μ m collection fiber to the

POF for maximum power coupling. The collection fiber is followed by a commercial 62.5 μm variable optical attenuator (VOA), which is used to vary the received optical power. The VOA is placed at the end of the link so that the mode power distribution in the POF remains constant. After the VOA a 62.5 μm lensed tip fiber is utilized for coupling into the photodiode. 62.5 μm is the largest core size readily available for lensed

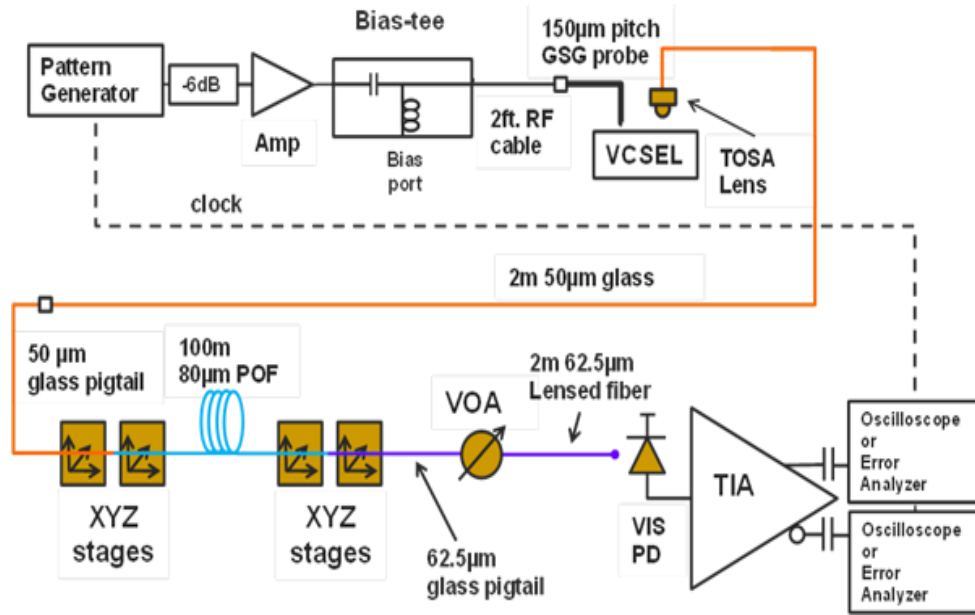


Fig. 8.1 Schematic of the experimental setup

fibers that achieve $<20\mu\text{m}$ spot size. The core of the collection fiber is smaller than the POF core, which will lead to some higher order mode stripping. This will not greatly impact the link performance because the POF has significant differential mode attenuation of the higher order modes [5].

The optical receiver consists of an Inphi 4331TA TIA and a VI Systems (VIS) GaAs photodiode with a 30 μm aperture and a capacitance of 100fF. Data from the setup was captured using a real time digital oscilloscope at 80GSa/s. This unequalized data was used for channel estimation using a linear equalizer structure which will be described in the later sections. Performance evaluation of the link before and after equalization is also

performed and the results are presented in section V. VCSEL characterization and POF fiber modal bandwidth characterization has been performed.

8.1.1 VCSEL Characterization: Spectrum

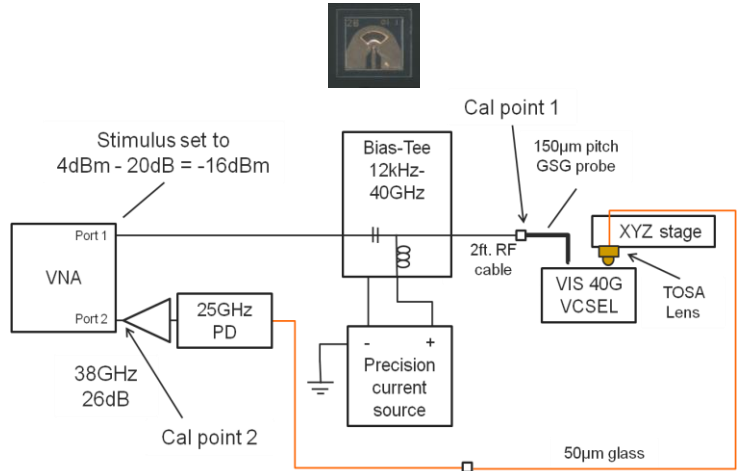


Fig. 8.2. Test setup used for VCSEL characterization

VCSEL output was coupled into a 50µm glass pigtail MMF through a lens taken from a commercial TOSA module. Figure 8.2 shows the test setup used for VCSEL characterization.

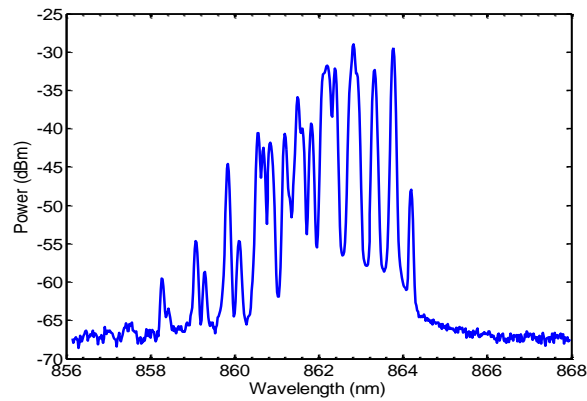


Fig. 8.3. VCSEL spectrum when biased at 15mA and modulated at 25Gbit/s

The same high-speed VCSEL was used for all the experiments reported. Figure 8.3 shows the spectrum of the VCSEL, when modulated at 25Gbit/s with 15mA bias (same parameters used in link experiments that follow). The RMS spectral width is

0.72nm, with center wavelength of 862.7nm. Additional 25Gbit/s VCSELs that were examined have similar or narrower spectral content. The chromatic dispersion (CD) of GI-PF-POF is typically -88 ps/nm·km at 845nm with a dispersion slope of +0.3 ps/nm²·km [5]. Following the Gaussian assumption, per IEEE 802.3 standards group, the impulse response is calculated to be ~16 ps for 100m leading to an ISI penalty of ~ 1dB for 25Gbit/s links [73]. Note that POF dispersion is almost 20% lower than that of silica fiber at 850nm.

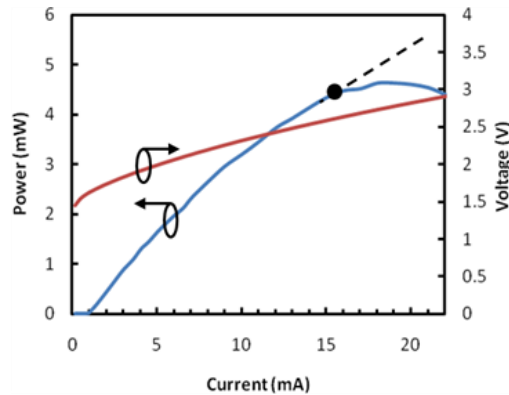


Fig. 8.4. L-I-V Curves for the VCSEL

8.1.2 VCSEL Characterization: L-I-V Characteristics

Figure 8.4 shows the L-I-V curves for the VCSEL. The VCSEL impedance is ~ 67Ω. Optimum performance was obtained for a DC bias of 15mA, which is close to the static L-I rollover. However, the lower duty cycle during modulation reduces thermal effects and the optimum bias appears high on the static L-I curve, an effect which has been noted by others [74]. The coupled VCSEL power is 6dBm. It was possible to modulate with average bias close to rollover due to the ½ mark density used with the 2¹⁵-1 PRBS pattern (average 50% duty cycle).

Dynamic effects including fluctuations in the mode power distribution (MPD) in the transverse modes in the VCSEL i.e. mode partitioning, which in turn leads to changes

to the MPD in the launch fiber and therefore in the fiber under test. Simultaneously, the VCSEL spectrum is changing due to the changing VCSEL mode partitioning (each transverse mode has a different wavelength). In short, each VCSEL mode power is changing as a function of time and each VCSEL mode couples into the fiber differently resulting in a unique MPD in the fiber associated with each transverse VCSEL mode. This is more complex than the mode partition noise (MPN) effect that was originally described for edge emitting lasers with multiple longitudinal modes, but a single transverse mode. In the edge emitting laser case, there is no notable change in the MPD of the fiber due to laser mode partitioning and MPN is purely a result of MPD fluctuations in the laser interacting with the CD of the fiber. The noise due to VCSEL mode partitioning will be exacerbated by any mode dependent loss in the link, which would not be the case for an edge emitting laser. Typically, noise arising from mode dependent loss and coherent speckle patterns in the fiber is referred to as modal noise. In VCSEL based links, the distinction often made between laser dependent modal noise and mode partition noise is somewhat dubious, since it is difficult to separate the laser mode partitioning dependent noise effects into two distinct impairments.

The noise due to VCSEL interactions with the fiber will be partially deterministic and therefore contribute to ISI that can be corrected with equalization. Modal noise is enhanced by differential mode attenuation (DMA) [76] and since POF has significantly more DMA than silica MMF [5], it is expected that there will be a higher modal noise in a VCSEL-based POF link. The DMA enhancement of the modal noise may be partially mitigated by the high mode mixing in the POF. There may also be polarization switching in the VCSEL [77] causing changes to the fiber MPD, but it is unknown to what extent

this VCSEL exhibits polarization switching and whether these effects could be partially deterministic. These additional complex VCSEL/fiber impairments result in significant ISI penalty in the link.

8.2 Receiver Characterization

The receiver is comprised of a custom designed PTFE-based (Rogers RT/duroid 5880) PC board with a laser etched cavity for the high-speed components, a VI Systems (VIS) GaAs photodiode with a $30\mu\text{m}$ aperture and a capacitance of 100fF , and an Inphi 4331TA TIA. Simulations, confirmed by experiment, using the TIA S-parameters, the lumped circuit model of the photodiode and the measured TIA-photodiode wire bond length, yield an effective photodiode electrical bandwidth $\sim 28\text{GHz}$. Due to the excess bandwidth of the receiver, the ISI induced due to receiver response time will be negligible. The low frequency cutoff is set to $\sim 25\text{kHz}$ with an off die capacitor connected to the decision threshold adjustment (DCA) feedback loop that accounts for the DC compensation of the non-zero average photocurrent. The current-mode logic (CML) outputs of the TIA are biased to 3.3V with external $>50\text{GHz}$ bias-tees. The receiver noise determined from the input referred RMS current noise of the receiver was measured to be $2.5\mu\text{A}$ with single ended output. The responsivity of the photodiode at 850nm was 0.4A/W .

8.3 Plastic Optical Fiber Modal Bandwidth Characterization

The perflourinated POF was manufactured using a preform and has an $80\mu\text{m}$ core with a graded W-clad index profile [78]. The differential modal delay (DMD) of this fiber has been measured, Fig. 8.5, using a procedure similar to the one described in TIA-455-220-A [79]. A mode mixer was used at the end of the fiber under test to maintain

consistency in the collection of relative mode powers by the detector. This mitigates mode dependent loss and mode dependent impulse response of the detector. In manufacturing of POF, deviations from the ideal alpha, as well as other non-ideal index deviations such as center dips/peaks, kinks, or core-cladding deviations will cause

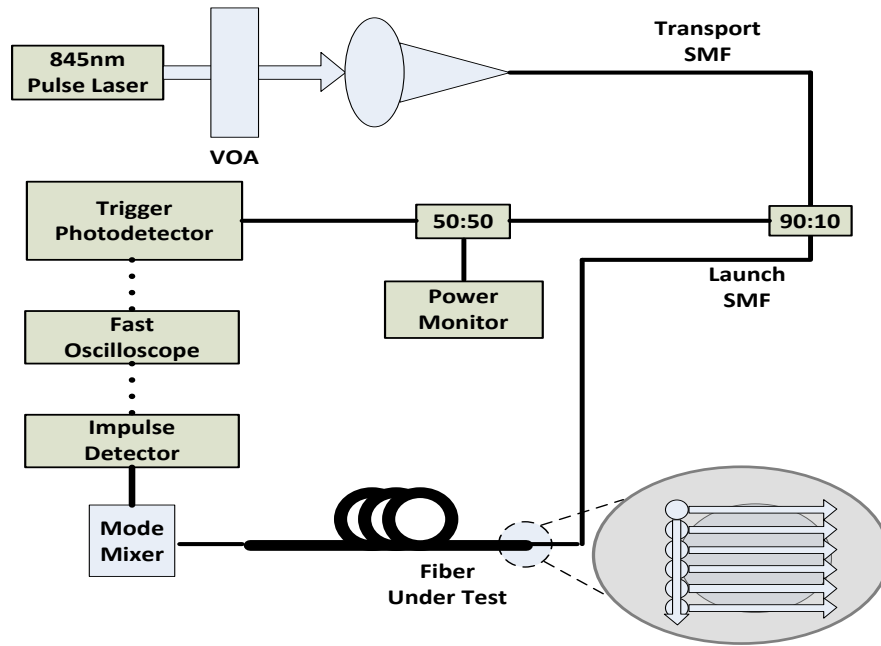


Fig. 8.5. Test setup for measuring DMD

bandwidth degradation. DMD is the difference between the time delays of the impulse responses measured at different excitation positions. More precisely, it is defined as the difference between 25% of trailing edge of slowest pulse and 25% of leading edge of fastest pulse when a short laser pulse from a SMF is scanned across the face of the MMF. The DMD measurement process not only validates that the fiber has sufficient bandwidth, but it also provides valuable feedback for fiber profile control.

High Resolution Differential Mode Delay (HRDMD) is measured by launching a ~ 12 ps, near transform-limited pulse produced by a mode-locked 845 nm titanium sapphire laser from a SMF that is scanned across the face of the MMF in one micron

steps. The temporal responses, shown in Fig. 8.6(a), yield a high resolution picture of modal delays excited by single mode fiber launch at each position. The DMD traces include the system response, which has a FWHM of ~ 25 ps. After normalizing the traces and de-convolving the system response the 200m long 80 μ m core GI-POF was found to have an X-cut DMD of 39 ps and a Y-cut DMD of 37 ps. The modal bandwidth of the fiber is calculated from this data by making use of a full set of DMD weightings that correspond to the range of fiber MPDs consistent with the encircled flux specifications for a set of ten IEEE 802.3 standards-compliant VCSEL launch MPDs [85]. An impulse response for the fiber is calculated by de-convolving the reference launch pulse output temporal response (calculated from the weighted DMD output pulses). The bandwidth is then determined by the traditional 3dB point on the resultant fiber transfer function, the least value of which is the min EMBc of the fiber. The fiber EMBc was calculated to be 23GHz which corresponds to a modal bandwidth-distance product of 4.6GHz \cdot km. The bandwidth-distance product is a fixed value for fibers with weak MC (like the silica GI-MMF) but it tends to decrease with length in the POF where there is strong MC [5]. So for the 100m POF link, the modal bandwidth is >46 GHz which corresponds to a power penalty ~ 0.5 dB assuming a Gaussian response [73]. An EMBc of >23 GHz was calculated for this fiber with 10 standard VCSEL MPDs.

Figure 8.6(b) shows the same DMD data with the amplitude of each pulse in dB. It should be noted that the individual pulses deviate from Gaussian response significantly and are asymmetric. In addition, the output pulses at various radial positions also exhibit wavy nature (ripple) and are not smooth, Fig. 8.6(c). It has been shown that for such fiber responses which exhibit wavy nature and significantly deviate from Gaussian response,

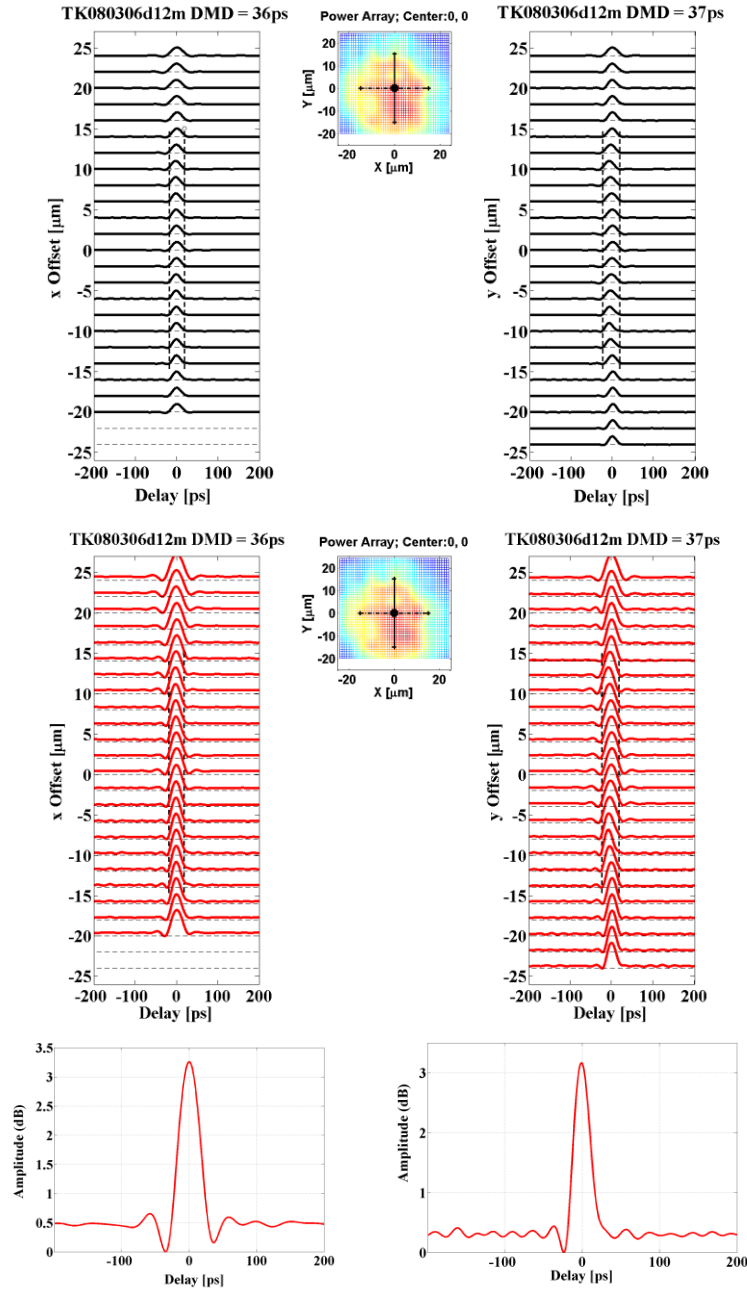


Fig. 8.6. Deconvolved and normalized DMD plots for the POF with amplitude of each pulse in (a) Linear scale; (b) dB scale; (c) A sample single pulse magnified to show ripple and non-Gaussian nature

the 3dB bandwidth is not an accurate metric of the link performance [86]. This non-ideal behavior of the DMD has been observed for most of the 18 different fibers with measured EMBc. The spreading of the mode powers across core diameter causes significant mode coupling which in turn increases the temporal width of the impulse response of the fiber,

thus reducing its effective bandwidth. The actual fiber bandwidth must thus be lower than the calculated standard EMBC value of 23GHz which assumes smooth Gaussian DMD response plots.

This observation of the degradation of fiber bandwidth is further consolidated when we analyze the channel response of the link, discussed in section IV below. This non-ideal DMD response of the fiber imposes an additional ISI penalty in the link which is deterministic and hence can be largely compensated along with the other ISI penalties using electronic equalization at the receiver end.

8.4 Fractional-Spaced Linear Analog Equalizer

Based on the VCSEL and fiber characterization results, the power penalties due to ISI from CD, MD, laser bandwidth and laser-fiber interactions are estimated to be >3dB. Owing to high attenuation values compared to silica-based optical links, the penalty due to the ISI could be highly detrimental to the performance of POF-based links. The power penalties due to the deterministic ISI effects can be compensated using a simple analog equalizer with modest number of taps. The tap-length of the equalizer is an indication of the complexity in analog circuitry required to implement the structure and hence of the cost of implementing the system [80], [71].

A digital implementation of the analog linear equalizer has been used to compensate for the dispersion-induced ISI. The linear equalizer, also called the feed-forward equalizer, consists of a simple finite impulse response (FIR) structure whose tap weights are adjusted to compensate for the channel distortion [81], [82]. Typically, two kinds of FFE structures are available: 1) Symbol-spaced equalizer, where the filter taps are separated by one whole symbol period; and 2) Fractionally-spaced equalizer in which

the tap-spacing is some fraction of the symbol period ‘T’.

The output of a T/K-spaced fractional feed forward equalizer is given by [14]

$$y(t) = a_{-N}Rx\left(t + \frac{NT}{K}\right) + \dots + a_{-1}Rx\left(t + \frac{T}{K}\right) + a_0Rx(t) + a_1Rx\left(t - \frac{T}{K}\right) + \dots + a_NRx\left(t - \frac{NT}{K}\right) \quad (8.2)$$

where $a_{-N} \dots a_{-1}, a_0, a_1, \dots, a_N$ are the filter tap weights, $Rx(t)$ is the unequalized received signal which is given as input to the FFE and ‘K’ represents the fractional delay between the taps. Here, a T/2-spaced equalizer had been used, since it has a better timing performance than symbol-spaced FFEs with same number of taps [84]. The filter tap weights are tuned adaptively to match the output to a known training sequence by least-mean-squares (LMS) algorithm [83] with a step-size of 0.01. Filter tap coefficients are

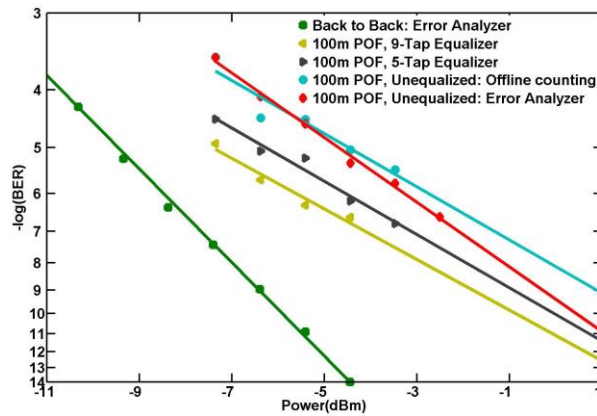


Fig. 8.7: BER of 100m POF before and after equalization using 5-tap and 9-tap FFE.

calculated by using a training sequence of length 6000 bits at the start of the transmission.

The performance of 5-tap FFE and 9-tap FFE has also been compared.

8.5 Impact of a T/2-FFE Equalizer on 100m POF Link: Results and Discussions

Figure 8.7 shows the performance of the 25Gbit/s POF link before and after equalization using a 5-tap and 9-tap FFE. The experiments used a 100m long Lucina W-clad fiber, with a core diameter of 80 μ m with a PRBS-15 pattern.

Errors were counted offline after clock recovery using a computer program. In order to validate the error counting process in our offline computation, also show the BER of the unequalized data from the 100m link counted by an SHF error analyzer which is in good agreement with the offline BER calculated with the computer methods. 2×10^7 bits have been counted for a PRBS pattern length of $2^{15}-1$. The extinction ratio was ~ 4 dB so the receiver sensitivity from the extrapolated data is ~ 0 dBm OMA. Results show that a penalty compensation of 2dB in the optical power can be readily achieved using a 5-tap fractional-spaced analog linear equalizer at a nominal BER of 10^{-6} . A further 1dB compensation of power penalty is shown to be possible if a 9-tap FFE is used. The 3dB penalty gain seen from the FFE mostly corresponds to the ISI penalties due to the CD (~ 1 dB) and the fiber bandwidth (which was shown in section IV to be ~ 2.4 dB). There might be additional minor penalties due to the VCSEL and its interplay with the fiber. The experimental raw data was captured at a rate of 3.2samples/bit which were then upsampled through interpolation to 20samples/bit for constructing the unequalized and equalized eyes. For the same optical modulation amplitude (OMA), the 9-tap FFE case exhibits significantly larger eye opening. This corresponds to a reduced vertical eye closure penalty (VECP) which is a widely accepted metric for the penalty due to ISI in the system [25]

8.6 POF Channel Estimation

Apart from improving the performance of the link, the fractional-spaced FFE can also be used to estimate the channel response by inputting the transmitted signal to the FFE and tuning the filter tap weights to make the output resemble the received signal. Since the fiber DMD exhibited non-Gaussian wavy-natured response, the calculated min

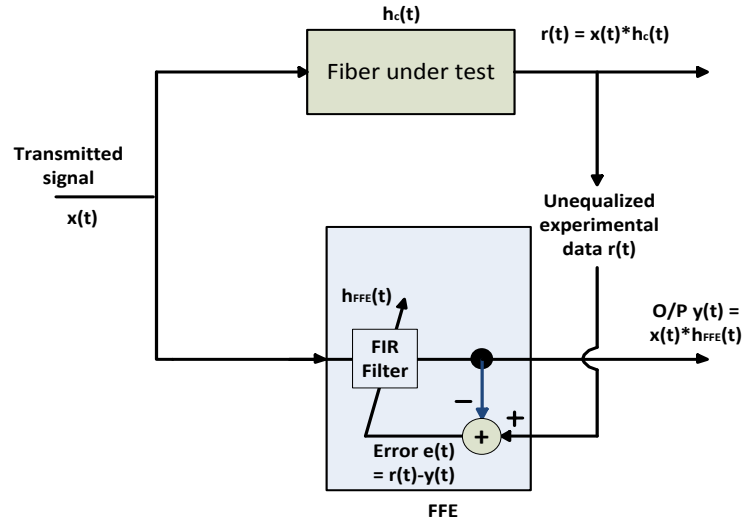


Fig. 8.8: Illustration of the channel estimation technique.

EMBC value does not accurately reflect the bandwidth of the fiber and the link. So the FFE filter has been used to estimate the 3-dB bandwidth of the 100m POF link by a technique illustrated in Fig. 8.8. The basic idea of this method is to use the experimental data to tune the filter tap weights of the FFE to resemble the fiber channel response. The same transmitted PRBS sequence used in the experiments was generated digitally and fed into the FFE structure which gives a filtered output $y(t)$. The difference between the unequalized experimental data and the output of the adaptive FIR filter gives the error signal $e(t)$ which is used to tune the filter tap weights of the FFE structure. The unequalized experimental data is represented as

$$r(t) = x(t) * h_c(t) \quad (8.3)$$

where $x(t)$ is the transmitted signal and $h_c(t)$ is the channel response of the MMF and the transmitter put together. Here ' * ' represents convolution. Similarly, the output of the FFE, $y(t)$ is given by

$$y(t) = x(t) * h_{FFE}(t) \quad (8.4)$$

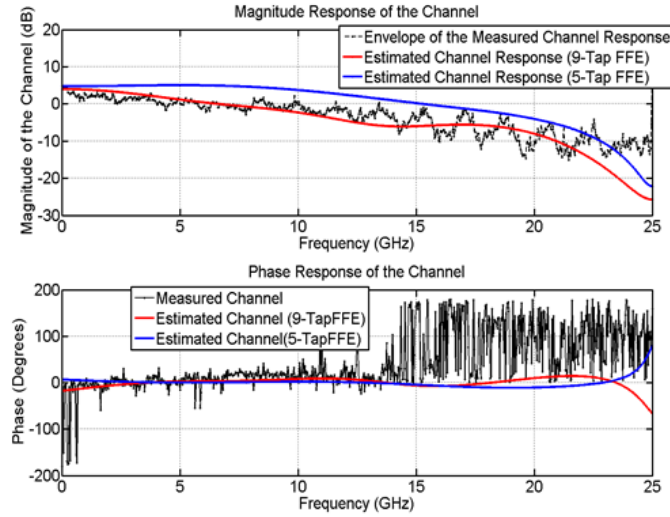


Fig. 8.9: Response of the 100m GI-PF-POF channel.

When the error signal $e(t)$ tends to zero, $y(t)$ tends to $r(t)$, and it follows from the equations that

$$h_c(t) = h_{FFE}(t) \quad (8.4)$$

Figure 8.9 shows the magnitude and phase of the estimated channel response from 9-tap FFE and 5-tap FFE structures. Note that this represents the response of the whole link up to the equalizer including the fiber, transmitter assembly, photodiode (PD) and the TIA. However, the bandwidth of this link is limited by the fiber response since the PD and the TIA have excess bandwidths as specified previously. For comparison, the channel response of the POF link has been measured by de-convolving the transmitted PRBS signal with the received signal. The phase noise seen in the measured channel response is due to the noise in the received signal. Response of the channel estimated

using a 9-tap FFE match the measured channel response better than the channel estimated using 5-tap FFE. The response of the fiber seems to be reasonably well-behaved for the frequency range measured, with a 3-dB cutoff at ~ 13 GHz. This low 3-dB cutoff is consistent with our observation about the bad DMD behavior of the fiber. Furthermore, the ISI penalty corresponding to this 13GHz bandwidth of the channel is ~ 2.4 dB, which is a deterministic penalty was and can be compensated through the FFE as shown in section V. The estimated channel response can further be used to simulate POF based links with synthetic channel and calibrated receiver model.

CHAPTER 9

CONCLUSION

9.1 Summary of Contributions

To address the rapid growth in the bandwidth needs, the IEEE 802.3 standard work groups continue to evolve standardizing optical links with speeds reaching 100Gbit/s. Consequently, some of the impairments that are negligible at lower speeds start to become prominent which need further investigation. This research addresses some of these challenges through a combination of advanced modeling and experimental studies for high-speed VCSEL-MMF links. In particular, the new MPN model developed here provides an accurate assessment of the MPN penalty in VCSEL-based links and is a step in the direction of understanding the complex spatial interactions of the multiple transverse modes in a VCSEL and the corresponding guided fiber modes. These modeling tools enable us to accurately simulate the MCDI effects which have significant impact on the dispersion induced fiber ISI penalties and the MPN for bitrates of 25Gbit/s and higher.

The new MPN model presented in this work has been developed starting from the Langevin noise-driven spatio-temporal rate equations that describe the transverse mode dynamics in a multi-mode VCSEL. A Covariance matrix representing the normalized variance and covariance of the laser mode powers was then derived from the noise-driven rate equations. This Covariance matrix formulation of the laser RIN and MPN is very generic and can be extended to any semiconductor laser with multiple longitudinal and transverse modes. Further, the derived expressions for the variance and covariance have

been reduced to three VCSEL-specific parameters which depend on the VCSEL physical parameters, and can be readily extracted through simple measurements on the VCSEL. Direct experimental measurements based on spatial filtering of VCSEL output have been used to verify the new model predictions. Further, simple closed-form expressions have been derived for MPN penalty in VCSEL-MMF links using reasonable approximations to the Covariance matrix described in the new model, thus allowing for a seamless integration into the widely used IEEE 802.3 spreadsheet model for high-speed VCSEL-MMF links.

On the experimental side, this work has resulted in high-speed demonstrations of PAM-4 based VCSEL-MMF links at $> 50\text{Gbit/s}$ using VCSELs at wavelengths of 850nm, 900nm and 1050nm. Comprehensive statistical analysis is done using representative OM3, OM4 and a prototype WBF to prove that deployable PAM-4 links with bit rates $> 50\text{Gbit/s}$ are possible at those wavelengths. Detailed analysis done on the fiber and noise penalties on the link data using analytic best fits reveal that while 1050nm links have an advantage of reduced CD penalty at the tested BER, the fiber induced MD penalty still dominates for 1050nm and results in relatively poor performance for standard OM3 and OM4 fibers that are optimized at 850nm. However, 1050nm PAM-4 links using specially designed WBF with good bandwidth qualities shall outperform 850nm links at bit rates $> 50\text{Gbit/s}$. In addition, this work has resulted in a thorough understanding of the temperature dependence of various VCSEL-MMF link penalties, including the deterministic ISI impairments such as CD, DMD, finite VCSEL and receiver bandwidths and random impairments such as VCSEL RIN and MPN penalties.

Finally, the research also shed light on the impact of electronic equalization on the POF-based VCSEL links. It has been shown that a simple fractional-spaced linear analog FFE can result in a significant penalty gain of up to ~ 3 dB in 100m POF links.

9.2 Future Directions

Some interesting venues opened up during the course of this research, which need further investigation. In particular, the complicated interplay of the multi-mode VCSEL output power and the fiber dispersion-induced modal delays results in penalties that need further investigation. At higher link speeds, the impact of the MCDI on the MPN penalty will be significant. Though the new MPN model presented in this work includes the MCDI effect through the effective bandwidth of the VCSEL-fiber pair, a simple analytical understanding of the relationship between the effective bandwidth and the physical launch conditions of the VCSEL-MMF pair is desired. Simple closed-form expressions capturing the MCDI effects in terms of the physical fiber and VCSEL parameters will facilitate optimal designing of future high speed short reach links.

Due to the limitations in the bandwidths supported by the state-of-the-art VCSELs, a direct modulated VCSEL-based link cannot go higher than 50Gbit/s, even after allowing some signal processing in the links. Consequently advanced multi-level modulation schemes should be further explored to achieve 100Gbit/s on single lambda. This work contributed in this direction by demonstrating error-free transmission of PAM-4 based links over a comprehensive set of fiber profiles, carefully chosen to span a wide range of profiles. Future 100Gbit/s links will require more advanced non-coherent modulation techniques such as Carrierless Amplitude Phase (CAP) modulation which can transmit more than 2 bits per symbol. Though a few demonstrations have been reported

on CAP-based optical links, the implementation complexities and the signal processing required to offset the associated penalties make them cost-prohibitive for the short reach applications. Thus, apart from the advanced modeling of VCSEL-MMF links, future efforts focusing on deployable multi-level modulation schemes with simple-enough implementation are desired.

APPENDIX A: DERIVATION OF COV MATRIX FROM LANGEVIN- DRIVEN VCSEL RATE EQUATIONS

It is obvious from the rate equations Eq. (6.1) and Eq. (6.2) that the noise correlation properties of different VCSEL modes depend on the correlation properties of the Langevin noise sources $F_{p,i}(t)$ and $F_n(t)$. It is important to note here that $F_n(t)$ has units of $\text{cm}^{-3} \cdot \text{sec}^{-1}$ and corresponds to the density Langevin noise source for the carrier reservoir in a volume $V_a = \pi R_a^2 d$, while $F_{p,i}(t)$ is the population Langevin noise source for the photon reservoir with units sec^{-1} . The corresponding correlations between the Langevin sources must be adjusted accordingly using the volume factor V_a . Under Markovian assumption of small correlation time for the noise sources compared to the lifetimes of the photons ($\tau_{p,i}$) and the carriers (τ_n), the reservoir Langevin noise sources are correlated with each other as [50], [39]

$$\overline{F_n(t')F_{p,1}(t)} = -\frac{2R_{sp}\overline{P_l(t)}\delta(t-t')}{V_a} \quad (\text{A.1})$$

$$\overline{F_{p,1}(t)F_{p,1}(t')} = 2R_{sp}\overline{P_l(t)}\delta(t-t') \quad (\text{A.2})$$

$$\overline{F_n(t)F_n(t')} = \frac{(2R_{sp}\overline{P_T(t)} + \gamma_n\overline{N_T(t)})\delta(t-t')}{V_a^2} \quad (\text{A.3})$$

$$\overline{F_{p,1}(t)F_{p,j}(t')} = 0, \text{ for } i \neq j \quad (\text{A.4})$$

where R_{sp} is the rate of spontaneous emission, $P_T(t)$ is the composite photon population such that $\overline{P_T(t)} = \sum_{k=1}^M \overline{P_k(t)}$ and $\gamma_n = A_{nr} + Bn + Cn^2 = \frac{1}{\tau_n}$ is the decay rate of carriers

and $\delta(t)$ is the Kronecker delta function. Here A_{nr} represents the non-radiative recombination mechanisms like the surface or trap recombination, B represents the radiative recombination coefficient, while C corresponds to the Auger recombination process.

The correlations between the Langevin noise sources in frequency domain can be derived by taking the Fourier transform of equations (A.1) through (A.4):

$$\lim_{T \rightarrow \infty} \{F_n(\omega) F_{p,i}^*(\omega)\} = -\frac{2R_{sp}\overline{P_i(t)}}{V_a} \quad (\text{A.5})$$

$$\lim_{T \rightarrow \infty} \{F_{p,i}(\omega) F_{p,i}^*(\omega)\} = 2R_{sp}\overline{P_i(t)} \quad (\text{A.6})$$

$$\lim_{T \rightarrow \infty} \{F_n(\omega) F_n^*(\omega)\} = \frac{(2R_{sp}\overline{P_T(t)} + \gamma_n\overline{N_T(t)})}{V_a^2} \quad (\text{A.7})$$

$$\lim_{T \rightarrow \infty} \{F_{p,i}(\omega) F_{p,j}^*(\omega)\} = 0 \quad (\text{A.8})$$

Linearization of the VCSEL rate equations can be performed by perturbing the i^{th} mode photon and carrier density populations around their steady-state values $\langle P_i(t) \rangle_t$ and $\langle N(r, \varphi, t) \rangle_t$.

This is done by writing

$$P_i = \overline{P_i} + \delta P_i(t) \quad (\text{A.9})$$

$$N(r, \varphi, t) = \overline{N(r, \varphi, t)} + \delta N(r, \varphi, t) \quad (\text{A.10})$$

Here, $\delta P_i(t)$ and $\delta N(r, t)$ represent differential perturbations of the steady-state values of i^{th} mode photons and carrier densities respectively. The corresponding perturbations for $g(r, t)$ and $G_i(t)$ are derived by substituting Eq. (A.10) in Eq. (6.3), (6.4) respectively:

$$g(r, \varphi, t) = \overline{g(r, \varphi, t)} + \delta g(r, \varphi, t) \quad (\text{A.11})$$

$$G_i(t) = \overline{G_i(t)} + \delta G_i(t) \quad (\text{A.12})$$

where the steady-state and the differential terms are given by

$$\overline{g(r, \varphi, t)} = a_o v_g (\overline{N(r, \varphi, t)} - N_t) \quad (\text{A.13})$$

$$\delta g(r, \varphi, t) = a_o v_g \delta N(r, \varphi, t) \quad (\text{A.14})$$

$$G_i(t) = \iint_0^{R_a, 2\pi} a_o v_g \psi_i^2(r, \varphi) (N(r, \varphi, t) - N_t) r dr d\varphi \quad (\text{A.15})$$

$$\delta G_i(t) = \iint_0^{R_a, 2\pi} a_o v_g \psi_i^2(r, \varphi) \delta N(r, \varphi, t) r dr d\varphi \quad (\text{A.16})$$

Substituting Eq. (A.9) through (A.12) in Eq. (6.1), we get

$$\begin{aligned} \frac{d\{\delta P_i(t)\}}{dt} = & \left[\left(\overline{G_i(t)} - \frac{1}{\tau_{p,i}} \right) \overline{P_i(t)} + \frac{\beta_i d}{\tau_n} \iint_0^{R_a, 2\pi} \overline{N(r, \varphi, t)} r dr d\varphi \right] + \left(\overline{G_i(t)} - \frac{1}{\tau_{p,i}} \right) \delta P_i(t) \\ & + \overline{P_i(t)} \delta G_i(t) + \delta G_i(t) \delta P_i(t) + \frac{\beta_i d}{\tau_n} \iint_0^{R_a, 2\pi} \delta N(r, \varphi, t) r dr d\varphi + F_{p,i}(t) \end{aligned} \quad (\text{A.17})$$

Using the rate equations for the steady-state analysis and after neglecting the second order term $\delta G_i(t) \delta P_i(t)$, Eq. (A.17) reduces to

$$\frac{d\{\delta P_i(t)\}}{dt} = - \left(\frac{\beta_i d}{\tau_n \overline{P_i(t)}} \iint_0^{R_a, 2\pi} \overline{N(r, \varphi, t)} r dr d\varphi \right) \delta P_i(t) + \overline{P_i(t)} \delta G_i(t) + F_{p,i}(t) \quad (\text{A.18})$$

Here, we made use of the initial assumption that $\delta N(r, \varphi, t) \ll \overline{N(r, \varphi, t)}$.

Similarly, substituting Eq. (A.9) through (A.12) in Eq. (6.2) and using the steady-state rate equations, we derive

$$\begin{aligned}
& \frac{\partial\{\delta N(r, \varphi, t)\}}{\partial t} \\
&= -\frac{1}{\tau_n} \delta N(r, \varphi, t) - \sum_{k=1}^M A_k \psi_k^2(r, \varphi) \overline{P_k(t)} \delta g(r, \varphi, t) \\
&\quad - \sum_{k=1}^M A_k \psi_k^2(r, \varphi) \overline{g(r, \varphi, t)} \delta P_k(t) + F_n(t)
\end{aligned} \tag{A.19}$$

It is helpful to convert the partial differential equation to a regular differential equation containing time-dependent differential modal gain $\delta G_i(t)$. This can be achieved by multiplying Eq. (A.19) with $a_o v_g \psi_i^2(r, \varphi)$ and integrating over the cross-sectional area of the active region $A = \pi R_a^2$ which gives

$$\begin{aligned}
\frac{\partial\{\delta G_i(t)\}}{\partial t} &= -\frac{1}{\tau_n} \delta G_i(t) - \sum_{k=1}^M \{a_o v_g \langle \psi_i^2(r, \varphi) \psi_k^2(r, \varphi) \delta g(r, \varphi, t) \rangle_r \overline{P_k(t)}\} \\
&\quad - \sum_{k=1}^M a_o v_g \langle \psi_i^2(r, \varphi) \psi_k^2(r, \varphi) \overline{g(r, \varphi, t)} \rangle_r \delta P_k(t) + a_o v_g F_n(t)
\end{aligned} \tag{A.20}$$

It is justified to assume that the perturbed differential carrier density $\delta N(r, \varphi, t)$ is proportional to the local time-averaged carrier density $\overline{N(r, \varphi, t)}$, i.e.,

$$\delta N(r, \varphi, t) = \overline{N(r, \varphi, t)} \delta K(t) \tag{A.21}$$

where $\delta K(t)$ is the time-component of the perturbation. Using this assumption, we can write

$$\delta g(r, \varphi, t) = \overline{g(r, \varphi, t)} \delta K(t) \tag{A.22}$$

$$\delta G_i(t) = \overline{G_i(t)} \delta K(t) \tag{A.23}$$

Using Eq. (6.22), (6.23) in Eq. (6.20), we get

$$\begin{aligned} \frac{\partial\{\delta G_i(t)\}}{\partial t} = & -\frac{1}{\tau_n}\delta G_i(t) - \frac{\delta G_i(t)}{G_i(t)} \sum_{k=1}^M \{a_o v_g A_k C'_{ikg} \overline{P_k(t)}\} - \sum_{k=1}^M a_o v_g A_k C'_{ikg} \delta P_k(t) \\ & + a_o v_g F_n(t) \end{aligned} \quad (\text{A.24})$$

Here, $\{C'_{ikg}\}_{i,k=1}^M$ represents the unnormalized spatial overlap integral of the intensity profiles of the transverse modes i, j and the time-averaged spatial gain density $\overline{g(r, \varphi, t)}$, given by

$$C'_{ikg} = \langle \psi_i^2(r, \varphi) \psi_k^2(r, \varphi) \overline{g(r, \varphi, t)} \rangle_{r, \varphi} = \iint_0^{R_a, 2\pi} \psi_i^2(r, \varphi) \psi_k^2(r, \varphi) \overline{g(r, \varphi, t)} r dr d\varphi \quad (\text{A.25})$$

$\{C'_{ikg}\}_{i,k=1}^M$ can be normalized by writing

$$C'_{ikg} = C_{fac} C_{ikg} \quad (\text{A.26})$$

Here, $\{C_{ikg}\}_{i,k=1}^M$ are the normalized overlap integrals, each ranging from 0 to 1 and C_{fac} is the normalization factor given by

$$C_{fac} = \sqrt{\langle \psi_i^4(r, \varphi) \overline{g(r, \varphi, t)}^2 \rangle_{r, \varphi} \langle \psi_k^4(r, \varphi) \rangle_{r, \varphi}} \quad (\text{A.27})$$

Using uniform gain and mode spatial profile assumption, C_{fac} can be approximated to

$$C_{fac} = \frac{a_o v_g \overline{N(t)}}{(\pi R_a^2)^2 d} \quad (\text{A.28})$$

Taking Fourier transform of Eq. (A.18) and (A.24) and re-arranging,

$$\rho_i \delta P_i(\omega) - \overline{P_i(t)} \delta G_i(\omega) = F_{p,i}(\omega) \quad (\text{A.29})$$

$$a_o v_g \sum_{k=1}^M \{A_k C_{fac} C_{ikg}\} \delta P_k(\omega) + \rho_n \delta G_i(\omega) = a_o v_g F_n(\omega)$$

(A.30)

Here, the ρ_i and ρ_{ni} following substitutions have been made:

$$\rho_i = \left\{ j\omega + \frac{\beta_i d}{\tau_n P_i(t)} \iint_0^{R_a, 2\pi} \overline{N(r, \varphi, t)} r dr d\varphi \right\} \quad (\text{A.31})$$

$$\rho_{ni} = \left\{ \left(j\omega + \frac{1}{\tau_n} \right) + \frac{1}{G_i(t)} \sum_{k=1}^M \{ a_o v_g C_{fac} C_{ijg} \overline{P_k(t)} \} \right\} \quad (\text{A.32})$$

Eliminating $\delta G_i(\omega)$ from Eq. (A.29) and Eq. (A.30), we derive, for all $i = 1$ to M

$$\mathcal{A}_i \delta P_i(\omega) + \sum_{k \neq i}^M \{ \mathcal{M}_k C_{ikg} \} \delta P_k(\omega) = \mathcal{N}_i(F_n, F_{p,i}) \quad (\text{A.33})$$

where

$$\mathcal{A}_i = \left[\frac{\rho_{ni} \rho_i}{P_i(t)} + a_o v_g A_i C_{fac} C_{iig} \right] \quad (\text{A.34})$$

$$X_i = \frac{\rho_{ni}}{P_i(t)} \quad (\text{A.35})$$

$$\mathcal{M}_k = a_o v_g A_k C_{fac} \quad (\text{A.36})$$

$$\mathcal{N}_i(F_n, F_{p,i}) = a_o v_g F_n(\omega) + X_i F_{p,i}(\omega) \quad (\text{A.37})$$

Eq. (A.33) represents a system of M linear equations in $\{\delta P_i(\omega)\}_{i=1}^M$, and hence can be solved using Cramer's rule which gives

$$\delta P_i(\omega) = \frac{\Delta_i(\omega)}{\Delta(\omega)} \quad (\text{A.38})$$

It can be argued that the major contribution to the cross-correlation between modes i and j is through the direct interaction between the two modes through the

common gain medium. Thus we can neglect the terms other than i and j in the determinants, Eq. (6.19) and (6.20) while calculating $cov_{ij}(\omega)$, i.e.,

$$\Delta(\omega) = \begin{vmatrix} \mathcal{A}_i & \mathcal{M}_j C_{ijg} \\ \mathcal{M}_i C_{ijg} & \mathcal{A}_j \end{vmatrix} \quad (\text{A.39})$$

$$\Delta_i(\omega) = \begin{vmatrix} \mathcal{N}_i(F_n, F_{p,i}) & \mathcal{M}_j C_{ijg} \\ \mathcal{N}_j(F_n, F_{p,j}) & \mathcal{A}_j \end{vmatrix} \quad (\text{A.40})$$

$$\Delta_j(\omega) = \begin{vmatrix} \mathcal{A}_i & \mathcal{N}_i(F_n, F_{p,i}) \\ \mathcal{M}_i C_{ijg} & \mathcal{N}_j(F_n, F_{p,j}) \end{vmatrix} \quad (\text{A.41})$$

A simplified closed-form expression for variance in the i^{th} mode, $\widetilde{var}_i(\omega)$ can then be derived as

$$\widetilde{var}_i(\omega) = \frac{1}{|\Delta(\omega)|^2} \lim_{T \rightarrow \infty} \left\{ \frac{1}{T} \Delta_i(\omega) \Delta_i^*(\omega) \right\} = \frac{1}{|\Delta(\omega)|^2} [\widetilde{var}_{pos}(\omega) - \widetilde{var}_{neg}(\omega)] \quad (\text{A.42})$$

where

$$\begin{aligned} \widetilde{var}_{pos}(\omega) &= \left\{ |\mathcal{A}_j|^2 + \mathcal{M}_j^2 C_{ijg}^2 \right\} (a_o v_g)^2 \overline{F_n(\omega) F_n^*(\omega)} + |X_i|^2 |\mathcal{A}_j|^2 \overline{F_{p,i}(\omega) F_{p,i}^*(\omega)} \\ &\quad + |X_j|^2 \mathcal{M}_j^2 C_{ijg}^2 \overline{F_{p,j}(\omega) F_{p,j}^*(\omega)} - 2a_o v_g C_{ijg} \text{Re}(\mathcal{M}_j \mathcal{A}_j X_j^*) \overline{F_n(\omega) F_{p,j}^*(\omega)} \\ &\quad - 2a_o v_g C_{ijg} \text{Re}(\mathcal{M}_j \mathcal{A}_j X_i) \overline{F_n(\omega) F_{p,i}^*(\omega)} \end{aligned} \quad (\text{A.43})$$

$$\begin{aligned} \widetilde{var}_{neg}(\omega) &= 2(a_o v_g)^2 C_{ijg} \text{Re}(\mathcal{M}_j \mathcal{A}_j) \overline{F_n(\omega) F_n^*(\omega)} - 2a_o v_g |\mathcal{A}_j|^2 \text{Re}(X_i) \overline{F_n(\omega) F_{p,i}^*(\omega)} \\ &\quad - 2a_o v_g \mathcal{M}_j^2 \text{Re}(X_j) C_{ijg}^2 \overline{F_n(\omega) F_{p,j}^*(\omega)} \end{aligned} \quad (\text{A.44})$$

For the typical values of a VCSEL, Table 1, the contributions due to the $\mathcal{M}_j^2 (a_o v_g)^2$ term in Eq. (A.43), (A.44) and the cross-fluctuations between the carrier and

photon reservoirs of the Langevin sources, $\overline{F_n(\omega)F_{p,l}^*(\omega)}$ and $\overline{F_n(\omega)F_{p,j}^*(\omega)}$ is small.

Neglecting these terms, we derive

$$\begin{aligned} \widetilde{var}_i(\omega) = & \frac{1}{|\Delta(\omega)|^2} [\{|\mathcal{A}_j|^2 - 2C_{ijg}Re(\mathcal{M}_j\mathcal{A}_j)\}(a_o v_g)^2 \overline{F_n(\omega)F_n^*(\omega)} \\ & + |X_i|^2 |\mathcal{A}_j|^2 \overline{F_{p,l}(\omega)F_{p,l}^*(\omega)} + |X_j|^2 \mathcal{M}_j^2 C_{ijg}^2 \overline{F_{p,j}(\omega)F_{p,j}^*(\omega)}] \end{aligned} \quad (\text{A.45})$$

The dependence of $\widetilde{var}_i(\omega)$ on the i^{th} mode power, measured through the i^{th} mode photon number $\overline{P_i(t)}$, is not trivial from Eq. (A.45) and requires separate analysis in the two frequency regimes. Note here from the Langevin noise correlations, Eq. (A.5) through (A.7), that $\overline{F_{p,l}(\omega)F_{p,l}^*(\omega)} \propto \overline{P_i(t)}$ while $\overline{F_n(\omega)F_n^*(\omega)}$ is independent of i^{th} mode power. Also, from Eq. (6.48) we have

$$|\Delta(\omega)|^2 \approx |\mathcal{A}_i \mathcal{A}_j|^2 \quad (\text{A.46})$$

In the low frequency regime, ignoring second order effects like the SHB, it is easy to see from Eq. (A.34) and (A.35) that X_i terms dominate in Eq. (A.45) resulting in

$$\widetilde{var}_i(\omega) = \frac{1}{|\mathcal{A}_i \mathcal{A}_j|^2} [|X_i|^2 |\mathcal{A}_j|^2 \overline{F_{p,l}(\omega)F_{p,l}^*(\omega)} + \mathcal{M}_j^2 |X_j|^2 C_{ijg}^2 \overline{F_{p,j}(\omega)F_{p,j}^*(\omega)}] \quad (\text{A.47})$$

Noting that $|X_i(\omega)| \propto \frac{1}{\overline{P_i(t)}}$, $|\mathcal{A}_i| \propto \frac{1}{\overline{P_i(t)}}$, we deduce from Eq. (6.2) that, $\widetilde{var}_i(\omega) \propto \overline{P_i(t)}$.

Now, in the high frequency regime, $|\mathcal{A}_j|^2$ term dominates in Eq. (A.45), resulting in

$$\widetilde{var}_i(\omega) = \frac{1}{|\mathcal{A}_i \mathcal{A}_j|^2} [|\mathcal{A}_j|^2 - 2C_{ijg}Re(\mathcal{M}_j\mathcal{A}_j)] (a_o v_g)^2 \overline{F_n(\omega)F_n^*(\omega)}$$

(A.48)

which gives a 2nd order dependence of variance on the i^{th} mode power, i.e., $\widetilde{\text{var}}_i(\omega) \propto \overline{P_i(t)}^2$.

For a broad range of frequencies, we can write

$$\begin{aligned} \widetilde{\text{var}}_i(\omega) = & \left[\left\{ |\mathcal{A}_j|^2 - 2C_{ijg} \text{Re}(\mathcal{M}_j \mathcal{A}_j) \right\} (a_o v_g)^2 \frac{\overline{F_n(\omega) F_n^*(\omega)}}{\overline{P_i(t)} |\mathcal{A}_i \mathcal{A}_j|^2} + |X_i|^2 |\mathcal{A}_j|^2 \frac{\overline{F_{p,l}(\omega) F_{p,l}^*(\omega)}}{\overline{P_i(t)} |\mathcal{A}_i \mathcal{A}_j|^2} \right. \\ & \left. + \mathcal{M}_j^2 |X_j|^2 C_{ijg}^2 \frac{\overline{F_{p,j}(\omega) F_{p,j}^*(\omega)}}{\overline{P_i(t)} |\mathcal{A}_i \mathcal{A}_j|^2} \right] \overline{P_i(t)} \end{aligned} \quad (\text{A.49})$$

It is useful to convert the photon numbers $\overline{P_i(t)}$ into normalized mode powers $\{\bar{a}_i\}_{i=1}^M$ related to photon population as $\overline{P_i(t)} = \bar{a}_i \overline{P_T(t)}$. Rewriting Eq. (A.49) in terms of the normalized mode powers, we have

$$\widetilde{\text{var}}_i(\omega) = \widetilde{\alpha}(\omega)^2 \bar{a}_i \quad (\text{A.50})$$

where $\widetilde{\alpha}(\omega)$ is the frequency domain proportionality constant, given by

$$\begin{aligned} \widetilde{\alpha}(\omega)^2 = & \left[\left\{ |\mathcal{A}_j|^2 - 2C_{ijg} \text{Re}(\mathcal{M}_j \mathcal{A}_j) \right\} (a_o v_g)^2 \frac{\overline{F_n(\omega) F_n^*(\omega)}}{\bar{a}_i |\mathcal{A}_i \mathcal{A}_j|^2} + |X_i|^2 |\mathcal{A}_j|^2 \frac{\overline{F_{p,l}(\omega) F_{p,l}^*(\omega)}}{\bar{a}_i |\mathcal{A}_i \mathcal{A}_j|^2} \right. \\ & \left. + \mathcal{M}_j^2 |X_j|^2 C_{ijg}^2 \frac{\overline{F_{p,j}(\omega) F_{p,j}^*(\omega)}}{\bar{a}_i |\mathcal{A}_i \mathcal{A}_j|^2} \right] \overline{P_T(t)} \end{aligned} \quad (\text{A.51})$$

In the special case of low overlap, $C_{ijg} \ll 1$, and for reasonably low frequencies, the proportionality constant reduces to

$$\widetilde{\alpha}(\omega)^2 = \frac{2R_{sp}}{\left| j\omega + \frac{\beta_i N_T(t)}{\tau_n P_i(t)} \right|^2} \quad (\text{A.52})$$

Following a similar approach, the covariance between modes i and j , cov_{ij} can be

calculated as

$$\widetilde{\text{cov}}_{lj}(\omega) = \frac{1}{|\Delta(\omega)|^2} \lim_{T \rightarrow \infty} \left\{ \frac{1}{T} \Delta_i(\omega) \Delta_j^*(\omega) \right\} = \frac{1}{|\Delta(\omega)|^2} [\widetilde{\text{cov}}_{pos}(\omega) - \widetilde{\text{cov}}_{neg}(\omega)] \quad (\text{A.53})$$

where

$$\begin{aligned} \widetilde{\text{cov}}_{pos}(\omega) &= \{ \mathcal{A}_j \mathcal{A}_i^* + \mathcal{M}_j \mathcal{M}_i^* C_{ijg}^2 \} (a_o v_g)^2 \overline{F_n(\omega) F_n^*(\omega)} \\ &\quad - 2 a_o v_g C_{ijg} \mathcal{M}_j \mathcal{A}_i^* \overline{\text{Re}(X_j) F_n(\omega) F_{p,j}^*(\omega)} \\ &\quad - 2 a_o v_g C_{ijg} \mathcal{M}_i^* \mathcal{A}_j \overline{\text{Re}(X_i) F_n(\omega) F_{p,i}^*(\omega)} \end{aligned} \quad (\text{A.54})$$

$$\begin{aligned} \widetilde{\text{cov}}_{neg}(\omega) &= C_{ijg} \left[\{ \mathcal{M}_j \mathcal{A}_i^* + \mathcal{M}_i^* \mathcal{A}_j \} (a_o v_g)^2 \overline{F_n(\omega) F_n^*(\omega)} + \mathcal{M}_j \mathcal{A}_i^* |X_j|^2 \overline{F_{p,j}(\omega) F_{p,j}^*(\omega)} \right. \\ &\quad \left. + \mathcal{M}_i^* \mathcal{A}_j |X_i|^2 \overline{F_{p,i}(\omega) F_{p,i}^*(\omega)} \right] \\ &\quad - \{ \mathcal{A}_j \mathcal{A}_i^* + \mathcal{M}_i^* \mathcal{M}_j C_{ijg}^2 \} (a_o v_g) X_i \overline{F_n(\omega) F_{p,i}^*(\omega)} \\ &\quad - \{ \mathcal{A}_j \mathcal{A}_i^* + \mathcal{M}_j \mathcal{M}_i^* C_{ijg}^2 \} (a_o v_g) X_j^* \overline{F_n(\omega) F_{p,j}^*(\omega)} \end{aligned} \quad (\text{A.55})$$

In the low overlap regime i.e., $C_{ijg} \ll 1$, the corresponding terms in Eq. (A.54)

and (A.55) can be neglected resulting in the covariance, $\widetilde{\text{cov}}_{ij}(\omega)^{(1)}$ of

$$\widetilde{\text{cov}}_{lj}(\omega)^{(1)} = \frac{(a_o v_g)^2 \mathcal{A}_j \mathcal{A}_i^*}{|\Delta(\omega)|^2} \overline{F_n(\omega) F_n^*(\omega)} \quad (\text{A.56})$$

Or

$$\widetilde{\text{cov}}_{lj}(\omega)^{(1)} = \frac{(a_o v_g)^2}{\mathcal{A}_i \mathcal{A}_j^*} \left\{ \frac{2R_{sp} \overline{P_T(t)} + \gamma_n \overline{N_T(t)}}{V_a^2} \right\} \quad (\text{A.57})$$

Using the inverse power proportionality of V_i and V_j , as discussed before, it can be readily seen from Eq. (A.57) that

$$\widetilde{\text{cov}}_{ij}(\omega)^{(1)} \propto \overline{P_i(t)} \overline{P_j(t)} \quad (\text{A.58})$$

In the other regime when there is high overlap between the VCSEL modes, , i.e., when $C_{ijg} \gg 0$, the terms containing C_{ijg} dominate over the other terms in Eq. (A.54) and (A.55), reducing Eq. (A.53) to

$$\begin{aligned} \widetilde{\text{cov}}_{ij}(\omega)^{(2)} &= \frac{C_{ijg}}{|\Delta(\omega)|^2} \left[\{ \mathcal{M}_j \mathcal{A}_i^* + \mathcal{M}_i^* \mathcal{A}_j \} (a_o v_g)^2 \overline{F_n(\omega) F_n^*(\omega)} \right. \\ &\quad \left. + \mathcal{M}_j \mathcal{A}_i^* |X_j|^2 \overline{F_{p,j}(\omega) F_{p,j}^*(\omega)} + \mathcal{M}_i^* \mathcal{A}_j |X_i|^2 \overline{F_{p,i}(\omega) F_{p,i}^*(\omega)} \right] \end{aligned} \quad (\text{A.59})$$

Or

$$\begin{aligned} \widetilde{\text{cov}}_{ij}(\omega)^{(2)} &= - \frac{C_{ijg}}{|\mathcal{A}_i \mathcal{A}_j|^2} \left[\{ \mathcal{M}_j \mathcal{A}_i^* + \mathcal{M}_i^* \mathcal{A}_j \} (a_o v_g)^2 \left\{ \frac{2R_{sp} \overline{P_T(t)} + \gamma_n \overline{N_T(t)}}{V_a^2} \right\} \right. \\ &\quad \left. + \mathcal{M}_j \mathcal{A}_i^* |X_j|^2 2R_{sp} \overline{P_j(t)} + \mathcal{M}_i^* \mathcal{A}_j |X_i|^2 2R_{sp} \overline{P_i(t)} \right] \end{aligned} \quad (\text{A.60})$$

Note that the covariance is negative in this case, indicating that the correlations are dominated by the mode competition effect. Also note the linear dependence of the $\widetilde{\text{cov}}_{ij}(\omega)$ on the overlap integral C_{ijg} . Using the inverse power proportionality of V_i and X_i in Eq. (A.59), we find

$$\widetilde{\text{cov}}_{ij}(\omega)^{(2)} \propto -C_{ijg} \overline{P_i(t)} \overline{P_j(t)} \quad (\text{A.61})$$

For the generic case where some modes overlap more than the others, combining Eq. (A.57) and (A.60), we can write

$$\begin{aligned}
\overline{\text{cov}}_{ij}(\omega) &= \overline{P_i(t) P_j(t)} \left[\frac{(a_o v_g)^2}{\mathcal{A}_i \mathcal{A}_j^* \overline{P_i(t) P_j(t)}} \left(\frac{2R_{sp} \overline{P_T(t)} + \gamma_n \overline{N_T(t)}}{V_a^2} \right) \right. \\
&\quad - \frac{C_{ijg}}{|\mathcal{A}_i \mathcal{A}_j|^2 \overline{P_i(t) P_j(t)}} \left\{ (\mathcal{M}_j \mathcal{A}_i^* \right. \\
&\quad \left. + \mathcal{M}_i^* \mathcal{A}_j) (a_o v_g)^2 \left(\frac{2R_{sp} \overline{P_T(t)} + \gamma_n \overline{N_T(t)}}{V_a^2} \right) + \mathcal{M}_j \mathcal{A}_i^* |X_j|^2 2R_{sp} \overline{P_j(t)} \right. \\
&\quad \left. \left. + \mathcal{M}_i^* \mathcal{A}_j |X_i|^2 2R_{sp} \overline{P_i(t)} \right\} \right]
\end{aligned} \tag{A.62}$$

APPENDIX B: RELATIONSHIP BETWEEN MPN PENALTY AND COVARIANCE MATRIX

The composite waveform at the receiver in the end-to-end fiber-optic link can be expressed as

$$r(t) = \sum_{i=1}^M a_i(\tau_i) r_i(t - \tau_i) \quad (\text{B.1})$$

where $r_i(t - \tau_i)$ is the normalized received waveform for the i^{th} VCSEL mode and τ_i is the relative time-delay for the i^{th} VCSEL mode due to dispersion. For a single-mode fiber link,

$$\tau_i = DL(\lambda_i - \lambda_o) \quad (\text{B.2})$$

Here L is the fiber length, D is the chromatic dispersion and λ_i and λ_o are the wavelengths of i^{th} and center modes respectively. For an MMF case, τ_i depends on the effective bandwidth which is a function of the chromatic dispersion parameter D , modal bandwidth of the fiber given by its differential mode delay (DMD) and the launch conditions at the VCSEL-MMF interface. Let us stick to the SMF case here for easy comparison with the O-A model. At the sampling instance t_k , the amplitude of the received sample is

$$r_k = \sum_{i=1}^M a_i(\tau_i) r_i(t_k - \tau_i) \quad (\text{B.3})$$

From now on, $r_i(t_k - \Delta\tau_i)$ will be written as r_{ik} for brevity. Assuming negligible receiver noise, the variance due to the VCSEL noise at the receiver is calculated as

$$\sigma_{\text{RIN+MPN}}^2 = \overline{r_k^2} - \bar{r}_k^2 \quad (\text{B.4})$$

Since the VCSEL fluctuations arise from the spontaneous emission fluctuations which do not change with time, it is safe to assume that the mode power fluctuations are wide-sense stationary (WSS) which means that their variance and covariance statistics

are independent of the absolute time delays. Substituting Eq. (B.3) and re-arranging, Eq. (B.4) reduces to

$$\sigma_{\text{RIN+MPN}}^2 = \sum_{i=1}^M r_{ik}^2 \text{var}_i + \sum_{i \neq j} r_{ik} r_{jk} \text{cov}_{ij}(\Delta\tau_{ij}) \quad (\text{B.5})$$

The frequency-dependent forms of $\mathbf{\Gamma}_p$ and \mathbf{k}_n in Eq. (6.46) and Eq. (6.47) above incorporate this time-dependence of the correlations. Using the corresponding time-domain versions of Eq. (6.46), (6.47) in Eq. (B.5) and re-arranging, we get

$$\sigma_{\text{RIN+MPN}}^2 = \alpha^2(\Delta\tau_{ij}) \sum_{i=1}^M r_{ik}^2 \bar{a}_i + \sum_{i \neq j} r_{ik} r_{jk} \{ \mathbf{\Gamma}_p^2(\Delta\tau_{ij}) - \mathbf{k}_n^2(\Delta\tau_{ij}) C_{ijg} \} \bar{a}_i \bar{a}_j \quad (\text{B.6})$$

Variance due to VCSEL noise, $\sigma_{\text{RIN+MPN}}^2$ is a function of the sampling instance of the received waveform. Since MPN is measured as the additional noise variance appearing over the variance due to the RIN when fiber is added, we have

$$\sigma_{\text{MPN}}^2 = \sigma_{\text{RIN+MPN}}^2 - \sigma_{\text{RIN}}^2 \quad (\text{B.7})$$

Substituting Eq. (B.6) and Eq. (6.46) in Eq. (B.7), we have

$$\sigma_{\text{MPN}}^2 = \alpha^2(\Delta\tau_{ij}) \sum_{i=1}^M \{ r_{ik}^2 - 1 \} \bar{a}_i + \sum_{i \neq j} \{ r_{ik} r_{jk} - 1 \} \{ \mathbf{\Gamma}_p^2(\Delta\tau_{ij}) - \mathbf{k}_n^2(\Delta\tau_{ij}) C_{ijg} \} \bar{a}_i \bar{a}_j \quad (\text{B.8})$$

APPENDIX C: PUBLICATIONS LIST

Journal Publications:

1. **Sriharsha Kota Pavan**, Patrick J. Decker, Yi Sun, Robert Lingle Jr., and Stephen E. Ralph, “Estimation of 25Gbit/s VCSEL-MMF Link Penalties at 850nm: Temperature Dependence”, *Journal of Lightwave Technology (JLT)*, vol.33, no.1, pp.109-116, Jan. 2015.
2. Andrew J. Stark, Pierre Isautier, Jie Pan, **Sriharsha Kota Pavan**, Mark Filer, Sorin Tibuleac, Robert Lingle, Jr., Richard de Salvo, and Stephen E. Ralph “Advanced Signaling Technologies for High-Speed Digital Fiber-Optic Links”, *Applied Optics (AO) and the Journal of the Optical Society of America (JOSA)*, vol.53, no.25, pp.5824-40, Sep. 2014 .
3. Justin Lavrencik, **Sriharsha Kota Pavan**, and Stephen E. Ralph “Direct Measurement of VCSEL Transverse Mode Correlation and k_{mpn} ”, *Photonics Technology Letters* vol.27, no.19, pp.2031-2034, Oct. 2015.
4. **Sriharsha Kota Pavan**, Justin Lavrencik, and Stephen E. Ralph “New Model for Mode Partition Noise in VCSEL-MMF Links Based on Langevin-driven Spatio-Temporal Rate Equations”, *Optics Express* 2016 (to be submitted).
5. **Sriharsha Kota Pavan**, Justin Lavrencik, and Stephen E. Ralph “Statistical Study of VCSEL-based PAM-4 Links Over MMF up to 62 Gbit/s and 150m Reach: Performance Comparison at 850nm and 1050nm”, *Optics Express* 2016 (to be submitted).

Selected Conference Publications

1. **Sriharsha Kota Pavan**, Justin Lavrencik, and Stephen E. Ralph, “Experimental demonstration of 51.56 Gbit/s PAM-4 at 900nm and impact of level dependent RIN”, *European Conference and Exhibition on Optical Communication (ECOC)*, Cannes, France 21-25 September 2014.
2. **Sriharsha Kota Pavan**, Justin Lavrencik, Roman Shubochkin, Yi Sun, Jinkee Kim, Durgesh Vaidya, Robert Lingle Jr., Tomofumi Kise and Stephen E. Ralph, “50Gbit/s PAM-4 MMF Transmission Using 1060nm VCSELs with Reach beyond 200m”, *Optical Fiber Communication Conference and Exposition and the National Fiber Optic Engineers Conference (OFC/NFOEC)*, San Francisco, California 9-12 March 2014.
3. Justin Lavrencik, **Sriharsha Kota Pavan**, David K. Haupt, and Stephen E. Ralph “Direct Measurement of Transverse Mode Correlation and MPN using 900nm

- VCSELS”, *Optical Fiber Communication Conference and Exposition and the National Fiber Optic Engineers Conference (OFC/NFOEC)*, Los Angeles, California 22-26 March 2015.
4. Justin Lavrencik, **Sriharsha Kota Pavan**, Alirio Melgar, and Stephen E. Ralph “Direct Measurement of Transverse Mode Correlation and Fiber-Enhanced RIN through MMF using 850nm VCSELS”, *Optical Fiber Communication Conference and Exposition and the National Fiber Optic Engineers Conference (OFC/NFOEC)*, Anaheim, California 20-24 March 2016.
 5. Yi Sun, Robert Lingle Jr., **Sriharsha Kota Pavan**, Patrick J. Decker and Stephen E. Ralph, “25 Gbps System Transmission Experiments Over 150 m Conventional and Bend-Optimized OM4 MMF Link”, *62nd International Cable Connectivity Symposium (IWCS)*, Charlotte, NC USA, 10-13 November 2013.
 6. **Sriharsha Kota Pavan**, Patrick J. Decker, Benjamin Klein and Stephen E. Ralph “New Model for Mode Partition Noise and Relative Intensity Noise in VCSEL-based Optical Links”, *IEEE Photonics Conference (IPC)*, Bellevue, Washington USA, 8-12 September 2013.
 7. **Sriharsha Kota Pavan**, Patrick J. Decker and Stephen E. Ralph, “Simulation of POF MMF links: Noise, ISI and Equalization”, *21st International Conference on Plastic Optical Fiber (POF)*, Atlanta, Georgia 10-12 September 2012.
 8. **Sriharsha Kota Pavan**, and Stephen E. Ralph “Signal processing in short reach high-speed MMF links”, *IEEE Avionics Fiber-Optics and Photonics Technology (AVFOP) Conference*, Cocoa Beach, Florida USA, 9-12 September 2012.
 9. C. Patrick Caputo, **Sriharsha Kota Pavan** and Stephen E. Ralph, “25G POF Links”, *1st International Conference on Advanced Photonic Polymers (ICAPP)*, Tokyo, Japan November 2011 (Invited Talk).

REFERENCES

- [1] IEEE802.3 Bandwidth Assessment Report, July 2012. [online]. <http://www.cablinginstall.com/articles/print/volume-22/issue-2/features/new-switch-architectures-impact-on-40-100g-data-center-migration.html>
- [2] J. Petrilla. (2012, September). Example MMF Link Model. IEEE 802.3bm 40Gb/s and 100Gb/s Fiber Optic Task Force. [Online]. http://www.ieee802.org/3/bm/public/sep12/ExampleMMF_LinkModel_%2012_09_18.xlsx
- [3] S. Kota Pavan, J. Lavrencik, R. Shubochkin, Y. Sun, J. Kim, D. Vaidya R. Lingle Jr., T. Kise, S. E. Ralph, "50Gbit/s PAM-4 MMF Transmission Using 1060nm VCSELs with reach beyond 200m," Proc. OFC, W1F.5, San Francisco, 2014.
- [4] G. P. Agrawal, "Fiber optic communication systems", Third edition, John Wiley and Sons, ISBN: 0-471-21571-6.
- [5] P. J. Decker, A. Polley, J. H. Kim, S. E. Ralph, "Statistical Study of Graded-Index Perfluorinated Plastic Optical Fiber", Journal of Lightwave Technology, vol.29, no.3, pp.305-315, Feb.1, 2011
- [6] T. Wipiejewski, T. Moriarty et al, "Gigabits in the home with plugless plastic optical fiber (POF) interconnects," Electronics System-Integration Technology Conference, Sept 2008.
- [7] D. Kuchta, A. Rylyakov, C. Schow, J. Proespel, F. Doany, C. W. Baks, B. H. Bissell, C. Kocot, L. Graham, R. Johnson, G. Landry, E. Shaw, A. MacInnes, and J. Tatum, "A 56.1Gb/s NRZ Modulated 850nm VCSEL-Based Optical Link", OFC 2013, paper OW1B.5, 2013.
- [8] J. D. Ingham, R. V. Penty, I. H. White, P. Westbergh, J. Gustavsson, A. Haglund, and A. Larsson, "32Gb/s Multilevel Modulation of an 850nm VCSEL for Next Generation Datacommunication Standards", CLEO 2011, paper CWJ2, 2011.
- [9] K. Szczerba, P. Westbergh, M. Karlsson, "60 Gbits error-free 4-PAM operation with 850 nm VCSEL". Electronics Letters, vol. 49(15), pp. 953-955, 2013.
- [10] K. Szczerba, P. Westbergh, J. Karout, J. S. Gustavsson, A. Haglund, M. Karlsson, P. A. Andrekson, E. Agrell, and A. Larsson, "30 Gbps 4-PAM transmission

- over 200 m of MMF using an 850 nm VCSEL,” *Optics Express*, vol. 19, no. 26, pp. B203–B208, Nov. 2011.
- [11] D. G. Cunningham, W. G. Lane, “Gigabit Ethernet Networking”, Macmillan Technology Series, 1999 ISBN: 1-57870-062-0.
- [12] G. P. Agrawal, P. J. Anthony, and T. M. Shen, "Dispersion penalty for lightwave systems with multimode semiconductor lasers," *J. Lightwave Technol.* 6, 620-625, 1988.
- [13] S. Kota Pavan, J. Lavrenchik, and S. E. Ralph, “Advanced simulation tools for VCSEL-MMF links > 25Gbit/s”, to be submitted, JLT.
- [14] K. Balemarthy, A. Polley, and S. E. Ralph, "Electronic Equalization of Multikilometer 10-Gb/s Multimode Fiber Links: Mode-Coupling Effects," *J. Lightwave Technol.* 24, 4885-4894, 2006.
- [15] S. Kota Pavan, P.J. Decker, B. Klein and S. E. Ralph, “New Model for Mode Partition Noise and Relative Intensity Noise in VCSEL-based Optical Links”, *Proc. Photonics Conference (IPC), 2013 IEEE* , pp.44,45.
- [16] Y. Koike and T. Ishigure, “Progress of low-loss GI polymer optical fiber from visible to 1.5- μ m wavelength,” in *Proc. 11th Int. Conf. Integr. Optics Opt. Fibre Communications, and 23rd Eur. Conf. Opt. Commun. (Conf. Publ. No. : 448)*, Sep. 1997, vol. 1, pp. 59–62, vol. 1, 22–25.
- [17] J. Castro, R. Pimpinella, B. Kose, and B. Lane, "The Interaction of Modal and Chromatic Dispersion in VCSEL based Multimode Fiber Channel Links and its Effect on Mode Partition Noise," *Proceedings of the 61st International Wire and Cable Symposium 2012*.
- [18] M. Webster, L. Raddatz, I. H. White, D. G. Cunningham, "A statistical analysis of conditioned launch for gigabit ethernet links using multimode fiber," *J. Lightw. Technol.*, vol.17, no.9, pp.1532-1541, Sep. 1999.
- [19] P. Pepeljugoski, M. J. Hackert, J. S. Abbott, S. E. Swanson, S. E. Golowich, A. J. Ritger, P. Kolesar, Y. C. Chen, P. Pleunis, “Development of System Specification for Laser-Optimized 50- μ m Multimode Fiber for Multigigabit Short-Wavelength LANs,” *J. Lightw. Technol.*, vol. 21, no.5, pp.1256-1275, May. 2003.

- [20] G. J. Meslener, "Temperature Dependence of Mode Distribution, Intensity Noise, and Mode-Partition Noise in Subcarrier Multiplexed Transmission Systems", *IEEE Photonics Technology Letters*, vol.4, no.8, pp.939-941, August 1992.
- [21] H. L. T. Lee, R. J. Ram, "Mode Partition Noise in Vertical Cavity Surface Emitting Lasers", Lasers and Electro-Optics Society Summer-Topical-Meetings, LEOS 2001.
- [22] J. Y. Law, G. P. Agrawal, "Mode-Partition Noise in Vertical Cavity Surface Emitting Lasers", *IEEE Photonics Technology Letters*, vol.9, no.4, pp.437-439, April 1997.
- [23] C. Webb, J. D. C. Jones, "Handbook of Laser Technology and Applications: Laser design and laser systems", Taylor & Francis, 2004, pg. 684.
- [24] K. Ogawa, "Analysis of mode partition noise in laser transmission systems," *IEEE J. Quantum Electron.*, vol. 18, pp. 849-855, May 1982
- [25] IEEE P802.3bs 400Gb/s Ethernet Task Force:
<http://www.ieee802.org/3/bs/>.
- [26] K. Ogawa, "Semiconductor laser noise: mode partition noise", chapter 8 in *Semiconductors and semimetals*, editors R.K. Williardson and A.C. Beer, Vol. 22C, Academic Press, NY, 1985.
- [27] J. Castro, R. Pimpinella, B. Kose, and B. Lane, "Mode Partition Noise and Modal-Chromatic Dispersion Interaction Effects on Random Jitter", *J. Lightw. Technol*, Vol. 31, No. 15, pp 2629-2638, 2013.
- [28] M. B. Willemsen, M. P. van Exter, and J. P. Woerdman, "Correlated fluctuations in the polarization modes of a vertical-cavity semiconductor laser," *Phys. Rev. A*, vol. 60, pp. 4105–4113, 1999.
- [29] J. P. Hermier, A. Bramati, A. Z. Khoury, V. Josse, E. Giacobino, P. Schnitzer, R. Michalzik, and K. Ebeling, *IEEE J. Quantum Electronics*, Vol. 37, No. 1, pp. 87-91, 2001.
- [30] R. Shubochkin, et al., "Trends in Datacom Optical Links," *Proc. IWCS 2013*.

- [31] “50Gb/s Per Lane Specification Considerations”, Chris Cole, IEEE 802.3 Plenary Meeting, 3 - 6 Nov. 2014, San Antonio, TX
- [32] L. Tao, Y. Wang, J. Xiao, N. Chi, “Enhanced performance of 400 Gb/s DML-based CAP systems using optical filtering technique for short reach communication”, *Optics Express*, 22(24):29331-9, Dec 1, 2014.
- [33] R. Hirai, H. Toyoda, N. Kikuchi, “Feasibility study of 100G/lambda Nyquist-PAM4 with commercially available 1.3um/1.5um EML”, IEEE 802.1/3 Joint Interim Meeting, September 8 - 13, 2014 Ottawa, Ontario, CANADA.
- [34] D. Kuchta, A. Rylyakov, C. Schow, J. Proesel, C. Baks, P. Westbergh, J. Gustavsson, and A. Larsson, "64Gb/s Transmission over 57m MMF using an NRZ Modulated 850nm VCSEL," in *Optical Fiber Communication Conference, OSA Technical Digest (online) (Optical Society of America, 2014)*, paper Th3C.2.
- [35] P. Pepeljugoski, “Dynamic Behavior of Mode Partition Noise in Multimode Fiber Links,” *IEEE Journal of Lightwave Technology*, vol. 30, no. 15, pp. 2514-2519, 2012.
- [36] Jose Castro, Rick Pimpinella, Bulent Kose, and Brett Lane , “Advances in characterization of the VCSEL mode partition noise penalty in optical fiber channels”, in *Optical Fiber Communication Conference, OSA Technical Digest (online) (Optical Society of America, 2014)*, paper Th2A.13.
- [37] Rick Pimpinella and Jose Castro, “Measurement and Estimation of the Mode Partition Coefficient k”, *IEEE P802.3bm 40 Gb/s and 100 Gb/s Fiber Optic Task Force*, November 2012, San Antonio, TX.
- [38] Murty, M. R., Cunningham, D., Giovane, L., Wang, J., Feng, Z. W., & Fanning, T. R. (2015, March). Mode partition noise characterization of 25 Gb/s VCSELs. In *SPIE OPTO (pp. 938104-938104)*. International Society for Optics and Photonics.
- [39] G. P. Agrawal and N. K. Dutta, *Semiconductor Lasers*, 2nd ed. New York: Van Nostrand Reinhold, 1993.
- [40] D. M. Kuchta, J. Gamelin, J. D. Walker, J. Lin, K. Y. Lau, and J. S. Smith, “Relative intensity noise of vertical cavity surface emitting lasers,” *Appl. Phys. Lett.*, vol. 62, 1194–1196, 1993.

- [41] R. Schatz and M. Peeters, "Modeling spatial-hole burning and mode competition in index-guided VCSELs," *Proc. SPIE*, vol. 4942, pp. 158–169, 2002.
- [42] A. Valle and L. Pesquera, "Analytical calculation of transverse mode characteristics in vertical-cavity surface-emitting lasers," *J. Opt. Soc. Amer. B*, vol. 19, no. 7, pp. 1549–1557, 2002.
- [43] J. Mulet and S. Balle, "Transverse mode dynamics in VCSELs: spatio-temporal versus modal expansion descriptions," *Phys. Rev. A*, pp. 53 801-1–53 801-8, 2002.
- [44] K. Becker, I. Fischer, W. Elsaber, "Spatio-Temporal Emission Dynamics of VCSELs: Modal Competition in the Turn-On Behavior", *Proceedings of SPIE Vol. 5452*, SPIE, Bellingham, WA, 2004.
- [45] A. Valle and L. Pesquera, "Mode partition noise in multi-transverse mode vertical-cavity surface-emitting lasers," *Proc. SPIE*, vol. 3625, pp. 414–425, 1999.
- [46] A. Valle and L. Pesquera, "Theoretical Calculation of Relative Intensity Noise of Multimode Vertical-Cavity Surface-Emitting Lasers", *IEEE JOURNAL OF QUANTUM ELECTRONICS*, VOL. 40, NO. 6, JUNE 2004.
- [47] M. Ahmed, M. Yamada, and S. Abdulrhmann "A MULTIMODE SIMULATION MODEL OF MODE-COMPETITION LOW-FREQUENCY NOISE IN SEMICONDUCTOR LASERS", *Fluctuations and Noise Letter*, vol. 1, no. 3 (2001), L163-L170.
- [48] Justin Lavrencik, Sriharsha Kota Pavan, and Stephen E. Ralph "Direct Measurement of VCSEL Transverse Mode Correlation and kmpn", *Photonics Technology Letters* vol.27, no.19, pp.2031-2034, Oct. 2015.
- [49] S. Kota Pavan, et al., *European Conference and Exhibition on Optical Communication (ECOC)*, Cannes, France 21-25 September 2014.
- [50] L. A. Coldren, S. W. Corzine, and M. L. Mashanovitch, *Diode Lasers and Photonic Integrated Circuits*, 2nd ed. New York: John Wiley & Sons, Inc., Appendix Thirteen, pp. 661-672, 2012.
- [51] J. H. Lau, R. V. Mohan, D. L. Kwong, X. Yongfei, P. V. Ramana, J. Chandrappan, Z. Jing, P. O. Gomez, and T. A. Aung, "Optical coupling methods for cost-effective

- polymer optical fiber communication,” *IEEE Trans. Comp. Packag. Technol.*, vol. 32, no. 3, pp. 593–599, Sep. 2009.
- [52] Y. Koike, T. Ishigure, and E. Nihei, “High-bandwidth graded-index polymer optical fiber,” *J. Lightw. Technol.*, vol. 13, no. 7, pp. 1475–1489, Jul. 1995.
- [53] T. Ishigure, H. Endo, K. Ohdoko, K. Takahashi, and Y. Koike, “Modal bandwidth enhancement in a plastic optical fiber by W-refractive index profile,” *J. Lightw. Technol.*, vol. 23, no. 4, pp. 1754–1762, Apr. 2005.
- [54] T. Ishigure, H. Kano, and Y. Koike, “Which is a more serious factor to the bandwidth of GI POF: Differential mode attenuation or mode coupling?,” *J. Lightw. Technol.*, vol. 18, no. 7, pp. 959–965, Jul. 2000.
- [55] S. E. Golowich, W. White, W. A. Reed, and E. Knudsen, “Quantitative estimates of mode coupling and differential modal attenuation in per-fluorinated graded-index plastic optical fiber,” *J. Lightw. Technol.*, vol. 21, no. 1, pp. 111–121, Jan. 2003.
- [56] A. Polley and S. E. Ralph, “Mode coupling in plastic optical fiber enables 40-Gb/s performance,” *IEEE Photon. Technol. Lett.*, vol. 19, no. 16, pp. 1254–1256, Aug. 15, 2007.
- [57] C. P. Caputo II, P. J. Decker, S. E. Ralph, “VCSEL-based 100m 25Gb/s Plastic Optical Fiber Links”, *Proc. Optical Fiber Communication (OFC/NFOEC) Conf.*, March 2011.
- [58] “IEEE Standard 802.3AQ-2006, Physical Layer and Management Parameters for 10Gb/s Operation, Type 10GBASE-LRM,” Sept. 2006.
- [59] D. Crivelli, H. Carrer, M. Hueda, N. Swenson, P. Voois, O. Agazzi, “Architecture and Experimental Evaluation of a 10Gb/s MLSD-Based Transceiver for Multimode Optical Fibers”, *Proceedings of IEEE Conference on Communications, Beijing*, May 2008.
- [60] S. C. J. Lee, F. Breyer, S. Randel, B. Spinnler, I. L. L. Polo, D. Van den Borne, J. Zeng, E. De Man, H. P. A. van den Boom, A. M. J. Koonen, “10.7 Gbit/s Transmission over 220 m Polymer Optical Fiber using Maximum Likelihood Sequence Estimation,” *Proc. Optical Fiber Communication (OFC/NFOEC) Conf.*, March 2007.

- [61] F. Breyer, N. Hanik, S. Randel, B. Spinnler, "Investigations on Electronic Equalization for Step-Index Polymer Optical Fiber Systems", Proc. Symposium IEEE/LEOS Benelux Chapter, Eindhoven, 2006.
- [62] D. Zeolla, A. Antonino, G. Bosco, and R. Gaudino, "DFE Versus MLSE Electronic Equalization for Gigabit/s SI-POF Transmission Systems", IEEE Photon. Technol. Lett., vol. 23, no. 8, pp. 510–512, Apr. 15, 2011.
- [63] F. Breyer, S. C. J. Lee, S. Randel, N. Hanik, "Comparison of OOK- and PAM-4 Modulation for 10 Gbit/s Transmission over up to 300 m Polymer Optical Fiber", Proc. Optical Fiber Communication (OFC/NFOEC) Conf., March 2008.
- [64] S. Loquai, R. Kruglov, B. Schmauss, C.A. Bunge, F. Winkler, O. Ziemann, E. Hartl, and T. Kupfer, " Comparison of Modulation Schemes for 10.7 Gb/s Transmission Over Large-Core 1 mm PMMA Polymer Optical Fiber", J. Lightwave Technology, vol.31, no.13, pp.2170-2176, Jul.1, 2013.
- [65] C. M. Okonkwo, E. Tangdionga, H. Yang, D. Visani, S. Loquai, R. Kruglov, B. Charbonnier, M. Ouzzif, I. Greiss, O. Ziemann, R. Gaudino, and A. M. J. Koonen, "Recent Results From the EU POF-PLUS Project: Multi-Gigabit Transmission Over 1 mm Core Diameter Plastic Optical Fibers", J. Lightwave Technology, vol.29, no.2, pp.186-193, Jan.15, 2011.
- [66] D. Marcuse, "Computer Simulation of Laser Photon Fluctuations: Theory of Single-Cavity Laser", J. Quantum Electronics, vol.20, no.10, pp.1139-1148, 1984.
- [67] H. Li and K. Iga, "Vertical-Cavity Surface-Emitting Laser Devices", Springer-Verlag Berlin Heidelberg 2003, ISBN: 978-3-642-08743-1.
- [68] K. Szczerba, M. Karlsson, P. A. Andrekson, and A. Larsson, "Intersymbol Interference Penalties for OOK and 4-PAM in Short-range Optical Communications", Proc. Optical Fiber Communication (OFC/NFOEC) Conf., March 2013.
- [69] R. Gitlin and S. Weinstein, "Fractionally-spaced equalization: An improved digital transversal equalizer," Bell Syst. Tech. J., vol. 60, no. 2, pp. 275–296, Feb. 1981.
- [70] Mool C. Gupta, John Ballato, "The Handbook of Photonics", Second Edition, Ch. 12-1.

- [71] A. Momtaz, Member, IEEE, and Michael M. Green, Member, IEEE, "An 80 mW 40 Gb/s 7-Tap T/2-Spaced Feed-Forward Equalizer in 65 nm CMOS", IEEE JOURNAL OF SOLID-STATE CIRCUITS, VOL. 45, NO. 3, pp. 629-639, MARCH 2010.
- [72] P. Westbergh, J. S. Gustavsson, B. Kögel, A. Haglund, A. Larsson, A. Mutig, A. Nadtochiy, D. Bimberg, A. Joel, "40 Gbit/s error-free operation of oxide-confined 850 nm VCSEL," Electronics Letters, vol.46, no.14, pp.1014-1016, July 2010.
- [73] Petar Pepeljugoski, "Enhanced Spreadsheet Model for 10Gb/sMMF Links", IBM Research, Yorktown Heights, NY 10598, presentation pepeljugoski_01_0508.
- [74] Z. Bouhamri, Y. Le Guennec, J. M. Duchamp, G. Maury, A. Schimpf, V. Dobremez, L. Bidaux, and B. Cabon, "Multistandard Transmission Over Plastic Optical Fiber," Microwave Theory and Techniques, IEEE Transactions on , vol.58, no.11, pp.3109-3116, Nov. 2010.
- [75] P. A. Morton, T. Tanbun-Ek, R. A. Logan, A. M. Sergent, P. F. Sciortino Jr, and D. L. Coblenz, "Frequency response subtraction for simple measurement of intrinsic laser dynamic properties", IEEE Photon. Tech. Lett., vol. 4, no. 2, pp.133 - 136, 1992.
- [76] Antonius M.J. Koonen, "Bit-Error-Rate Degradation in a Multimode Fiber Optic Transmission Link Due to Modal Noise", IEEE Journal on Selected Areas in Communications, vol. SAC-4, no.9, pp.1515-1522, Dec. 1986.
- [77] Joachim Kaiser, Christian Degen, and Wolfgang Elsässer, "Polarization-switching influence on the intensity noise of vertical-cavity surface-emitting lasers", J. Opt. Soc. Am. B, vol. 19, no.4, pp.672-677, Apr. 2002.
- [78] Asahi Glass Company: "LUCINA Graded Index-CYTOp® Optical Fiber (GI-POF)", Technical Bulletin, July 2000.
- [79] "FOTP-220 Differential Mode Delay Measurement of Multimode Fiber in the Time Domain", TIA-455-220-A, Jan. 2003.
- [80] John F. Bulzacchelli et al., "A 10-Gb/s 5-Tap DFE/4-Tap FFE Transceiver in 90-nm CMOS Technology", IEEE J. Solid-state circuits, vol.41, No.12, Dec 2006.

- [81] C. Xia et al., "On the Performance of the Electrical Equalization Technique in MMF Links for 10-Gigabit Ethernet", *J. Lightw Technol.*, vol.23, No.6, pp.2001-2011, June 2005.
- [82] R. Gitlin and S. Weinstein, "Fractionally-spaced equalization: An improved digital transversal equalizer," *Bell Syst. Tech. J.*, vol. 60, no. 2, pp. 275–296, Feb. 1981.
- [83] C. S. Fludger, T. Duthel, D. van den Borne, C. Schulien, E. D. Schmidt, T. Wuth, J. Geyer, E. D. Man, G. D. Khoe and H. de Waart, "Digital equalization of chromatic dispersion and polarization mode dispersion" *J. Lightwave Technology*, vol. 28, no. 11, pp. 1867-1875, Nov. 1980.
- [84] Moshe Nattiv, "FRACTIONAL TAP-SPACING EQUALIZERS FOR DATA TRANSMISSION", Department of Electrical Engineering, McGill University, Montreal, Canada, March 1979.
- [85] Doug Coleman and Phillip Bell, "Calculated Effective Modal Bandwidth Enhances 10GbE Performance Reliability for Laser-Optimized 50/125 μm Multimode Fiber", Corning Cable Systems White Paper, March 2005, LAN-639-EN / March 2005 / pdf.
- [86] INTERNATIONAL ELECTROTECHNICAL COMMISSION, "Optical Fibers- Part 1-49: Measurement methods and test procedures.